UNIVERSITY OF SOUTHAMPTON

Faculty of Engineering and Environment

INFRARED TECHNIQUES FOR QUANTITATIVE EVALUATION OF INTERFACIAL FRACTURE BEHAVIOUR AND DAMAGE TOLERANCE IN SANDWICH STRUCTURES

by

Wei Wang

Thesis for the degree of Doctor of Philosophy

February 2015

UNIVERSITY OF SOUTHAMPTON

ABSTRACT

FACULTY OF ENGINEERING AND ENVIRONMENT

Doctor of Philosophy

INFRARED TECHNIQUES FOR QUANTITATIVE EVALUATION OF INTERFACIAL FRACTURE BEHAVIOUR AND DAMAGE TOLERANCE IN SANDWICH STRUCTURES

by Wei Wang

An important failure mode of foam cored composite sandwich structures is the debonding between the face sheet and core. The challenges in establishing and improving the damage tolerance of sandwich structures mainly arise from the lack of reliable methods to characterise the fracture behaviour at face sheet/core interface. It has been demonstrated that the inclusion of crack arresting devices can improve damage tolerance. Characterisation of the fracture behaviour at tri-material interfaces is essential to evaluate the efficiency of such crack arresting devices, which are embedded in the foam core. Thereby, the research reported in the thesis seeks to establish optical measurement methods for characterising the stress fields at the crack tip and the crack tip parameters (i.e. fracture toughness) for foam cored composite sandwich structures, to provide a better understanding of the fracture behaviour at bi/tri-material interfaces.

Thermoelastic stress analysis (TSA) is used to establish the stress state at interfacial cracks. In the vicinity of growing interfacial cracks large and discontinuous motion occurs that has a deleterious effect on TSA, therefore a new motion compensation (MC) method is required. The thesis describes how the MC was developed and demonstrates the technique is essential for quantitative evaluations in the neighbourhood of a growing crack. Thus, the full-field stress state at an interfacial crack is obtained reliably and with a high spatial resolution.

An experimental method based on high speed infrared (IR) thermography is defined that enables the characterisation of fracture toughness by measuring the increase in temperature at the crack front (ΔT) during crack propagation. It is demonstrated that IR thermography with 15 kHz frame rate can be used to conduct a quantitative measurement of the crack front temperature associated with the crack growth. A constant of proportionality, ψ, is derived that links the temperature change per unit area at the crack front to the fracture toughness. It is shown that the ψ values obtained from specimens with the same interface are identical, even though the specimen dimensions and loading mode-mixities are different. It is demonstrated that by determining the values of ψ, the fracture toughness can be determined in any loading configuration by a direct temperature measurement.

The efficiency of crack arresting devices or ‘peel stoppers’ is established using TSA. The efficiency is defined as the ability of the peel stopper to deflect the crack from the face sheet/core interface and arrest its growth. To enable effective crack deflection away from the interface, modifications of the initial peel stopper design are proposed. TSA identified the local stress concentrations introduced by the different peel stoppers and established the mechanisms that control crack propagation in the vicinity of the peel stoppers. Thereby defining a configuration that contains the face sheet detachment in mode I dominated loading.

The work described in this thesis develops the optical measurement methods, based on imaging, to address the challenges in understanding interfacial fracture mechanisms and the determination of the crack tip parameters. This provides an important contribution to the understanding of the mechanics of interfacial fracture in foam cored composite sandwich structures.

Contents

List of Figures

List of Tables

Declaration of Authorship

I, *Wei Wang*, declare that the thesis entitled:

Infrared techniques for quantitative evaluation of interfacial fracture behaviour and damage tolerance in sandwich structures

and the work presented in this thesis are both my own, and have been generated by me as the result of my own original research. I confirm that:

this work was done wholly or mainly while in candidature for a research degree at this University;

where any part of this thesis has previously been submitted for a degree or any other qualification t this University or any other institution, this has been clearly stated;

where I have consulted the published work of others, this is always clearly attributed;

where I have quoted from the work of others, the source is always given. With the exception of such quotations, this thesis is entirely my own work;

I have acknowledged all main sources of help;

Where the thesis is based on work done by myself jointly with others, I have made clear exactly what was done by others and what I contributed myself;

Parts of this work have been published (Appendix A).

Signed: ……..

Date: …….

Acknowledgements

First, I would like to express my gratitude to my supervisors Prof. Janice M Dulieu-Barton and Prof. Ole Thomsen. Without their encouragement, patience and unfaltering dedication to the project, this thesis would not have reached its present form. The great help received from them for helping improve my English is really appreciated.

I would like to acknowledge my colleague Dr Richard K Fruhmann for shearing his knowledge and experience, especially the knowledge of TSA and high speed IR thermography. Also, a great thank to him for helping correct my English in my papers and PhD thesis. I would also like to express my gratitude to my colleagues Dr Shufeng Zhang, Dr Cedric Devivier, Mr Haibin Zhu, Dr George Crammond, Dr Gary Battams and Mr Georgios Martakos for their kindly help and advice.

The PhD project is co-sponsored by the University of Southampton and the Danish Council for Independent Research | Technology and Production Sciences (FTP), under the research project 'Enhanced Performance of Sandwich Structures by Improved Damage Tolerance' ('SANTOL'). The financial support received is gratefully acknowledged. The foam material supported by DIAB AB Sweden is highly appreciated.

Finally, I would like to thank my parents and wife for their love, patience, understanding and advice through these years. Thank you for your accompany when I was upset and in difficult time.

To all involved, a big thank you!

Wei

Nomenclature

Symbol	Meaning	Units
A	Area of crack increment	mm^2
C	Compliance	$m\ N^{-1}$
C_P	Specific heat at constant pressure	$J\ kg^{-1}K^{-1}$
D	Displacement value of each IR pixel	mm
E	Young's modulus	MPa
G	Energy release rate	$J\ m^{-2}$
G_C	Fracture toughness	$J\ m^{-2}$
G_S	Shear modulus	MPa
H	Non-dimensional bimaterial constants	-
K	Stress intensity factor	$MPa\ m^{1/2}$
K_T	Thermoelastic constant	Pa^{-1}
L	Half span length of the MMB rig	mm
M	Bending moment	N m
N	Subset size	*pixel*
P	Load	N
P_C	Critical load	N
Q	Heat	J
R	Spectral radiant emittance	$W\ m^{-3}$
S	Percentage of the overlap	%
T	Absolute temperature	K
U	Elastic strain energy	J
V	Displacement at the mid-point of each subset	mm

Abbreviation	Full version	Units
W_{ext}	Work done by the external forces	J
W_p	Plastic work	J
W_S	Surface energy	J
a	Crack length	mm
a_0	Initial crack length	mm
b	Specimen width	mm
c	Level arm distance of the MMB rig	mm
d	Spatial resolution	mm/pixel
e	emissivity	-
f	Intensity in the reference subset	-
f_l	Loading frequency	Hz
f_r	Frame rate	Hz
g	Intensity value in the deformed subset	-
h	Planck's constant	J s
h_s	Face sheet reinforcement thickness	mm
l	Distance	mm
n	Number of data points	-
s	Speed of light	$m\ s^{-1}$
t	Time	s
t_c	Core thickness	mm
t_f	Face sheet thickness	mm
u	Displacement vector, x direction	mm
v	Displacement vector, y direction	mm
Λ	Total energy	J
Π	Potential energy	J
δ	Displacement	mm
ρ	Density	$Kg\ m^{-3}$
σ	Stresses	Pa
σ_g	Global stresses on the specimen	Pa
σ_s	Average surface stress vallues	Pa
ϵ	Oscillatory index	-

Abbreviation	Full version	Units
φ_R	Reduced mode-mixity	^{o}
$\hbar$	Characteristic length of the crack problem	mm
φ	Mode-mixity	^{o}
φ_F	Full mode-mixity	^{o}
λ	Wavelength	m
κ	Boltzmann's constant	J K^{-1}
α	Coefficient of linear thermal expansion	$\times 10^{-6}$ K^{-1}
ς	Conductivity of material	W m^{-1} K^{-1}
Δ	Change in	-
θ	Interval between IR images	rad
υ	Possion's ratio	-
ψ	Constant of proportionality	J K^{-1} m^{-3}
R	Displacement ratio	-
ϕ	Vertex angle of the groove	^{o}
ϱ	Stress correction factor	-
γ	Tilt angle	^{o}

List of abbreviations

Abbreviation	Full version
TSA	Thermoelastic stress analysis
IR	Infrared
FE	Finite element
MC	Motion compensation
DIC	Digital image correlation
FRP	Fibre reinforced plastic
PVC	Polyunyl chloride
RIM	Resin infusion moulding
SCDE	Crack surface displacement extrapolation
LEFM	Linear elastic fracture mechanics
CSB	Cracked sandwich beam
TPSB	Three-point sandwich beam
DCB	Double cantilever beam
ELSS	End-laded sandwich specimen
TSD	Tilted sandwich debond
MMB	Mixed mode bending
DCB-UBM	Double cantilever beam specimen loaded with uneven bending moment
CFRP	Carbon fibre reinforced plastic
PU	Polyurethane
SPATE	Stress pattern analysis by thermal emissions
DL	Digital level
NUC	Non-uniformity correction

Abbreviation	Full version
EER	Energy release rate
CCD	Charge coupled device
FFT	Fast Fourier transform
SD	Standard deviation
CC	Cross-correlation
SSD	Sum-squared different

Chapter 1

Introduction

1.1 Background

A typical sandwich structure consists of a thick, low density core material sandwiched between two thin and high stiffness face sheets. Face sheets are adhesively bonded to the core which allows an efficient load transmission between the components. Compared to monolithic structures or laminated composites, this structure is well known for its superior bending stiffness and strength to weight ratios. The concept of sandwich structures was first adopted in the aircraft industry in 1920s, motivated by exploring materials with high structural efficiency for weight reduction of the airplane [1]. The later development of both core materials (balsa, corrugated, honeycomb and cellular foam) and face sheets (metals and fibre composites) has increased the use of sandwich structures to a larger scale in aerospace, marine, transportation, automotive and the energy (wind turbine blades) industries [2, 3].

The complexity of sandwich structures, which consist of at least three components and two interfaces, can lead to a wide range of damage scenarios such as local indentation, face wrinkling, core crushing and face sheet/core debonding [1]. For a sandwich structure, the existence of one damage type can introduce other subsequent damage during operation and the damage may not be uniformly distributed through the thickness [4]. To evaluate the criticality of a given damage and therefore prevent the catastrophic failure, a thorough understanding of damage tolerance of sandwich structures is necessary. However, in many applications, the conservative designs with large factors-of-safety are still used, due to the difficulty for designers to predict the critical damage modes [5]. The damage modes in sandwich structures have complex interactions, which require the

development of suitable measurement techniques to enable characterising how different damage initiates and what their behaviour in-service is [6-9]. This requirement is essential to establish the damage tolerance philosophy for sandwich structures and forms the fundamental motivation for the current study.

The particular damage mode considered in the current work is face sheet/core debonding. Debonds can initiate from manufacturing defects as well as in-service overload or impact. Early investigations of this damage type have shown that debonds can significantly affect the strength and buckling behaviour of sandwich structures, which highlighted the criticality of the debond damage [10-13]. Propagation of the debonded region can cause catastrophic failure of sandwich structures as their ultimate strength and stiffness are drastically reduced. To achieve a thorough understanding regarding debond damage tolerance, knowledge is required concerning different aspects which are summarised in the flowchart shown in Figure 1.1. According to these requirements, four principal challenges have to be addressed and are of great concern to current researchers. The first challenge is to develop methods for characterising crack tip parameters (e.g. the stress intensity factors and fracture toughness) [14] and fatigue crack growth rate [15]. The purpose is to establish multi-mode [16] fracture characteristics which can be used to define the maximum values of stresses, energy release rates and loading cycles above which the crack may propagate. The second is to improve the damage tolerance of the debonded sandwich structure by inhibiting debond propagation by introducing crack arr-

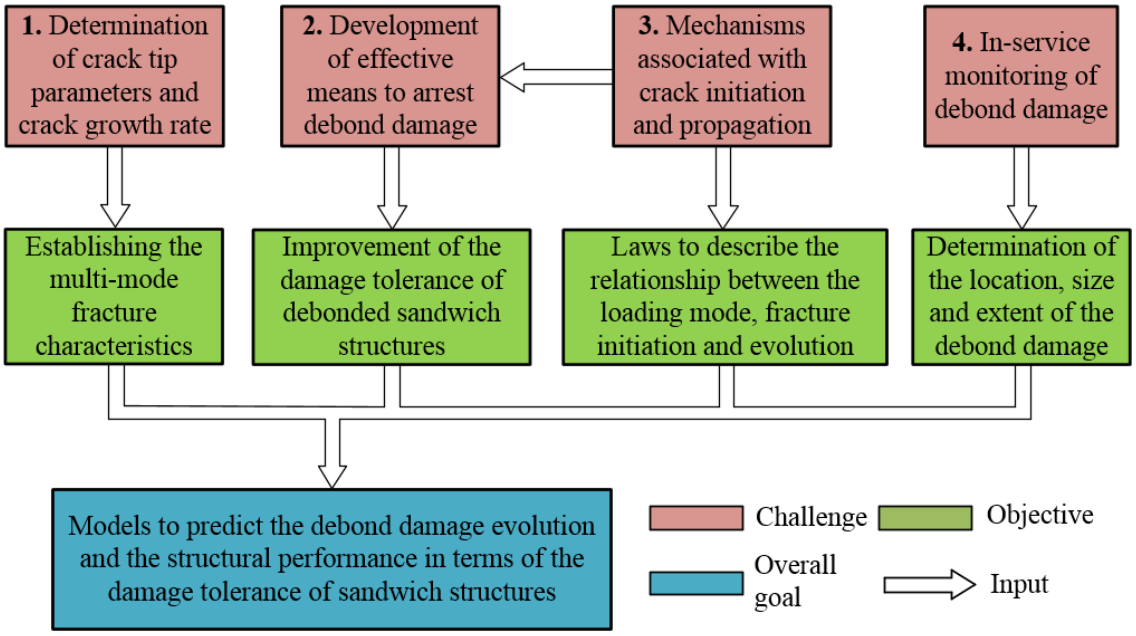

Figure 1.1: Flowchart of knowledge required for establishing and improving the damage tolerance philosophy of a debonded sandwich structure

esting devices into the face sheet/core interface to control the size/extent of the debond damage [17-19]. The third challenge is related to the understanding of the fracture mechanism associated with the debond initiation and evolution. The knowledge of how the debond initiates and propagates due to local effects at the bi-material interfaces or the tri-material interfaces at the crack arresting devices are essential to develop the fracture laws for characterising the fracture behaviour. The forth challenge is to develop non-destructive [20, 21] and structural health monitoring [22] methods to provide debond damage detection during the service life. As outlined in Figure 1.1, by implementing the established fracture laws and multi-mode fracture characteristics into a model, structural performance of a debonded sandwich structure can be predicted according to the extent of debonding obtained from in-service monitoring.

The work described in the thesis is concerned with the development of optical measurement methods, based on imaging, to address the challenges in understanding interfacial fracture mechanisms and the determination of the crack tip parameters. The work also considers the mechanisms that govern the processes of crack growth locally at crack arresting devices, to enable a better understanding of their efficiency.

The measurement methods are thermoelastic stress analysis (TSA) [23] and high speed infrared (IR) thermography [24]. TSA is based on the thermoelastic effect where a reversible temperature change induced by dynamic loading can be directly related to the change in stresses. In TSA it is usual to obtain the surface temperature change of a component using an IR detector, thus the full-field stress state can be derived without contact and damage. The high spatial resolution thermal data provided by modern IR detectors allow small scale local stresses to be investigated. This is important for studying debonding as fracture behaviour is affected by small features at the interfaces, and understanding the fracture mechanism requires the associated stress distribution to be resolved. The stress state obtained from TSA also provides the possibility to derive the crack tip stress intensity factor for the interfacial crack (but is beyond the scope of the thesis). Thus the non-contact and high resolution nature of TSA renders it as an attractive tool for investigating the interfacial fracture behaviour for sandwich structures. On the other hand, IR thermography is a technique that measures the surface temperature of the specimen. Generally, the image recording rate for IR thermography is limited by commercial IR detectors (e.g. maximum 383 Hz for the FLIR SC5500 IR system). However, the development of the calibration routine for off-the-shelf IR detectors has enabled the use of IR thermography at higher frame rates (up to 16 kHz for the FLIR SC5500 IR system) [24]. Thus high speed IR thermography provides an opportunity to characterise the thermal energy generated during the crack propagation before the heat dissipates. Hence opening the possibility of determining the fracture toughness by relating

the thermal energy to the fracture energy required for crack propagation in brittle materials.

1.2 Aims and Objectives

The overarching aim of this project is to develop optical measurement methods to enable the characterisation of the interfacial fracture behaviour in sandwich structures. This involves establishing high resolution data around the crack tip to provide better understanding of the interfacial fracture behaviour and determining the crack tip parameters. The particular concern of the project is the fatigue crack propagation mechanism at a crack arresting device proposed by Jakobsen *et al*. [18]. Based on the optical measurement methods developed during the PhD project, the work seeks to understand and improve the efficiency of the crack arresting device, thereby providing a means to improve the damage tolerance of sandwich structures. In summary the objectives of the PhD project are defined as follows:

1. Develop the TSA technique to establish the full-field and high resolution stress data at an interfacial crack tip in sandwich structures.

2. Develop a measurement method based on high speed IR thermography to characterise the interfacial fracture toughness for sandwich structures.

3. Investigate the influence of the local stress concentrations introduced at the tri-material junctions of the face sheet, core and the crack arresting device (termed local effects) using the TSA methodology.

The present PhD project is a part of a larger research project “enhanced performance of sandwich structures by improved damage tolerance” (SANTOL) funded by the Danish Council for Independent Research | Technology and Production Sciences (FTP) and co-sponsored by two industrial partners LM Wind Power A/S, Denmark, and Siemens Wind Power A/S, Denmark. SANTOL also involves two other PhD projects conducted by Marcello Manca at the Technical University of Denmark (DTU) and Georgios Martakos at Aalborg University (AAU), Denmark. The overall aim of SANTOL is to develop experimental and numerical methods to establish the multi-mode fracture characteristics of sandwich structures and establish a means for improving damage tolerance by inhibiting defect propagation. The typical sandwich structures studied are foam cored sandwich composites which are widely used in the webs and aerodynamic shells of wind turbine blades [3].

The work encompassed by the three individual projects and the research collaboration between the projects are presented by the flow diagram in Figure 1.2. The aim of each project is shown in blue and the overall achievements obtained are summarised in green. The arrows show where the results of one part of the project are required in another. The study of the fatigue crack propagation mechanism at the crack arresting device is a joint activity. TSA experimentally investigates the local effects at the crack arresting device and their influence on the fracture behaviour. The finite element (FE) model developed by Georgios Martakos simulates the energy release rate (ERR) developed at the crack arresting device. It is envisaged that the stresses and energy release rate based analysis can provide a thorough understanding of the fracture mechanism. To provide stable fatigue crack propagation conditions, the FE model is also used to predict the displacement amplitude applied by the test machine to allow the crack to propagate under a controlled energy release rate.

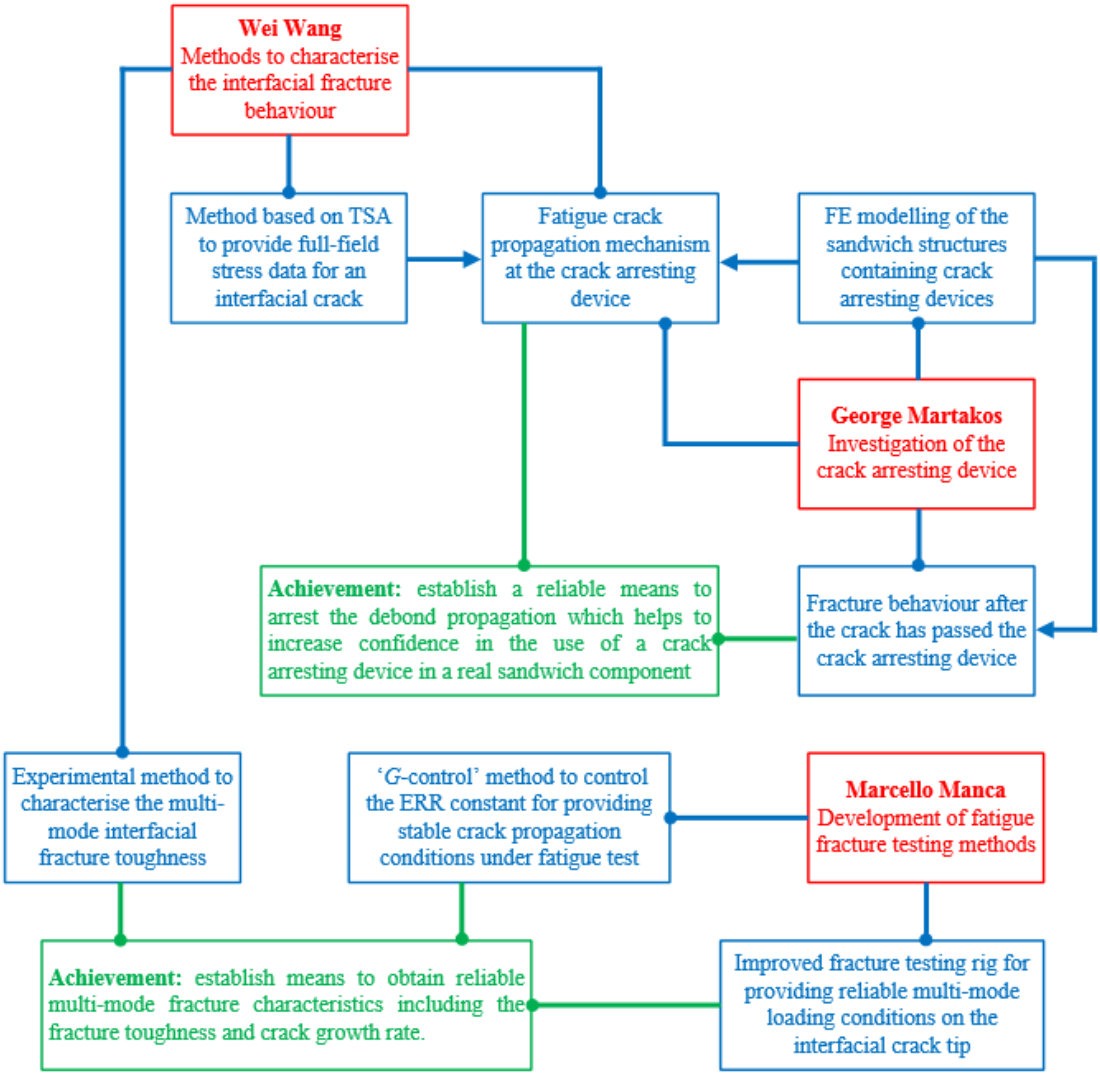

Figure 1.2: Outcomes and achievements of three individual projects and the interactions between different projects

1.3 Novelty

TSA has been successfully applied to many components and structures for the stress evaluation and analysis. However, for structural geometries where the loading results in large deformations, the motion of the structure relative to the stationary IR detector can result in erroneous assessment of the stress field. For TSA to be used as a measurement tool for quantifying the stresses in the neighbourhood of an interfacial crack in sandwich structures, it is necessary to compensate for the large and discontinuous motion induced by the face sheet/core detachment. The motion compensation (MC) approaches developed in previous work are reviewed in Chapter 3. These approaches are not suitable for structures with sharp and rapid gradients in displacement or discontinuous motion fields due to the fairly low resolutions that can be achieved with the existing MC techniques. In the present thesis a high spatial resolution MC method is developed that can compensate for large displacements and gradients. Based on the MC method, the full-field, high resolution stress data at interfacial crack tips in foam cored sandwich composites is obtained. It is shown that the TSA can provide the local stress fields at the crack tip associated with complex structural geometries (e.g. the cellular structure of the foam). Therefore, the TSA data serves as the basis for understanding the influence of local effects on the fracture behaviour and also provides a tool for validating FE models.

IR thermography can capture the heating associated with the debond growth. In a previous study [25] heat was found to dissipate during debond growth and IR thermography was able to capture the resulting temperature increase at the crack tip. However, a quantitative assessment of the relationship between the dissipated heat and the fracture energy associated with the crack growth has not been provided in the literature. A major challenge is the rapid heat dissipation at the crack front, requiring a very high data recording rate, i.e. a high framing rate for the IR system. Through a calibration procedure developed in [24], the IR detector used in this work can be operated at a high frame rate of 15 kHz. In this work a methodology is developed for capturing the temperature increase using high speed IR thermography. It is shown that meaningful temperature data associated with the crack growth can be obtained before heat dissipates. A quantitative analysis of the relationship between the dissipated heat and the fracture energy is provided, which shows the potential to determine the interfacial fracture toughness in sandwich structures by capturing the temperature evolution during crack growth.

The crack arresting device studied in this work has been examined experimentally [18, 26] using three-point bending tests, where the interfacial crack, initiated from core shear failure, was successfully deflected to a restricted area by the crack arresting device. However, a systematic study of the fracture deflection behaviour at the crack arresting

device under different loading conditions has not been provided. In the current work experimental investigations of the fracture behaviour at the crack arresting device under mode I dominated loading conditions are conducted. It is shown that modifications of the crack arresting device are required to improve the efficiency of deflecting an interfacial crack to an area where crack growth is restricted. Several attempts to improve the crack deflection behaviour are proposed based on modification of small features at the tri-material junctions of the face sheet, core and crack arresting device. Based on the TSA technique, the work presented in the thesis is the first to experimentally investigate the local effects developed at the original and the modified crack arresting devices, and to study the mechanisms that control crack propagation in the vicinity of the crack arresting devices.

1.4 Structure of the thesis

The thesis starts with a general overview of sandwich structures in Chapter 2, in which the structural concept, constituent materials and the manufacturing processes are specified. A description of debond damage is provided which underlines its importance in a damage tolerance context. Current knowledge on the fracture characterisation of a bi-material interfacial crack is summarised, which is followed by an introduction of the crack arresting methods developed for foam cored composite sandwich structures. This emphasises the importance of using full-field measurement techniques to characterise the fracture behaviour. Finally, full-field measurement techniques that have been used for the study of fracture are reviewed and a comparison of different techniques is provided. The selection of IR imaging techniques as a tool for assessing the fracture behaviour for foam cored composite sandwich structures is discussed and justified.

Chapter 3 introduces the theory of IR thermography and TSA. The difficulties caused by specimen motion in TSA are discussed. A review of current MC approaches for TSA is provided, which shows the necessity to develop a new MC method for fracture characterisation in sandwich structures. The FLIR thermal imaging system used in this project is described. The temperature calibration routine developed in [24] is described which enables the IR camera to be used outside its usual operating condition with high frame rates. Together, Chapters 2 and 3 establish the background and motivation for the current work.

Chapter 4 proposes a high spatial resolution MC method based on digital image correlation (DIC). The experimental validation of the MC method is conducted using IR lenses with different resolutions. It is shown that the MC method can significantly

improve the accuracy of TSA, especially when a magnifying lens is used. For practical considerations, the feasibility of the MC method for fatigue test in TSA is investigated.

TSA with the MC method is used to establish the stress state around an interfacial crack for a foam cored sandwich composite in Chapter 5. It is shown that the erroneous assessment of the stress field due to complex specimen motion is significantly improved and the results show a good agreement with FE modelling. The results obtained from the magnifying lens show that TSA can provide high resolution quantitative information regarding the crack tip stress fields in foam cored sandwich composites.

Chapter 6 proposes an experimental method for obtaining the fracture toughness of an interfacial crack in sandwich structures. The method relates the interfacial fracture toughness with the crack front temperature change developed during fracture. An experimental approach that uses high speed IR thermography to capture the temperature evolution during the crack growth is developed. For foam cored sandwich composites, it is shown that IR thermography with a frame rate of 15 kHz can make a quantitative measurement of the crack front temperature associated with the crack growth. It is shown that the measured temperature change per unit area is proportional to the interfacial fracture toughness.

Chapter 7 examines the crack path at the tri-material junction resulting from the inclusion of the crack arresting device in a sandwich structure subjected to static loading. Investigations are performed under mode I loading conditions. Modifications of the crack arresting device are proposed and tested to achieve the desired crack path. FE models containing different crack arresting devices are validated by the load-displacement data obtained from the static tests.

Chapter 8 studies the mechanisms that result in the crack path observed from the different crack arresting devices. The local effects (or local stress concentrations) introduced by the different crack arresting devices at the tri-material junction are studied using TSA under cyclic loading. To promote stable crack propagation in the fatigue tests, a test methodology that allows the crack to propagate under a controlled energy release rate is proposed based on the validated FE model. For the original and modified crack arresting devices, results obtained from TSA show different stress states when crack propagates in the vicinity of the crack arresting device. It is shown that the stress states are related to different crack paths at the crack arresting devices. Finally, the efficiency of the different crack arresting devices is demonstrated.

The overall conclusion of the current work and recommendations of future work is presented in Chapter 9.

Chapter 2

Interfacial fracture in foam cored sandwich structures

2.1 Sandwich structure concept and materials

Sandwich structures are formed by attaching two thin but stiff face sheets to a thick but lightweight core material as shown in Figure 2.1 (a). The typical material choice and location in sandwich structures can be compared to an ordinary I-beam concept (Figure 2.1 (b)), in which the face sheets and core perform the same functions as the flange and web of the I-beam respectively. The separation of face sheets by a thick but lightweight core increases the second moment of area with little increase in weight thereby providing high structural efficiency for resisting bending and buckling loads. In both I-beam and sandwich structures, the flange and face sheets carry normal stresses while the web and core resist shear stresses. The difference is, in sandwich structures, the adhesive attachment between the face sheet and the core needs to be strong enough to transmit axial and shear loads between the components. The major advantage of sandwich structures compared to the I-beam is that the structural efficiency can be expanded to panels, shells or other complex structures, while the I-beam concept can be only carried out at beam level.

One important feature of sandwich structures is the possibility of tailoring properties with different constituting materials according to the applications and performance requirements. A large variety of materials have been developed for both face sheets and core. A large number of materials are available for the face sheet since the introduction of fibre composites, and the number of core materials has also increased drastically with the

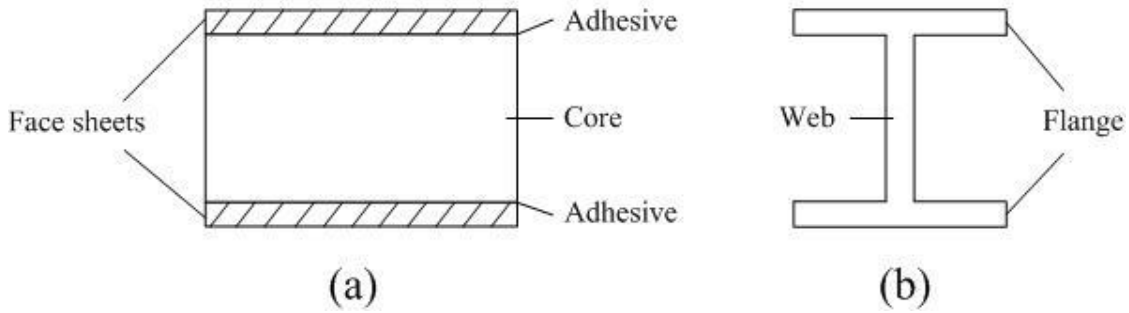

Figure 2.1: Schematic of sandwich structure and I-beam

development of more and more competitive cellular plastics [1]. The selection of appropriate constituent materials for different applications is therefore of great importance to the efficient design of sandwich structures.

The face sheet materials used in sandwich structures require high tensile and compressive strength and stiffness to counteract the external bending moment. Materials used for the face sheet can be mainly divided into two groups: metals and composites. The former group includes aluminium alloys, stainless steel and titanium, while the group of composites are dominated by fibre reinforced plastic (FRP). Compared to metals, the advantages of composites are their low weight, high strength and stiffness, tough face sheet/core bonding, high fatigue strength, good durability in hostile environments and flexible material tailoring.

Since the fibres occupy the most volume in FRP and carry most of the applied load, the properties of FRP are mainly determined by the choice of fibres. The most used reinforcing fibres are glass, carbon and aramid. The properties for different types of high performance fibres are listed in Table 2.1 [27]. In general, carbon fibres offer the highest strength and stiffness. The very high cost of carbon fibres however restricts their applications usually to the aerospace and aircraft industries. The tensile strength and modulus of aramid fibres are superior compared to that of glass fibre due to the low density, but inferior to that of carbon. The major shortcoming of aramid fibres is their low compressive strength, which is much lower than that of glass and carbon fibres. Compared to carbon and aramid, glass fibres provide the modest properties but with very low cost so are prevailing in a wide range of applications including ship structures and wind turbine blades [28, 29].

The primary functions of matrix materials are to transfer stresses between reinforcing fibres and protect the reinforcement from adverse conditions. In sandwich structures, the matrix also acts as the adhesive which bonds the face sheet and the core material. Two commonly used matric systems in FPR and sandwich structures are polyester and epoxy.

Table 2.1: Comparison of properties for high performance fibres [27]

Property	Units	Glass E-Glass	Glass S-2 Glass	Aramid K49	Carbon T700SC
Density	g/cm^3	2.58	2.46	1.45	1.8
Tensile strength	MPa	3445	4890	3000	4900
Tensile modulus	GPa	72.5	86.9	112.4	230
Compress. strength	MPa	1080	1600	200	1570
Strain to failure	%	4.8	5.7	2.4	1.5
Price	$/kg	2	20	30-50	40-60

The comparison of these two matrices is shown in Table 2.2 [30]. The major problem of polyesters is their high curing volume shrinkage which can introduce high interlaminate/interface shear stresses and severely decreases the adhesive strength.

The core in sandwich structures must have low density to minimise the total weight of the structure and provide a good adhesive performance. In addition, the core materials must be capable of carrying the transverse shear stresses and through thickness compressive stresses to prevent the shear failure and stabilise the face sheets against buckling and wrinkling [31]. Three main types of core materials are balsa wood, aluminium honeycomb and polymer foam as shown in Figure 2.2. Balsa wood offers several advantages including high compressive stiffness, good adhesive performance and low cost. However, as a natural material, the density of balsa is difficult to control and it is easily subjected to moisture attack which results in a significant decrease of the mechanical properties [1]. Balsa is usually applied to the applications where local high stresses are required or weight saving is not important. Aluminium honeycomb has the highest mechanical performance in all core materials compared to the weight. Because of the high cost, aluminium honeycombs are mostly used in the aircraft and aerospace industries. Polymer foams are relatively new core materials. They are usually manufactured from a wide range of synthetic polymers. The polyvinyl chloride (PVC) foam is currently the most popular foams which can be used in both ductile (linear foam structure) and brittle version (crosslinked foam structure) [32, 33]. The broad selection of different foams as well as the extensive density range makes polymer foams suited to a variety of applications. In many areas such as ship structures, wind turbine blades and aircraft components (the secondary structures such as the bulkhead and access panels), polymer foam cores have started to replace the traditional balsa wood and aluminium honeycomb to provide more cost-effective and weight-efficient structures [5, 34, 35].

Table 2.2: Comparison of properties for matrix materials [30]

Matrix	Strength	Curing shrinkage	Chemical resistance	Temperature resistance	Cost
Polyester	low	high	poor	good	low
Epoxy	high	low	good	poor	high

Figure 2.2: Sandwich core materials: (a) polymeric foam, (b) aluminium honeycomb and (c) balsa wood

The particular sandwich structures studied in this work comprising glass fibre/epoxy composite face sheets and PVC foam core. As described above, sandwich structures with these constituent materials are currently widely used in wind turbine blades and ship structures. Thus, understanding the damage tolerance of this kind of sandwich structure is of great importance in structural design.

2.2 Manufacture of foam cored sandwich composites

Sandwich structures are manufactured by adhesively bonding the face sheets and the core material together. For metallic face sheet, bonding is achieved by directly applying the adhesive layer (usually the liquid resin or highly vicious film) interleaved between the face sheets and the core. When sandwich structures are made of composite face sheets, the commonly used manufacturing approaches are: wet lay-up, resin infusion moulding (RIM) and prepreg lay-up.

In the wet lay-up approach, the fibres are laid directly onto the core and resin in liquid form is impregnated manually by rollers or brushers [36]. A vacuum can be applied after all the components have been impregnated to improve surface finish and consolidation, but typically it is left to cure in the open [37]. The process is very simple and has a low

tooling cost. However, the product quality can vary greatly which is highly dependent on the skill of the workers. Due to the low product repeatability and high labour cost, this approach is suited for very short production series and where the structural performance is of secondary importance.

In the RIM approach (see Figure 2.3), fibre reinforcements together with the core are positioned on the mould and the liquid resin is infused into the sandwich perform using application of a vacuum. A distribution mesh layer is placed over the top and bottom of the preform which allows a uniform resin flow through the part. During the infusion process, the use of vacuum minimises air bubbles in the resin while the applied uniform pressure from the vacuum bag ensures a high fibre volume fraction with low void content. This leads to an improved structural performance and quality repeatability compared with the wet lay-up approach. However, the RIM approach still potentially has resin- and void-rich areas. This can be mainly caused by several reasons: 1) the dry fibres can shift during vacuum infusion; 2) the resin non-uniformly flows through the preform with different speeds; 3) the applied pressure is limited by one atmosphere. The RIM approach is popular for producing large and geometrically complex structures due to its low cost and healthy work environment.

The prepreg approach applies the similar lay-up as the RIM, except that the fibre has been impregnated by highly viscous or solid resin and hence no additional resin is needed during the manufacturing. The use of prepreg provides the controlled fibre to resin ratio, but almost all the resins used for prepreg require well controlled high temperature and pressure to achieve intended properties. For consolidation, the curing usually occurs under a vacuum bag and with heat applied; in high performance (e.g. high fibre and low void content and good face sheet/core bonding) applications autoclaves are normally used to introduce higher pressure. Since the short flow distance, controlled resin content and high consolidation pressure, the prepreg approach offers sandwich composites with the highest repeatability and excellent mechanical properties. However, the requirements for the high temperature and pressure make the tooling cost significantly higher than with the other manufacturing approaches. This approach is commonly used in the aerospace industry, where the need for high structural performance can motivate the high cost.

The manufacturing process has been shown to clearly influence the performance of sandwich structures. The applied compaction pressure is important to ensure high fibre and low void content while evacuation is necessary to remove air and volatiles produced during the curing process. In the work described in this thesis, the RIM approach is used for two reasons: 1) this approach is capable of providing repeatable product quality with relatively low costs; 2) the widespread use of this approach in the manufacture of current wind turbine blades [36, 38] as RIM is more suited to large structure manufacture.

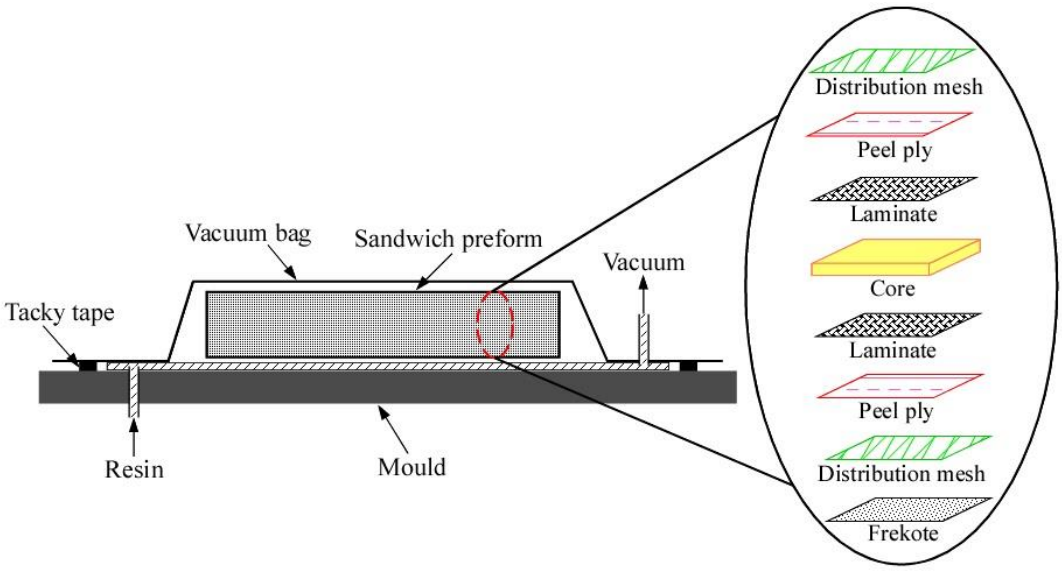

Figure 2.3: Schematic of sandwich panel manufacturing using RIM

2.3 Face sheet/core debond damage

In sandwich structures, debonding between the face sheet and the core can initiate as a result of manufacturing defects in the manufacturing process or a mismatch in the geometry. Debonds may also arise during service caused by impact events, overload or structural fatigue.

Experience from current ship structures and wind turbine blades, using foam cored sandwich composites, has shown that the face sheet/core debonding is one of the most common and critical damage types. Sorensen *et al*. [39] investigated the potential failure modes in wind turbine blades by testing a 25 m wind turbine blade to failure (the blade had undergone a full-scale loading equivalent to a 20 years fatigue life). The applied load is in the flap-wise direction as shown in Figure 2.4 (a), leading to a significant deflection of the blade (along z direction) during the test. Different types of damage were observed by post mortem examinations of the failed sections of the blade. For sandwich structure parts of the blade, the face sheet/core debonding was seen as the major damage in the blade that occurred inside the surface of the downwind skin and the main spar outer surface (see Figure 2.4 (a)). Figure 2.4 (b) shows the observed debonding damage in the main spar web, where the debond propagates along the interface and completely separates the face sheet and the core. In the application of ship structures, the face sheet/core debonding is seen also as the major damage type which can be introduced from different in service loads. Figure 2.5 (a) shows an example of the debonding damage after removal of the face sheet [40]. The debond was caused by the slamming event acting on the keel

where the core shear failure occurred first and then the crack propagated up to the interface. The debonding damage in Figure 2.5 (b) was introduced from the impact event on the keel location and the propagation of the debonded are effectively removed the face sheet from the core material [40].

Common to the above examples is that the debonding damage can propagate to a fairly large part of the structure if continued service loads are applied. This underlines the importance of debonding in the damage tolerance context as undetected propagation of the debonded area can result in complete loss of load carrying capacity of the sandwich structures. In service, the structural performance of a debonded sandwich structure can be reduced in three different ways:

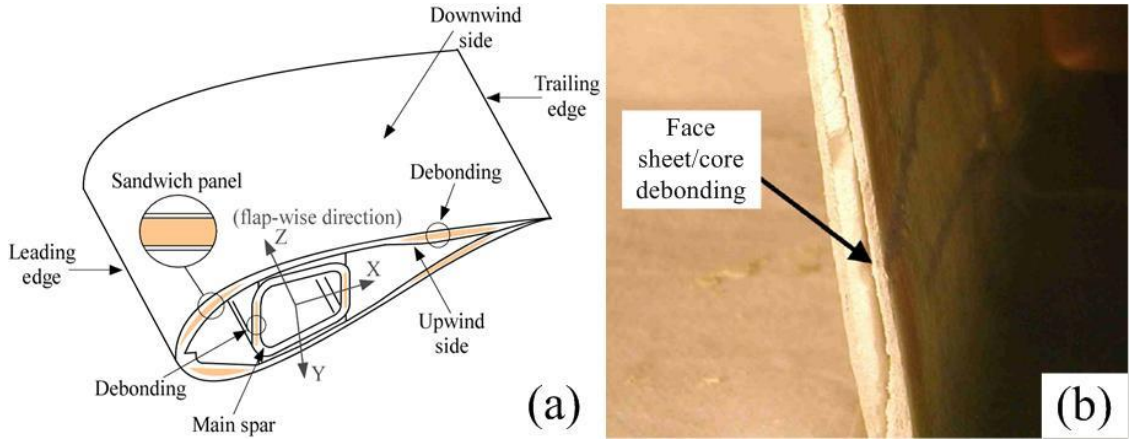

Figure 2.4: (a) the main elements of a wind turbine blade and (b) the observed face sheet/core debonding in the failed blade section [39]

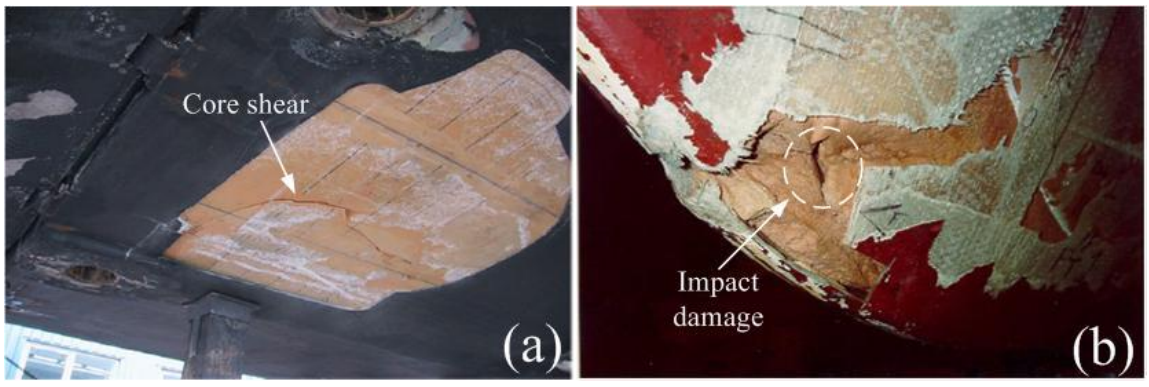

Figure 2.5: Examples of the face sheet/core debonding occurred in ship structures caused by (a) the slamming event and (b) the impact event [40]

1. Buckling: the face sheet over the debonded area may buckle under compression allowing the rapid propagation of the debonded area [41].

2. Kinking: the debonding damage propagates into the core and results in through thickness core shear failure.

3. Separation: the crack growth is unstable along the interface, which results in complete separation of the face sheet and the core.

The propagation of the debonded area increases the criticality of the damage which can result in a fatal failure of the structure. While structures with debonding are perceived to be no longer operating in their ideal condition [10-13], they can still operate acceptably over some time [42]. The questions regarding to the damage tolerance of the debonded sandwich structure now emerge:

1. When does the debonded area start to propagate?

2. How does the debonded area propagate in sandwich structures?

3. Is the damage critical to the structure?

It is clear that the above questions are mainly related to knowledge of the interfacial fracture behaviour in sandwich structures. To simulate the debond propagation, crack tip parameters and mechanisms associated with the crack initiation and propagation must be established. The following section therefore provides a review of the current knowledge on interfacial fracture in sandwich structures.

2.4 Characterisation of interfacial fracture

2.4.1 General bimaterial fracture mechanics

According to the first law of thermodynamics, when a system goes from a non-equilibrium state to equilibrium, there will be a decrease in potential energy. In 1920 Griffith applied this theorem for fracture and proposed the energy balance concept which established the foundations of fracture mechanics [43].

In Griffiths theory, a new state is developed at the instant following the formation of a crack. The new state can be a non-equilibrium state in which the potential energy is reduced by the attainment of equilibrium; or it is an equilibrium state where the energy does not change. Thus, a crack may form (or an existing crack may grow) only if such a process causes the total energy to decrease or remain constant. When the critical condition for fracture is considered (the crack growth under equilibrium conditions), the

following energy balance can be formed for an incremental increase in the crack area, dA [44]:

$$\frac{d\Lambda}{dA} = \frac{d\Pi}{dA} + \frac{dW_S}{dA} = 0 \tag{2.1}$$

where Λ is the total energy, Π is the potential energy supplied by internal strain energy and external forces and W_S is the energy required to create new surfaces. This energy balance shows that a crack may be formed or propagated if the potential energy resulting from crack growth is large enough to overcome the energy required by the new crack surfaces. This energy balance is also called Griffith energy balance.

In 1956 Irwin defined the energy release rate, G, as a measure of the energy available for an increment of crack extension [45]:

$$G = \frac{d\Pi}{dA} \tag{2.2}$$

and based on the Griffith energy balance, the critical energy release rate, G_C, is defined as [45]:

$$G_C = \frac{dW_S}{dA} \tag{2.3}$$

The critical energy release rate is also called the fracture toughness of the material.

Generally, the load applied to a crack can be defined by three modes as shown in Figure 2.6. These modes include the opening mode (Mode I), the sliding mode (Mode II) and the tearing mode (Mode III). When a 2D model is used, only the first two modes are typically considered.

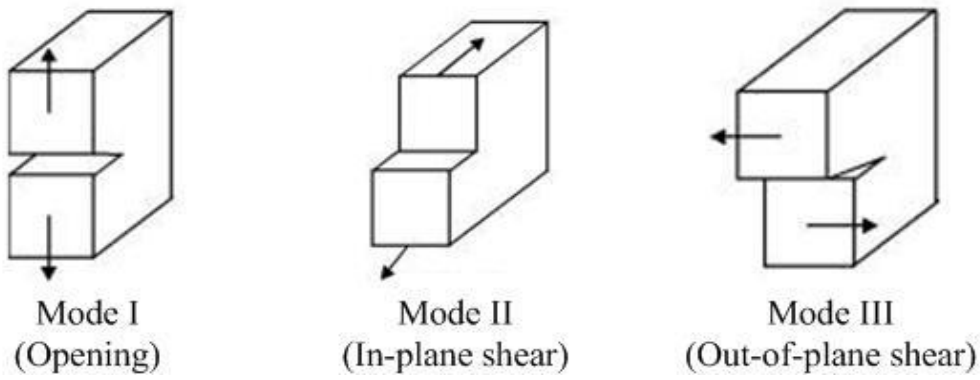

Figure 2.6: Fracture modes

For foam cored sandwich composites, the face sheet/core debonding problem can be modelled as a 2D interfacial crack between two dissimilar orthotropic materials. The crack geometry is shown in Figure 2.7 where the crack tip is located at $x, y = 0$. The displacement field close to the crack tip along the x axis can be specialised to describe only the opening (δ_y) and sliding (δ_x) relative displacement of the crack flanks as [40]:

$$\sqrt{\frac{H_{11}}{H_{22}}}\delta_y + i\delta_x = \frac{2H_{11}K|x|^{\frac{1}{2}+i\epsilon}}{\sqrt{2\pi}(1+2i\epsilon)\cosh(\pi\epsilon)} \tag{2.4}$$

Likewise, the stress state as normal σ_{yy} and shear σ_{xy} stresses in front of the crack tip can be described as follows [40]：

$$\sqrt{\frac{H_{22}}{H_{11}}}\sigma_{yy} + i\sigma_{xy} = \frac{Kx^{i\epsilon}}{\sqrt{2\pi x}} \tag{2.5}$$

where H_{11}, H_{22} and the oscillatory index ϵ are bimaterial constants determined from the elastic stiffness of material 1 and material 2 (a detailed description is given in [40]), $i = \sqrt{-1}$ and $x^{i\epsilon} = \cos(\epsilon \ln x) + i \sin(\epsilon \ln x)$ which is so-called oscillatory singularity and is responsible for the violently oscillatory of the stress and displacement fields that are not present in the elastic fracture mechanics of homogeneous solids. K is the complex stress intensity defined as:

$$K = K_1 + iK_2 \tag{2.6}$$

where K_1 and K_2 are mode I and mode II stress intensity factors respectively. In theory, the stress singularity at the infinitely sharp crack tip ($x = 0$ in equation 2.5) can result in the infinite stresses at the crack tip. For this reason, the theoretical stress value at the crack tip is usually described by the complex stress intensity factor and the crack tip mode-mixity.

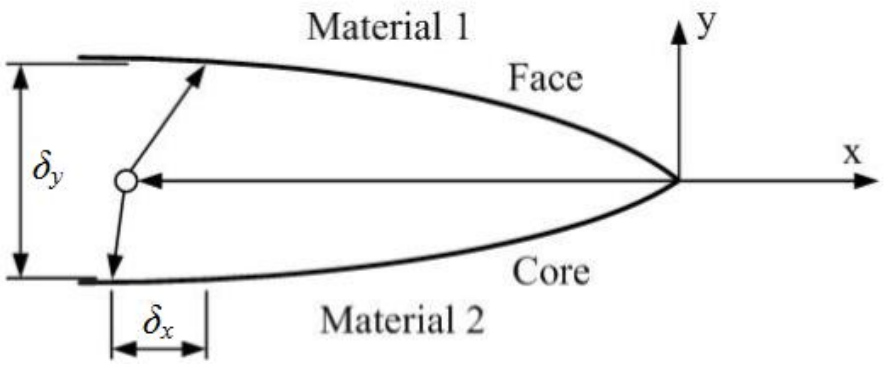

Figure 2.7: Sandwich bimaterial crack tip geometry

The mode-mixity is a parameter that quantifies the amount of the shearing stress at the crack tip and the direction of the shear stress. The mode-mixity as suggested by Hutchinson and Suo [46] can be defined in terms of the complex stress intensity factor as:

$$\varphi = \tan^{-1}\left[\frac{\Im(K\hbar^{i\epsilon})}{\Re(K\hbar^{i\epsilon})}\right] \tag{2.7}$$

where $\Im[K\hbar^{i\epsilon}]$ and $\Re[K\hbar^{i\epsilon}]$ are the imaginary and real components of the stress intensity factor, and $\hbar$ is the characteristic length of the crack problem which is usually chosen as the face sheet thickness [40]. It should be pointed out that the mode-mixity as defined in equation (2.7) is expressed by the angle from -90° to 90°. The angle equals 0° implies a pure mode I loading is applied to the crack tip. When the angle is increased from 0° to 90°, the mode II dominated loading increases and the positive sign of the angle indicates a positive shear stress ahead of the crack tip. Conversely, the negative sign of the angle presents the negative shear stress ahead of the crack tip and the amount of the negative shear stresses increase with the decrease of the angle from 0° to -90°.

The energy release rate can be related to the complex stress intensity factor by [47]:

$$G = \frac{H_{11}|K|^2}{4\cosh^2(\pi\epsilon)} \tag{2.8}$$

According to the displacement field stated in equation (2.4), the mode-mixity and energy release rate can be expressed in terms of the relative crack flank displacements as [40]:

$$\varphi_F = \tan^{-1}\left(\sqrt{\frac{H_{22}}{H_{11}}}\frac{\delta_x}{\delta_y}\right) - \epsilon\ln\left(\frac{|x|}{\hbar}\right) + \tan^{-1}(2\epsilon) \tag{2.9}$$

$$G = \frac{\pi(1+4\epsilon^2)}{8H_{11}|x|}\left(\frac{H_{11}}{H_{22}}\delta_y{}^2 + \delta_x{}^2\right) \tag{2.10}$$

It is shown in above equations that the oscillatory singularity $x^{i\epsilon}$ is filtered out. The mode-mixity and the energy release rate are only functions of the relative opening and sliding displacements at the crack flank. Based on the relationship, the finite element (FE) method may be used to calculate the relative nodal displacements of the crack flanks, and hence determine the mode-mixity and the energy release rate. However, at the bi-material interface, the energy release rate/mode-mixity close to the crack tip will behave in an oscillatory manner as shown in Figure 2.8 [48]. The oscillation is physically impossible as in the FE solution, the upper and lower surfaces of the crack will wrinkle and penetrate into each other close to the crack tip. To avoid the mathematical oscillatory error, several methods have been proposed in the literature. These methods include the virtual crack extension method [49], the virtual crack closure technique [50], the crack surface

displacement method [49] and the crack surface displacement extrapolation method (CSDE) [40]. A comparison of these methods was provided by Berggreen [40] in which the CSDE method was proved to be very robust and stable for different bimaterial interfaces and loading conditions.

In some studies the mode-mixity is derived from a reduced formulation to simply by-pass the oscillation and interpenetration problems [51]. For this case, the oscillatory index ϵ is assumed to be 0. Thus, the mode-mixity becomes:

$$\varphi_R = \tan^{-1}\left(\sqrt{\frac{H_{22}}{H_{11}}}\frac{\delta_x}{\delta_y}\right) \tag{2.11}$$

However, the CSDE method is required to derive the mode-mixity from a full formulation (equation (2.9)) as well as the energy release rate. The CSDE method is schematically illustrated in Figure 2.8. As observed in numerous investigations, the variation of the displacement field in the transition zone (evaluation zone) from the outer border to the inner border is almost linear. In the CSDE method the displacement field in the transition zone is identified and is linearly extrapolated into the crack tip (see the red line) to avoid the oscillatory error zone. This method is used throughout this thesis for determination of the crack tip mode-mixity and energy release rate from a FE manner.

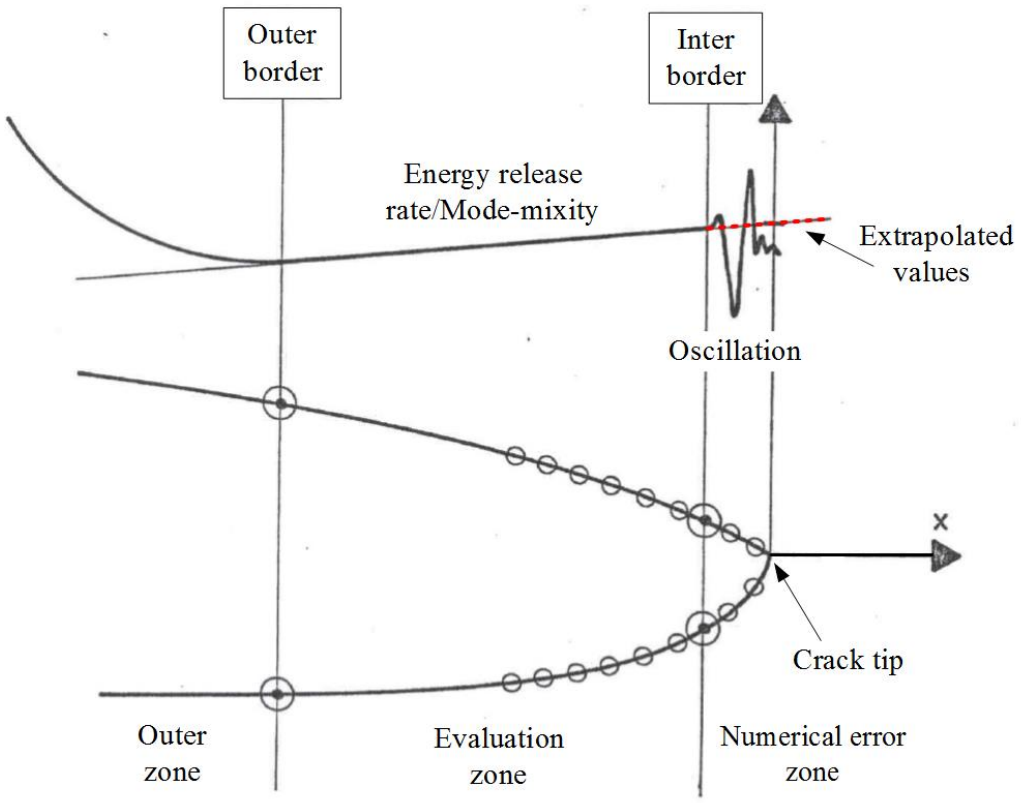

Figure 2.8: Schematic illustration of the CSDE method

The theory described above provides a fundamental knowledge for the analysis of the interfacial fracture in sandwich structures. The theory is based on linear elastic fracture mechanics (LEFM) which assumes that the plastic deformation zone close to the crack tip is highly localised and small compared to the crack length.

2.4.2 Fracture toughness

Fracture toughness, defined by the critical energy release rate, is a parameter that quantifies the minimum energy required to increase the crack in a unit area of a specimen. By this definition, for quasi static crack propagation, the energy criterion for fracture can be formulated as:

$$\frac{1}{b}\frac{\partial(W_{ext}-U)}{\partial a} \geq G_C \tag{2.12}$$

where b is the specimen width, W_{ext} and U are the work done by the external forces and the elastic strain energy respectively and a is the crack length.

If the material exhibits linear elastic behaviour, the fracture toughness can be estimated from equation (2.10). The values of δ_y and δ_x can be estimated from the FE model using the loading condition that the critical load (P_C) at the onset of crack propagation is applied. The critical load for crack propagation can be obtained experimentally.

Another method that can be used to calculate the fracture toughness is based on equation (2.12). As shown in Figure 2.9 (a), a specimen with an initial crack length, a, is loaded under constant loading. In this case, the load-displacement curve is illustrated in Figure 2.9 (b). Thus, the change of the elastic strain energy and the work done by external force can be written as:

$$\Delta U = \frac{P(d\delta)}{2}, \Delta W_{ext} = P(d\delta) \tag{2.13}$$

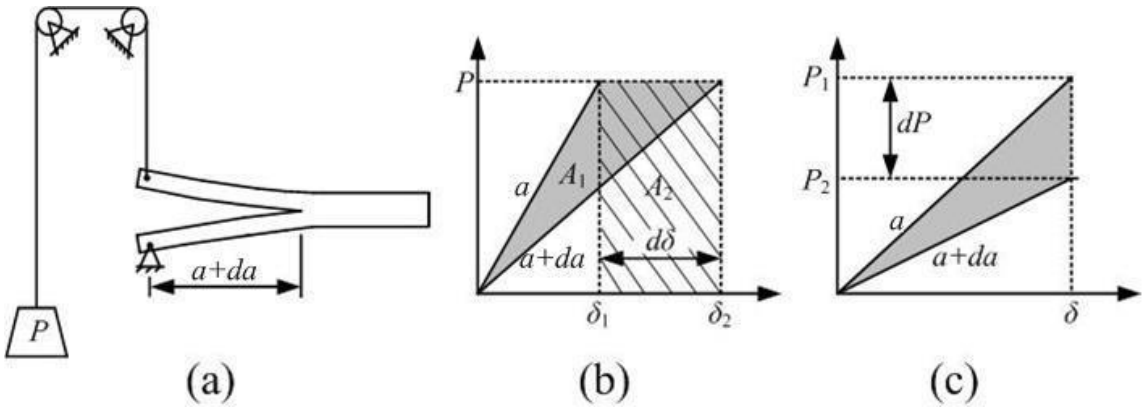

Figure 2.9: Energy required for the increment of an existing crack at constant load control and constant displacement control

Substituting equation (2.13) into (2.12), under the critical conditions for fracture, the fracture toughness of the specimen for constant load control is:

$$G_{PC} = \frac{P}{2b}\left(\frac{\partial \delta}{\partial a}\right) \tag{2.14}$$

If the specimen is loaded under constant displacement control, as illustrated in Figure 2.9 (c), the work done by external forces and the elastic strain energy becomes:

$$\Delta U = -\frac{\delta(dP)}{2}, \Delta W_{ext} = 0 \tag{2.15}$$

Thus, the fracture toughness of constant displacement control is:

$$G_{\delta C} = \frac{\delta}{2b}\left(\frac{\partial P}{\partial a}\right) \tag{2.16}$$

At this point, the compliance, *C*, is introduced which is defined as:

$$C = \frac{\delta}{P} \tag{2.17}$$

Substituting the compliance into equations (2.14) and (2.16) respectively, the fracture toughness for both constant load and displacement control can be expressed as:

$$G_C = \frac{{P_C}^2}{2b}\left(\frac{\partial C}{\partial a}\right) \tag{2.18}$$

where P_C is the critical load at the onset of crack propagation. The compliance of the structure in equation (2.18) is determined analytically as a function of the crack length. When the critical load for crack propagation is obtained, the fracture toughness of the material can be calculated. However, it should be noted that the derivation of the analytical solutions based on equation (2.18) is generally complex and possibly elusive for sandwich materials due to the complex loading configuration and specimen geometry.

The FE and analytical methods described above are based on LEFM for calculating the material fracture toughness. In recent years much effort has been made to determine the fracture toughness for an interfacial crack in sandwich structures. The aim is to quantify the ability of debond damage to resist fracture. A review of those studies is provided in the next section.

2.4.3 Characterisation of interfacial fracture toughness

In homogeneous materials it is known that a crack mostly propagates in pure opening mode even if there is an initial mixed-mode loading at the crack tip. However, when the crack is at the bimaterial interface, the asymmetries of moduli and Poisson's ratios along

the interface usually force the crack to propagate in a mixed-mode condition. A strong dependency of the fracture toughness on the mode-mixity has been found in several studies [16, 52]. The consequence of this dependence is that the complete distribution of the fracture toughness under different mode-mixity is needed for characterising the interfacial fracture behaviour.

A number of test specimens have been developed during the last two decades for determining the interfacial fracture toughness of sandwich structures. Test specimens such as the cracked sandwich beam (CSB), three-point sandwich beam (TPSB), double cantilever beam (DCB) and the end-loaded sandwich specimen (ELSS) have been commonly adopted as the mode I or mode II dominated fracture test specimens [53-56]. Recently, several specially designed testing approaches have been proposed by which the interfacial fracture toughness can be studied over a certain range of loading mode-mixities.

Li and Carlsson [57] introduced the tilted sandwich debond (TSD) configuration for characterising the mixed-mode interfacial fracture toughness of sandwich structures. The specimen and loading configuration is shown in Figure 2.10 (a) where the mode-mixity at the crack tip can be varied by changing the tilt angle of the rigid based. Analysis, however, shows that very limited mode-mixity can be obtained from this specimen over a range of tilt angles from -15° to 20° [57, 58]. Shivakumar and Smith [59] studied the fracture toughness of TSD specimens with different PVC foam cores (H45, H100 and H200). The results showed a roughly monotonic increase in the interfacial fracture toughness with the increase of the core density. A modified TSD approach was later developed by Berggreen and Carlsson [60], which extends the range of mode-mixity by reinforcing the upper face

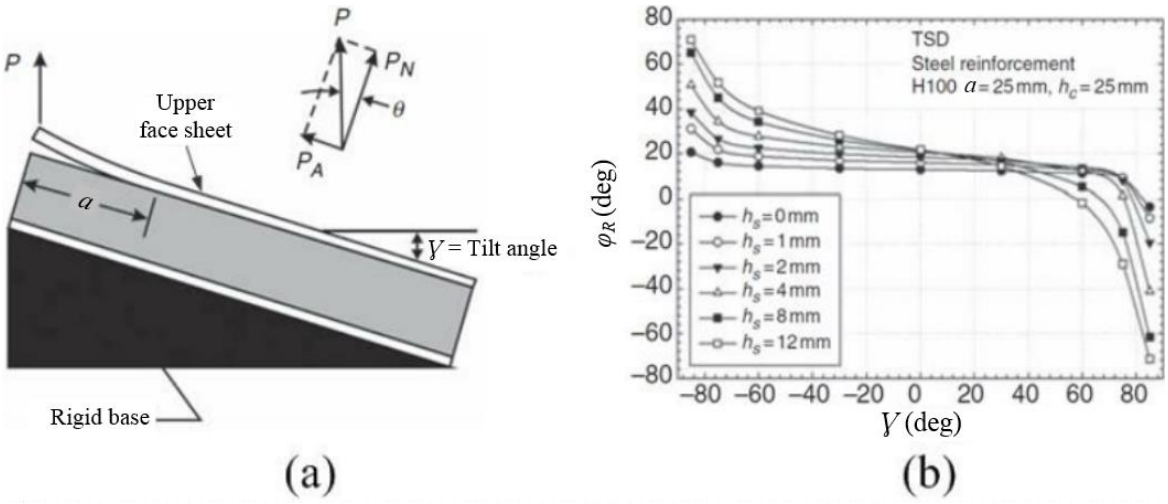

Figure 2.10: (a) Schematic representation of the TSD specimen and (b) the mode-mixity range with different face sheet reinforcement thickness [57, 60]

sheet with a stiff metal plate. As their results show in Figure 2.10 (b), a large increase of the mode-mixity range was observed with the increase of the reinforcement thickness (h_s). The mode-mixity at a fixed tilt angle was studied that was influenced by the variation in the crack length, but was less sensitive to the material parameters (thickness and stiffness) of the face sheet and the core.

Quispitupa *et al*. [61] proposed the mixed mode bending (MMB) test rig (see Figure 2.11 (a)) where various crack tip mode-mixities can be obtained by changing the lever arm distance, *c*. The mode-mixity range obtained from the MMB loaded sandwich specimens was studied which is smaller than that obtained from the modified TSD specimens. However, it was reported in [62] that a full set of mode-mixity can be achieved by changing the thickness of the core material. Unlike the TSD specimen, the mode-mixity of the MMB specimen is unaffected by the crack length when the ratio of a/L larger than 0.2 [62]. For a sandwich structure loaded in the MMB rig, the analytical solution for G_c was developed based on equation (2.18) [62]. The analytical solution was compared with

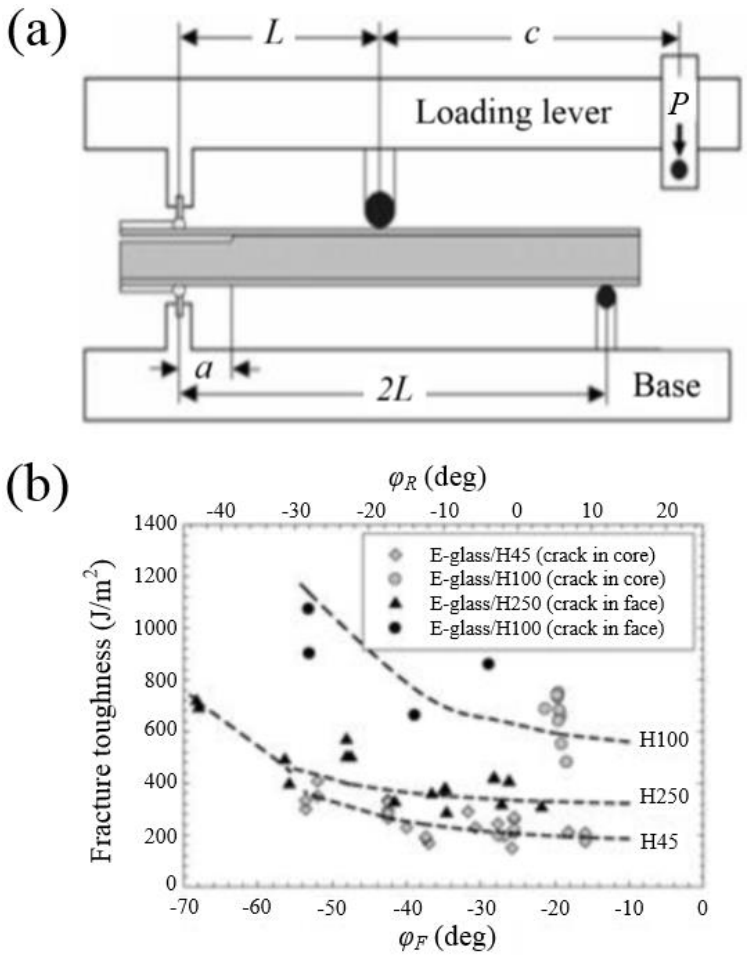

Figure 2.11: (a) Schematic representation of the MMB rig and (b) interface fracture toughness at various mode-mixities for MMB specimens with different foam density [63]

the FE solution and showed good agreement. In [63] the analytical solution was used to evaluate the interfacial fracture toughness of the MMB specimens with GFRP face sheets and PVC H45, H100 and H250 foam cores. A summary of the results is shown in Figure 2.11 (b). The interfacial fracture toughness is seen increasing with the increased mode II dominated loading. The fracture toughness shown in the plot is independent of the toughness of the core material, which is in contradiction to the results obtained by Shivakumar and Smith [59] as reviewed above. It was explained that the crack propagation mechanism might be changed when propagation path for H250 foam specimens shifts to the face sheet/core interface rather than just below the interface on the core side. However, it can be observed in Figure 2.11 (b) that when the crack grew in the face sheets, the fracture toughness obtained from H100 foam specimens is still higher than that obtained from the specimens with H250 foam core. The mechanisms behind this is shown not well understood which lead to less confident of current results.

Østergaard *et al*. [64, 65] developed the double cantilever beam specimen loaded with uneven bending moments (DCB-UBM) for studying the interfacial fracture toughness of sandwich structures. The test rig configuration for the DCB-UBM specimen is shown in Figure 2.12. As reported in [64] the entire mode-mixity range ($-90° < \varphi < 90°$) can be obtained by changing the moment ratio, M_1/M_2. In [65] interfacial fracture toughness was determined from the DCB-UBM specimen based on the FE modelling. Sandwich specimens consisting of GFRP face sheets and different density foam cores (H80 and H130) were studied. In their results the fracture toughness under mode II dominated loading is shown to be higher when compared to that under mode I dominated loading. The fracture toughness increased with increasing foam density.

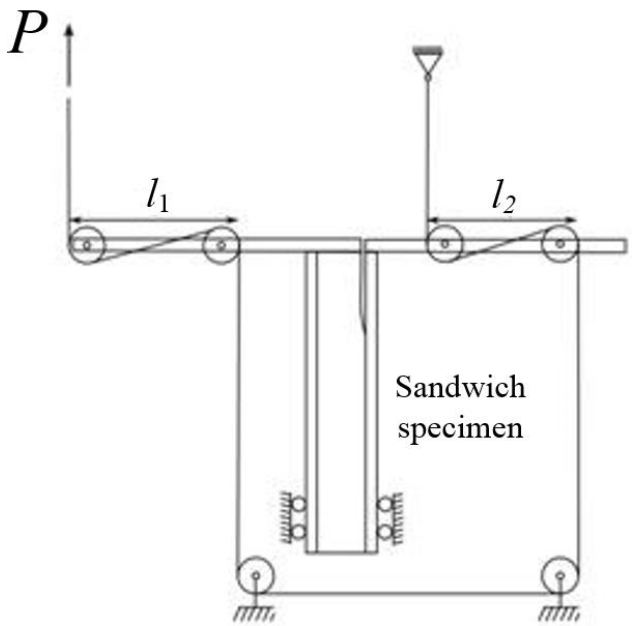

Figure 2.12: Schematic representation of the DCB-UBM specimen [64]

A detailed review of the test methods that can be used to characterise the mixed-mode interfacial fracture toughness has been provided. The main characteristics of the different test methods is summarised in Table 2.3. The TSD method is unsuited to be applied to fatigue tests as the crack growth rate cannot be accurately characterised when the mode-mixity changes with the crack length. The disadvantage of MMB method is that specimens with different dimensions must be tested for achieving the full mode-mixity range, while the major disadvantage of the DCB-UBM methods is its complex loading configuration which cannot be easily manufacture or set up in a test machine, particularly for fatigue loading.

A common conclusion obtained from current studies is that the interfacial fracture toughness increases with mode II dominated loading and the increased foam density. However, results obtained from the MMB specimen with H250 foam show the opposite conclusions. It has been noticed that the change of the crack path may change the crack propagation mechanism, which results in the change of the fracture toughness. To achieve a thorough understanding of the interfacial fracture behaviour, it is important to build knowledge about the crack tip stress/strain fields as these can provide more detailed information regarding crack propagation.

It has been shown that the mixed-mode fracture toughness values derived from current test specimens are mainly based on the FE analysis. For MMB specimens, analytical solutions for fracture toughness have been derived. The predictions of the fracture toughness using the analytical and FE solutions have shown good agreement. The analytical solution also provides a simple way to calculate the fracture toughness. However, due to the complex loading configurations of the TSD and DCB-UBM specimens, no analytical solutions were developed for these specimens which can be used to examine the FE models and solutions. This results in unreliable results obtained from these methods. Furthermore, an accurate comparison between the fracture toughness values obtained from different test methods cannot be achieved. Thus, a method that can be applied to characterise the fracture toughness under different test configurations is needed.

For the reasons described above, measurement techniques which can characterise the crack tip stress/strain fields as well as the fracture toughness are required for the studies of the interfacial fracture behaviour in sandwich structures.

Table 2.3: Comparison of different mixed-mode fracture test methods

Test methods	Mode-mixity range	Mode-mixity characteristics	Increase mode-mixity range	Test configuration
TSD	Limited	Affected by crack length	Face sheet reinforcements	Simple
MMB	Limited	Unaffected by crack length	Different core thicknesses	Simple
DCB-UBM	Full range	Unaffected by crack length	Not required	Complex

2.5 Overview of interfacial crack arresting approaches

In section 2.3 it is shown that an initial face sheet/core debonding can propagate to a fairly large part of the structure, with the effective removal of the face sheet from the core. Propagation is often rapid and catastrophic due to the brittle behaviour of sandwich structures. From a practical point of view it is desirable that the propagation of the debond can be suppressed before the fatal collapse occurs, and therefore a part of the load carrying capacity of the structure can be retained. For foam cored sandwich composites, several solutions to prevent the interfacial crack propagation have been proposed in the literature.

The stitching technique is one approach to arrest the debond evolution. The principle of this technique is to stich the upper and lower face sheets together by means of the fibres. This approach has been shown to increase the fracture toughness for the face sheet/core interface and create the sandwich panel with high transverse strength and stiffness [66, 67]. However, this approach received only little attention in the literature due to the restrictions of their increased manufacturing complexities and costs for the application of sandwich structures.

Another approach for preventing the debond propagation was proposed by Grenestedt [68], which in principle is to remove the peeled face sheet from the entire structure thereby arresting the propagation of the debond to larger parts. As illustrated in Figure 2.13 (a), this approach applies separate face sheets to the core and the putty filled in between the face sheets (the V-shape groove) allows the removal of the front face sheet during the crack growth. The functionality of this approach has been verified through extensive tests in which the debonded area was shown effectively suppressed by

discarding the front face sheet from the structure [68, 69]. However, when the face sheets are discarded from the structure, it is implied that the sandwich structures will lose a huge part of its original bending stiffness and in-plane tension strength. In addition, this approach is unable to arrest the debond propagation if the interfacial crack kinks into the core before the debonded face sheet is peeled off (see Figure 2.13 (b)).

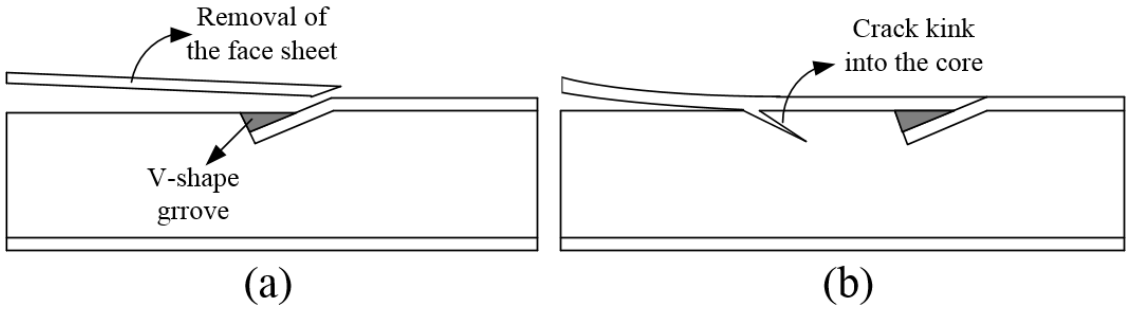

Figure 2.13: Two scenarios of the functional peeled face sheet (a) interfacial crack growth and (b) crack kink into the core

In several studies special structural elements called crack stoppers were embedded into the sandwich components to improve the strength and fatigue life of the structure. Hirose *et al*. [70] introduced a semi-circular shaped carbon fibre reinforced plastic (CFRP) rod in the face sheet/core interface. In their study a reduction in the crack propagation rate as the crack approached the crack stopper was observed. Rinker *et al*. [71] introduced the CFRP double-T joint element and the rectangular shaped CFRP element to the core structures. Sandwich structures with different embedded elements were investigated under fatigue loading and an increase of fatigue life expectancy was observed in the results. Common to these studies is that the structure/element introduced into the core was made from the FRP composites with stiffness quite different as the usual core materials, e.g. the PVC foam. However, the use of a high stiffness material for the crack stopper can result in an abrupt stiffness change around the crack stopper in which stress concentrations can be introduced and can potentially act as crack initiators. Furthermore, although the crack stoppers have shown the possibility to increase the strength and fatigue life of the structure, the debonded area cannot be confined/stopped in sandwich structures during crack propagation.

A sub-structural component called peel stopper was proposed by Jacobsen *et al*. [72] which was designed to inhibit the interfacial crack propagation by guiding the crack propagation path to a restricted area. As shown in Figure 2.14, the basic principle of the peel stopper is to utilise the wedge of the peel stopper to deflect the crack from the face sheet/core interface and guide it towards to a closed area bounded by the peel stopper. The ability of the peel stopper to deflect the interfacial crack was studied using the three-

point bending test configuration under both static and fatigue loading [72-74]. The crack path at the tri-material junction of the face sheet, core and the peel stopper has been shown to be highly dependent on the choice of the peel stopper material and the wedge angle. The interfacial crack was prone to deflect away from the face sheet/core interface with a relatively small wedge angle, and the material for the peel stopper was suggested to be compliant with large straining capability. In their work peel stopper was manufactured using a PolyUrethane (PU) material which has stiffness properties close to those of common foam core materials.

In this section the crack arresting approaches developed for foam cored sandwich structures have been summarised. The stitching technique is shown to be rather complicated with respect to manufacturing, while the approach which simply removes the debonded face sheets could largely diminish the overall stiffness and strength of the sandwich structures. The sub-structural components like the semi-circular CFRP rod and the rectangular shaped CFRP element are able to increase the fracture resistance of the structure. However, further propagation of the debonded area cannot be stopped using these approaches. Compared to the above methods, the peel stopper is able to confine the debonding damage to a restricted area and the structural integrity remains during the crack propagation. It is therefore regarded as an effective method for arresting the debonding damage in foam cored sandwich structures.

Although previous studies have shown the possibility to use the peel stopper to arrest the interfacial crack propagation, the capability of the peel stopper to deflect the interfacial crack is still less understood. The questions regarding how the interfacial crack behaves at the peel stopper under different loading conditions and how the small features at the tri-material junction affect the crack propagation behaviour must be addressed. These are essential to achieve a thorough understanding of the crack path at the tri-material junction and to further optimise the peel stopper design. For this reason, a full-field measurement technique that can be applied to characterise the local effects at the tri-material junction is appreciated.

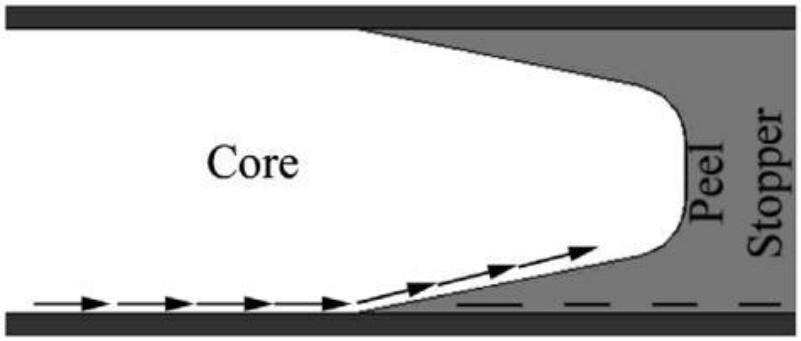

Figure 2.14: Schematic representation of the peel stopper principle

2.6 Optical measurement techniques for fracture mechanics

Sections 2.4 and 2.5 have demonstrated the importance to develop suitable measurement techniques for sandwich structures. Optical measurement techniques which can provide full-field measurements that related to the crack tip displacement/strain/stress/ temperature fields have been widely used to characterise the fracture behaviour. Some of those studies focus on the derivation of the stress intensity factor through the obtained crack tip displacement/stress fields [75-80] while others seek to understand the mechanisms associated with the crack initiation and propagation based on the measurements [81-85]. This section reviews some of the full-field measurement techniques that have been applied to fracture mechanics problems and a comparison of these techniques in terms of the applications of interfacial crack in sandwich structures will be presented.

2.6.1 Interferometric methods

Interferometry encompasses numerous techniques. Moiré interferometry and digital speckle pattern interferometry are the two main techniques which have been well developed for displacement measurements [81, 86]. The techniques are based on diffraction patterns formed when coherent light illuminates a structured surface. This surface can either be a mechanically applied grating pattern, or a random speckle pattern created when scattered laser light falls on a textured surface. Deformations in the structured surface can change the diffraction pattern and it is possible to correlate the two [86]. The techniques can be used to measure not only in-plane strains, but also out-of-plane displacements, and a very high displacement resolution can be obtained which is usually better than the micro scale. Applications of the techniques to fracture mechanics have been found mainly focusing on the near-tip displacement measurements in metallic materials where very small displacements around crack require measurements with sufficient sensitivity [81, 87-89]. Their high sensitivity, however, requires the isolation of the interferometer and specimens from environmental disturbances like vibrations, temperature gradients and even air currents and makes it hard to use the techniques outside an optical laboratory [86, 90]. In general these techniques require complex experimental setup with laser illumination and the post-processing of the fringes is often tedious and time-consuming.

2.6.2 Digital image correlation

Digital image correlation (DIC) measures displacements and indirectly, strains, by tracking the movement of an applied surface pattern during loading. The pattern is often formed by the white-light speckles which provide random and unique gray intensity

distributions on the surface of an object [91]. For DIC analysis, images containing random gray scales before and after deformation are collected and divided into numerous small areas called subsets. The basic idea behind is to match the maximum correlation of the gray distribution in each subset thereby obtaining the full-field displacement map. Applications of DIC to crack tip displacement and strain analysis have been found in different areas such as metals, composites and polymers [92-94]. The technique has the advantage that the deformation is directly sensed by the digital cameras which simplifies the optical setup, but the displacement resolution of DIC is usually lower than the interferometric methods. As a subset-based technique, the accuracy of DIC relies heavily on the selection of the subset size. A larger subset size provides more accurate displacement analysis with sufficient gray intensity contrast. However, this results in a reduction of the spatial resolution and the underlying deformation in a smaller subset cannot be obtained. The conflicting demands for accuracy and precision of the technique imply that there is a pay-off between displacement/strain and spatial resolutions. To obtain accurate data at the crack tip with sufficient spatial resolution, it is necessary to work with high magnification images which loses the field of view.

2.6.3 Grid method

The grid method tracks the change of a periodical pattern bonded onto the specimen surface to characterise the surface deformation [95]. The periodical pattern is normally a grid film consisting of white and black cross lines. To derive the displacement field, the phase field which is linearly related to the displacement field is extracted from the changed grid pattern using phase shifting method. Generally, the technique has the displacement resolution lower than that of the interferometric methods. In previous studies the grid method has been applied to measure the displacement and strain fields around a crack in metals [96] and concretes [97]. However, as the grid film needs to be firmly bonded onto the specimen surface, the flexibility of both the composite face sheet and the foam core, especially at the debonded region, can be influenced.

2.6.4 Infrared imaging techniques

IR thermography or IR imaging measures the surface temperature of an object. The technique uses an IR detector to absorb thermal energy emitted by an object in the IR band and converts it into visible images. Heat released during fracture can be related to the temperature change around the crack tip, which makes the technique an attractive tool for the energy analysis associated with fracture. In previous studies energy caused by the plastic deformation during fracture in metallic materials was characterised using IR thermography [98, 99]. The results show that the crack tip plastic deformation can be characterised by the dissipated heat. In a recent study the technique was used to capture the heat dissipation of a brittle fracture in foam cored sandwich structures, which

indicates that a large amount of heat is dissipated by the break of brittle materials [25]. The recent development of high speed IR thermography [24] has shown the possibility to characterise the heat dissipation of a propagating crack before heat dissipates. This shows the potential to characterise the fracture energy by relating the dissipated thermal energy with the energy release at the crack tip.

TSA is another IR imaging technique. TSA is based on the thermoelastic effect where the strain induced temperature change on the surface of a component can be related quantitatively to the change in stresses. The temperature measurement for TSA is usually provided by a sensitive IR detector. TSA offers several advantages such as simple experimental setup, minimal specimen preparation and wide range of measurement sensitivities and resolutions. Modern IR detectors are capable of providing thermal resolutions less than 20 mK at room temperature. However, the technique assumes that the energy conversion is reversible and adiabatic. This assumption requires that the detected component must be cyclically loaded at a suitable rate to prevent heat transfer. Furthermore, the adiabatic condition is also dependent on the thermal conductivity of the material and the stress gradients in the specimen [23]. The technique has been demonstrated for characterising the near-tip plastic deformation and stress field for metallic materials [84]. In a recent study TSA also shows the capability to obtain meaningful stress data around the crack tip in PVC foams [100].

2.6.5 Summary

The above listed techniques are a brief summary of the full-field optical methods that have been applied for fracture mechanics. These techniques have been widely applied to metallic materials. Studies have shown that an improved understanding with regard to the fracture behaviour in metallic materials has been achieved, assisted by the development of optical measurement techniques. It is therefore desirable that a reliable optical method can be developed and employed to examine the interfacial fracture characteristics in foam cored sandwich composites.

A summary of the critical features for different optical methods is shown in Table 2.4. Techniques are compared in the following discussions by considering the influences of different features on the application to an interfacial crack in sandwich structures. Of the displacement based measurement techniques, the interferometric techniques can provide highest displacement and spatial resolutions. However, the interferometric techniques require stringent stability of the optical setup which limits the applicability to many situations. Furthermore, the techniques restrict the specimen motion between each load step usually to the order of micrometres to avoid phase unwrapping errors and speckle decorrelation [89]. This makes the technique very difficult to use for measuring

interfacial cracks in sandwich structures where large motions (usually in a scale of millimetres) can occur near the crack tip caused by the detached face sheet. The grid method which requires physical gratings applied on the specimen surface are not suitable for the current study. The bonded grating around the interfacial crack can cause a local change in the flexibility of the foam and composite materials and influence the crack opening and propagation behaviour. Considering the surface preparation and the relatively large motion around an interfacial crack, DIC is considered more suitable for the interfacial crack characterisation in sandwich structures.

The main disadvantage of DIC compared to the IR imaging techniques is its relatively low spatial resolutions. While high spatial resolutions can be obtained from DIC, a significant reduction of the measurement area is required. On the contrary, IR techniques perform the temperature analysis based on each pixel. As the development of modern IR detectors, IR techniques can provide very high spatial resolution with a sufficient field of view. Based on the use of TSA and IR thermography, both stress and energy related information can be obtained for the analysis of interfacial crack behaviour. The stress associated with high spatial resolutions shows the possibility to quantify any local effects/stress concentrations around a crack. It is for these reasons that the IR techniques are selected in this project for studying the interfacial fracture behaviour in foam cored sandwich structures.

Table 2.4: Comparison of the optical measurement techniques

Techniques	Sensitivity	Experimental setup	Spatial resolution	Surface preparation	Results
Speckle interferometry	10 nm	Complex	Laser wavelength	Rough surface	Displacement /strain
Moiré interferometry	0.1 μm	Complex	Laser wavelength	Grating	Displacement /strain
Grid method	1 μm	Simple	Grid pitch	Grating	Displacement /strain
DIC	1 μm	Simple	Subset	Speckle pattern	Displacement /strain
TSA	4 mK	Simple	Pixel	Black coating	Stress
IR thermography	4 mK (low frame rate)	Simple	Pixel	Black coating	Temperature/ heat

2.7 Summary

The need for developing suitable measurement techniques for characterising interfacial fracture in sandwich structures can be summarised as follows.

1. A review of the interfacial fracture toughness for sandwich structures shows that the mechanisms that cause differences in fracture toughness values and fracture behaviour are not well understood. Therefore, suitable measurement techniques which can provide more detailed information relating to the mechanisms that drive interfacial crack propagation in sandwich structures is required.

2. It is noted that analytical solutions for determining the interfacial fracture toughness are not validated for most of the test methods/specimens. A demand therefore exists for a measurement method that can be applied to different test methods/specimens and provides measurements suitable for comparison with FE models.

3. The understanding of the crack propagation behaviour at the tri-material junction of peel stoppers in sandwich structures is limited. To understand the fracture mechanism and further optimise the peel stopper design, a suitable measurement technique that can characterise the local effects at the tri-material junction is required. Thus, the influence of the local effects on the fracture behaviour can be understood and optimised.

To select a suitable measurement technique for characterising the interfacial fracture, a comparison of the full-field measurement techniques in terms of the applications of interfacial crack in sandwich structures is provided. Of the displacement based measurement techniques, DIC has been considered more suitable for the interfacial crack characterisation in sandwich structures as it can provide suitable displacement resolution and the application of the paint for the speckle pattern does not affect the material behaviour. However, it has been demonstrated that the spatial resolution provided by DIC is limited when compared to TSA. With the same field of view, TSA can provide higher spatial resolution than that of DIC. This is important for studying debond damage as fracture behaviour is affected by small features at the interface. Thus the use of TSA and high speed IR thermography in studies of interfacial cracks is explored in the present work.

Chapter 3

Infrared imaging techniques

3.1 Infrared thermography

It is known that electromagnetic radiation is emitted from the surface of any object at temperatures above absolute zero. The radiation is emitted across a wide spectral range, in which the IR portion refers to the radiation with wavelengths in the range from 770 nm to 1 mm [101]. Any object emits electromagnetic radiation proportional to its surface temperature. In 1900 Planck proposed the analytical equation which describes how the radiated energy varies as a function of both temperature and wavelength [102]. This can be written as:

$$R(\lambda, T) = \frac{2\pi s^2 h}{\lambda^5}\left(e^{\frac{sh}{\kappa\lambda T}} - 1\right)^{-1} \tag{3.1}$$

where R is the spectral radiant emittance, λ is the wavelength, T is the absolute temperature of the object, s is the speed of light, h is Planck's constant and κ is Boltzmann's constant. The above equation assumes that the radiation is emitted from an idealised source, for which all incident radiation, regardless of the angle of incidence, spectral composition and polarisation, is absorbed completely [102]. The idealised source is usually referred to as a 'blackbody'.

Planck's law is presented in Figure 3.1 in the form of isothermal curve (T constant). At room temperature, the maximum emitted energy is located in the IR spectrum, as shown in Figure 3.1. It is for this reason that IR radiation is commonly adopted for temperature measurement. The principle underlying IR thermography is therefore to transform the thermal energy which is emitted by objects in the IR band of the electromagnetic spectrum into a visible image.

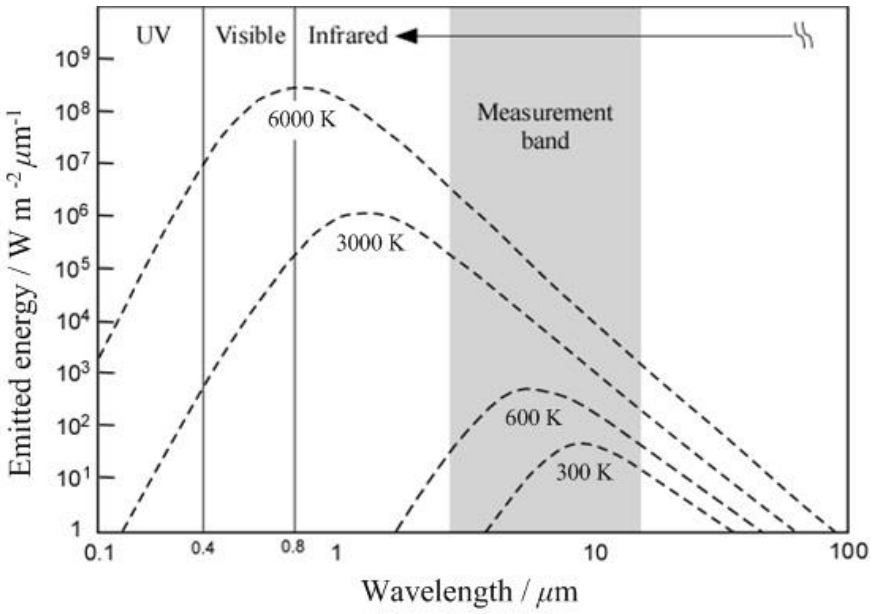

Figure 3.1: Emitted energy from a blackbody according to Planck's law

IR thermography relies on the use of an IR detector to absorb the IR emitted energy from an object. Modern IR detectors can be divided into two groups: thermal detectors and photon detectors. In a thermal detector the incident radiation is absorbed, changing the temperature of the detector [103]. The temperature change is then related to a change in another detector property (e.g. resistance) which provides the measurement output. Photon detectors absorb the radiation within a semiconductor material by interaction with the electrons; the changed electronic energy distribution leads to the observed electrical output signal [103]. Photon detectors require cryogenic cooling, resulting in increased complexity and cost, but offer better performance in terms of temperature sensitivity and response rate; they are therefore the preferred choice for performance driven applications such as TSA.

For a real object, incident radiation cannot be absorbed completely; some of the radiation is reflected and/or transmitted. Thermal equilibrium requires that the probability of a surface to emit radiation has to be equal to its absorption probability. This identity is known as Kirchhoff's law [104]. To describe the relationship between absorbed and reflected radiated energy, the concept of emissivity is introduced. The emissivity is defined in terms of the ratio between the radiated energy of a real object and a blackbody at the same temperature:

$$e(\lambda, T) = \frac{R(\lambda, T)}{R_{bb}(\lambda, T)} \tag{3.2}$$

where e is the emissivity and the subscript bb refers to the blackbody. In general all bodies in nature have different emissivities with values less than 1. The emissivity also varies depending on the material surface preparation. Typically, a rough surface has a higher emissivity than a polished surface. When IR emissions are used for temperature measurement it is therefore important to know the emissivity of the studied material. For high reflecting objects (i.e. low emissivity) such as most metals, the radiation coming from the surfaces contains a high amount of reflected light from the surrounding environment. This makes temperature measurement difficult. A common way to overcome the problem is to apply a thin coating with high emissivity (e.g. a matt black coating) on the material surface. The application of a thin coating also helps to ensure a uniform surface emissivity.

3.2 Thermoelastic stress analysis

3.2.1 TSA theory

The thermoelastic effect [105] refers to the change in temperature that occurs when a material is subject to a change in the elastic strain. Since the first theoretical treatment of the thermoelastic effect established by Thomson (Lord Kelvin) in 1853, simplified forms of the thermoelastic equations for both isotropic and orthotropic materials have been developed. The simplified equations rely on the assumption of adiabatic conditions (i.e. the energy conversion between mechanical deformation and thermal energy is reversible). In practice, the adiabatic condition is achieved by cyclically loading the material at a rate such that virtually no heat conduction occurs during a loading cycle. Under adiabatic conditions, the relationship between the stress change and the corresponding change in temperature for an isotropic material can be written as [106]:

$$\Delta T = -\frac{\alpha T}{\rho C_p}\Delta(\sigma_1 + \sigma_2) \tag{3.3}$$

where ρ is the material density, α is the coefficient of linear thermal expansion, C_p is the specific heat at constant pressure and $\Delta(\sigma_1 + \sigma_2)$ is the change in the sum of the principal stresses. Equation (3.3) shows that the temperature change, ΔT, is proportional to the change in stresses. The thermoelastic constant, K_T, is a material property that defines this proportionality and it is usually defined as:

$$K_T = \frac{\alpha}{\rho C_p} \tag{3.4}$$

In the case of a homogeneous orthotropic material, equation (3.3) has to be presented in the form as [106]:

$$\Delta T = -\frac{T}{\rho C_p}\Delta(\alpha_1\sigma_1 + \alpha_2\sigma_2) \tag{3.5}$$

where α_1 and α_2 are the coefficients of thermal expansion in the principal material directions.

Equations (3.3) and (3.5) provide the theoretical basis for TSA. However, heat diffusion is inevitable in practice which results in non-adiabatic effects influencing the TSA. In general, the non-adiabatic behaviour becomes significant where there are large stress gradients (leading to 'large' instantaneous temperature gradients within the loading cycle) and for materials with a high conductivity. A more complete formulation of the thermoelastic relationship for an isotropic material that considers the non-adiabatic behaviour can be described as [107]:

$$\frac{\partial T}{\partial t} = -\frac{1}{\rho C_p}\left(\alpha T\frac{\partial(\sigma_1 + \sigma_2)}{\partial t} - \varsigma\nabla^2 T\right) \tag{3.6}$$

where t is time and ς is the conductivity of the material. Two different terms in the brackets are given in equation (3.6). The first term, $\frac{\partial(\sigma_1+\sigma_2)}{\partial t}$, corresponds to the adiabatic temperature change due to the change in stress. The second term, $\varsigma\nabla^2 T$, describes the spatial heat transfer due to a temperature gradient. It is clear that adiabatic conditions can only be achieved when the thermal conductivity is zero ($\varsigma = 0$) or no temperature gradient exists ($\nabla^2 T = 0$). In a real material the thermal conductivity can never be zero. The thermal conductivity can be high in metallic materials such as aluminium alloys while in some materials, for example FRP and PVC foam, ς is very small. On the other hand, $\nabla^2 T$ can equal zero only under certain load conditions (e.g. uniaxial tension) with a homogeneous material, in which the adiabatic temperature change is distributed uniformly across the whole material without temperature gradients. However, in experimental work, the loading conditions and the materials under study are normally complex and in order to achieve nearly adiabatic conditions, it is common to increase the loading frequency (the time scale, ∂t, is made small) so that the first term becomes large in comparison with the heat transfer term.

3.2.2 Measurement system

The application of IR thermography for TSA was first demonstrated by Belgen in 1967 [108]. Since then, two types of systems (single detector scanning systems and focal plane array detector systems) have been developed from which the small change in temperature for TSA can be measured.

The first commercially available system for TSA was the SPATE (Stress Pattern Analysis by Thermal Emissions), which is a single detector scanning system. The detector unit comprises a motor-driven mirror system that allows the detector to scan the entire region of interest in a point by point raster mode. Due to the small temperature changes generated by the thermoelastic effect (a resolution of a few mK is generally required to measure stresses with a useful resolution [109]), a lock-in amplifier was employed in the SPATE system to filter out the signal noise. In the lock-in procedure, a reference signal (often the load cell signal) is used to provide a band pass filter. The IR signal is then filtered, relying on the reference signal to extract only the temperature changes at the reference frequency (i.e. the loading frequency). Through the use of a reference signal, a phase angle between the load and the temperature changes can be obtained. The phase angle will be uniform across the specimen under ideal adiabatic conditions with only a 180° phase shift between regions of tensile and compressive stress. Under non-adiabatic conditions, a shift in the phase angle of the thermoelastic signal relative to the loading reference will occur. Local deviations in the phase angle can therefore be used to identify non-adiabatic behaviour for TSA. The lock-in procedure has become general practice in almost all TSA systems to date.

Single detector scanning systems such as the SPATE have now been replaced by focal plane array detectors, capable of obtaining snapshot images. This reduces the data acquisition time from hours to seconds, thereby providing means to measure real-time fatigue damage accumulation and crack growth. In essence the systems perform the same thermoelastic signal processing as the SPATE system, but using digital instead of analogue processing. The main features of the system used in this work are described in section 3.3.

3.2.3 Stress calibration

When the component under examination contains only a single material, the thermoelastic temperature change, ΔT (as defined in equations (3.3) or (3.5)) can be used directly to describe the corresponding stress change in a component. However, since the temperature, T, may not be uniformly distributed over the surface of the component due to ambient temperature fluctuations or heating at a damage site, the non-dimensional stress metric, $\Delta T/T$, is commonly used to present the stress change in TSA. However, when a component contains two or more materials (e.g. in a sandwich structure), it is necessary to obtain the thermoelastic constant for each material, i.e. calibrate the $\Delta T/T$ value into units of stress, to enable a comparison of the stresses in different materials. This process is referred to as “stress calibration”. Stress calibration is also required when comparing the TSA results with analytical or numerical analyses. Two commonly used methods for the stress calibration are:

1. direct calibration based on equation (3.4) with known material properties,

2. calibration based on a calculated stress and measured value of $\Delta T/T$.

The first method requires material properties (density, coefficient of thermal expansion and the specific heat) to be determined individually from other measurement techniques. The method is not regarded as very accurate as errors in each of the material properties are combined in the calculation and can lead to significant total errors [110]. The second method is a more common approach for stress calibration in TSA. It has been used for the stress calibration in both composite materials [111] and foam cored sandwich structures [112]. The method requires no knowledge about the material properties. Instead, a representative calibration specimen with a known stress field is required. For isotropic materials, the thermoelastic constant can be derived based on equation (3.3) using a simple uniaxial test specimen. In the case of orthotropic materials the orientation of the test specimen is important and stress calibration should be applied for each principal material direction. In the work described in this thesis the second method is used to obtain the thermoelastic constant for different constituent materials in sandwich structures. A detailed description of the stress calibration is provided in Chapter 5.

3.2.4 Sample motion problem

The challenge of addressing test specimen motion arises whenever a change in stress is required to effect a measurement made using an imaging system. Since the stress change always involves a deformation, and the imaging system is typically stationary, the component will move relative to the image, as shown in Figure 3.2 for the example of an arbitrary sample undergoing sinusoidal loading. The change in temperature at the top right corner of the specimen (Pixel 1 in Figure 3.2) between the top and bottom of the load cycle is $T_2 - T_1$. However, since the analysis is conducted on a pixel by pixel basis, the detector will output $T_3 - T_1$. Specimen motion is considered significant when large stress gradients are of interest and when motion exceeds 1 image pixel, although the effect can be observed for displacements smaller than 1 image pixel at specimen edges.

The primary need for motion compensation (MC) in the current work results from the initial interfacial crack introduced in the sandwich specimen, which causes a large and complex motion around the crack tip under dynamic loading. This motion generates spurious measurements that mask the actual thermoelastic response especially at the foam and the face sheet edges.

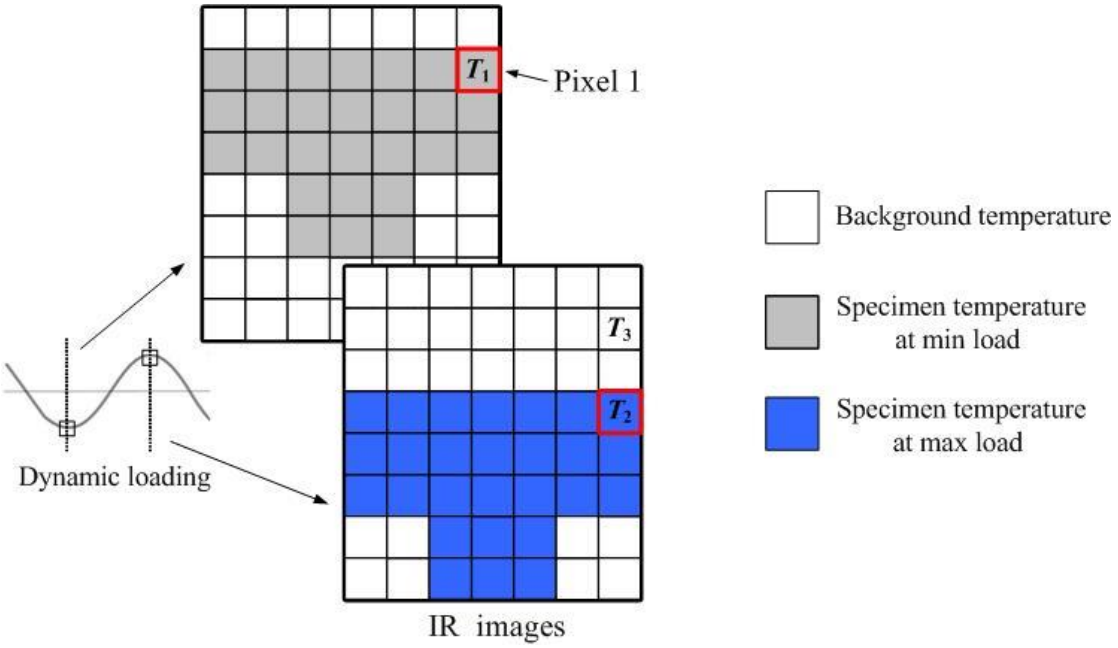

Figure 3.2: Sample motion observed in IR images during dynamic loading

One method to deal with the sample motion problem was reported in [113] which is essentially based on pattern recognition and requires two operations. The first step termed "vector tracking" is to identify two strong contrast points on the specimen surface in the first thermal image of a recorded video data, and draw a vector between them. The points can be small surface defects or marks with low emissivity attached on the specimen. The points with strong contrast can be searched and located in all subsequent thermal images and the corresponding vector is then relocated in each frame according to the new position of the points. The second step then calculates the motion (displacement, rotation and elongation) of the vector from frame to frame, and distorts each image accordingly so that the specimen becomes stationary in the thermal images. One major shortcoming of this method is that the analysis assumes a uniform and continuous motion field. When the method is used to correct the motion around an interfacial crack, the vector is unable to characterise the non-uniform and discontinuous displacement field between the detached face sheets and the core.

The use of digital image correlation (DIC) to correct for specimen motion in TSA has been proposed in two recent studies by Sakagami *et al.* [114] and Silva and Ravichandaran [115]. In both publications, a single IR detector was used to obtain the data for both the TSA analysis and the DIC based motion correction. The use of an IR detector for DIC requires the specimen to be painted using paints with different emissivity values in the IR spectrum to form a speckle pattern. However, the varying emissivity that gives the speckle in the IR spectrum also influences the assessment of the

surface temperature for TSA. To circumvent the effect of the speckle pattern to TSA, in [114] the specimen motion was obtained in a first set of measurement for DIC. Then the speckle was removed and a second data set was collected for TSA. This process is cumbersome, especially for rough surfaces such as foams, and does not lend itself to applications where the motion field may change as a defect (such as an interfacial crack) is grown over a series of fatigue steps. In reference [115] both the DIC and TSA were performed on the same IR images. The gaps in the data arising from the speckles were filled by interpolating across the speckles. This requires the speckles to be relatively sparsely distributed, and lowers the spatial resolution of the displacement field obtained by DIC. The use of a single IR detector to capture both images for DIC and TSA brings the benefit that the images collected possess the same pixel resolutions and no spatial alignment is required. However, images obtained from current IR detectors can provide only limited spatial resolutions, typically no more than 640 × 512 pixels in one image and significantly reduce the resolution of the displacement field obtained by the DIC. This does not pose a problem when the motion is relatively uniform across the surface of the specimen. However, when large displacement gradients and discontinuities exist within the field of view, as in the case of a face sheet debonding from a sandwich structure, this low spatial resolution will prohibit the details of the motion field to be captured, thereby resulting in a decrease in accuracy of the DIC.

It has been shown from the above descriptions that the current MC methods for TSA are not suited to correct the motion of an interfacial crack in sandwich structures. Therefore, a new MC method which is able to correct the discontinuous motion field is necessary for the current study.

3.3 FLIR infrared system

3.3.1 Main features of the system

The IR system used in this work was supplied by FLIR (formerly Cedip Infrared Systems at the time of purchase). The camera system belongs to the FLIR SC5500 series. The system includes a photon detector, sensitive to radiation with wavelengths from 3 to 5 μm. The detector comprises a 320 × 256 element indium/antimonide (InSb) detector array, cooled by an internal Stirling pump to 77K. Each detector element absorbs the radiation within the semiconductor material (InSb) by interaction with electrons, and the changed electronic energy on the detector array is presented by a 14 bit digital level (DL) bitmap using an on-board analogue to digital converter. The system is able to output the raw

thermal images with minimal on-board processing enabling the data to be processed in a variety of ways by the user.

In standard operation the detector has a sensitivity of 4.2 mK at 25 °C with an electronic noise of 15.75 mK. The detector provides a maximum frame rate of 383 Hz at full frame. Compared to previous TSA systems, which used a calibration constant relating the amplitude of the detector response to the stress change, this system was radiometrically calibrated by the manufacturer so that the detector DL output can be directly converted to temperature. The temperature calibration process is described in the next section.

The IR detector is focused on the object under study using a variety of lenses. The lens type and the detector stand-off distance determine the field of view (FOV) and the spatial resolution. Three sets of lenses are available for the current IR system. An inbuilt 27 mm lens allows objects to be studied from a range of distances from approximately 150 mm to infinity. The minimum FOV of the 27 mm lens is about 54.4 × 43.5 mm^2, which gives a minimum pixel resolution around 0. 17 mm. For investigating local effects with high spatial resolution, two magnifying lenses, known as the G1 lens and the G0.5 lens, are available. These lenses are designed to work together with the inbuilt 27 mm optics; they slot into the camera housing in front of the 27 mm lens. The use of the G1 lens increases the pixel resolution to 0.03 mm and the FOV is decreased to an area of 9.6 × 7.7 mm^2. The G0.5 lens is an intermediate lens which provides FOV of 19.2 × 15.4 mm^2 and a corresponding pixel resolution of 0.06 mm. The selection of a suitable IR lens depends on both the area of interest on the structure and the required spatial resolution. In this work all three lenses are used for different purposes and the selection of the lens is specified for each application.

One important feature offered by the current IR detector is that the thermal images can be recorded at increased frame rates by subwindowing (i.e. using only a subset of the full array). However, the obtained maximum frame rate is limited by the integration time (exposure time) and the detector data handling capacity. At increased frame rate, the reduced integration time decreases the emittance available for measurement which lowers the thermal sensitivity. Meanwhile, the limited data handling capacity requires a reduction of the window size and a corresponding decrease of the field of view. Thus, the faster the data capture the lower the thermal sensitivity and the spatial resolution. Figure 3.3 illustrates how the integration time and the window size changes with the frame rate for the current system [24]. It is shown that a practical limit of the maximum frame rate is around 16 kHz above which the sensitivity and the image window size become impractical.

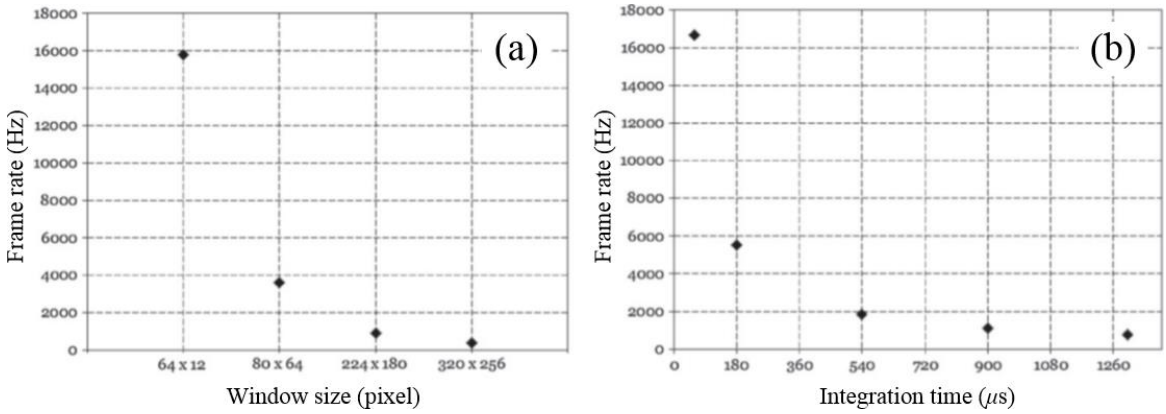

Figure 3.3: Relationship between (a) window size and frame rate and (b) integration time and frame rate [24]

This IR system also includes other important features which are used in this work. For instance, the external trigger function allows data collection to be initiated by an external event. In addition, the detector can also be operated in a pre-trigger mode. This enables data to be acquired, for example, specimen failure, by triggering the recording after the event.

3.3.2 Temperature calibration at high frame rates

Temperature calibration is required for the IR system to provide a direct link between the temperature and the detector DL output. As the calibration data provided by the manufacturer only covers a finite range of combinations of integration time, window size and frame rate, the operation of the IR detector outside of these parameter combinations (for example at frame rates of several kHz combined with temperature measurements around 300 K) requires a new calibration procedure to be performed.

The calibration is usually done by exposing the detector in front of a blackbody over a range of controlled temperatures. The calibration is then performed using the average DL value from the detector array. Since each detector element possesses its own behaviour, the response of each element must be corrected relative to the mean response of the detector array. This step is called the non-uniformity correction (NUC). The standard NUC is based on the linear relationship between the detector digital output and the incident radiation. The NUC procedure is to present all detector elements with a uniform high emissivity source at two different temperatures. As the response of each detector element is linear, the two data points captured for each element enable to element response to be defined by two parameters, a gain and an offset. Thus the variation in response of each detector element relative to the mean response of the detector can be corrected. Subsequent conversion into units of temperature can then be performed using

the single calibration curve obtained for the detector. This is the standard calibration process applied to all data within the standard operating range of the detector.

At high frame rates, the necessary integration time is very small (e.g. 60 μs at 15 kHz) which significantly decreases the photon emittance available for measurement and results in a very low detector DL output for room temperature measurements. At these very low photon counts, the linear response of the detector cannot be assumed, and therefore the standard NUC procedure is unsuited to calibrate for high speed IR thermography. A calibration approach that accounts for the detector nonlinear response has been recently developed by Fruehmann *et al*. [24]. The approach performs a calibration for each detector element individually across the array, thereby addressing the problems of image non-uniformity and detector nonlinearity in a single step. In [24] the calibration process has been experimentally examined at the frame rate of 15 kHz. An assessment of the measurement precision at 15 kHz frame rate was provided in [24] and is listed in Table 3.1. The sensitivity represents the temperature increment per DL and the precision is the detector noise calibrated into °C (the noise quoted is the mean over the full array of the standard derivation from 20 readings at identical temperature for an individual detector element). In this work, the high speed IR thermography is used to monitor the crack front temperature during the interfacial fracture and to characterise the fracture energy in sandwich structures.

Table 3.1: Detector precision at 15 kHz frame rate [24]

Temperature (°C)	Sensitivity (°C/DL)	Precision (°C)
15	0.14	0.32
20	0.11	0.27
35	0.08	0.19
45	0.06	0.14

3.4 Digital image correlation

As has been described in section 3.2.4, a new MC method is required for correcting the discontinuous motion field of an interfacial crack for TSA. For this purpose, a high spatial resolution MC method based on DIC is developed in this work and is described in Chapter 4. Comparing to other displacement measurement techniques (as reviewed in section 2.6), DIC is selected in this work as it requires simple surface treatment and provides a suitable displacement resolution with a convenient test setup. This section

provides a general review of the DIC technique and an introduction of the DIC system used in this work.

3.4.1 Digital image correlation algorithm

In DIC the specimen deformation is calculated by tracking speckle patterns between different images of the specimen as it deforms using a correlation algorithm. DIC essentially tracks the same point between the images, however, since an individual point cannot provide enough information to enable reliable identification of the same point in different images, image correlation is therefore performed using the variation in grey scale levels of a group of points referred to as the subset. In this section the image correlation algorithm is reviewed for 2D-DIC deformation measurement. The correlation for 3D-DIC is the same except that the out-of-plane deformation is also considered.

Figure 3.4 illustrates the image correlation conducted on one typical subset used to compute the displacements in the x and y directions of the central point P. As point P in the reference subset moves to P' in the deformed subset, the assumption of deformation continuity is made which means the neighbouring points of P in the reference subset remain the same around P'. Thus, the location of a point such as point Q in the reference subset can be mapped to the point Q' in the deformed subset according to the shape functions as follows [91]:

$$\begin{aligned} x_{\mathrm{i}}^{'} &= x_{\mathrm{i}} + \xi\,(x, y) \\ y_{\mathrm{i}}^{'} &= y_{\mathrm{i}} + \eta\,(x, y) \end{aligned} \tag{3.7}$$

where $\xi\,(x, y)$ and $\eta\,(x, y)$ are the shape functions. If only considering the pure translation in a rigid body, the displacements of all points in the subset are the same and can be described using a zero-order shape function:

$$\begin{aligned} \xi\,(x, y) &= u \\ \eta\,(x, y) &= v \end{aligned} \tag{3.8}$$

where u and v are displacement vectors in the x and y directions respectively. The first-order shape function which allows translation, rotation and shear of the subset to be considered can be described as:

$$\begin{aligned} \xi\,(x, y) &= u + \frac{\partial u}{\partial x}dx + \frac{\partial u}{\partial y}dy \\ \eta\,(x, y) &= v + \frac{\partial v}{\partial x}dx + \frac{\partial v}{\partial y}dy \end{aligned} \tag{3.9}$$

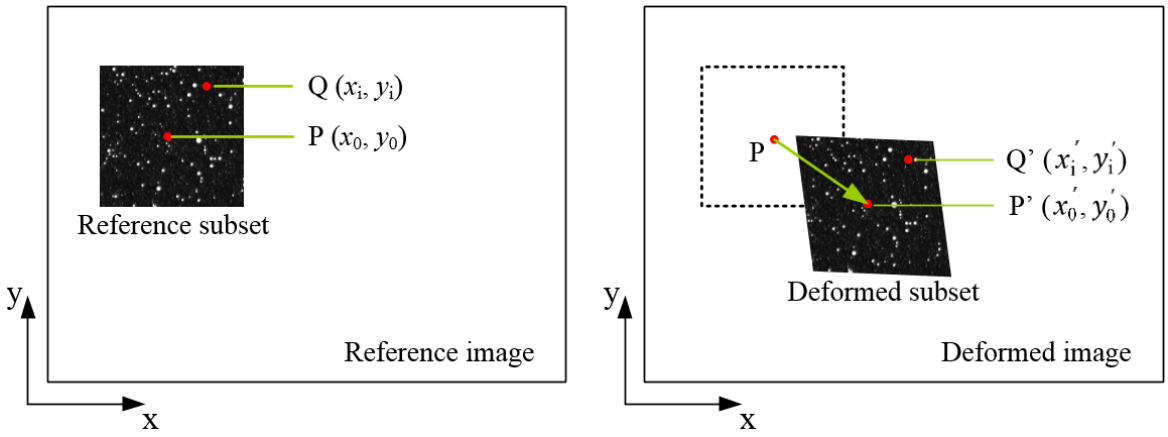

Figure 3.4: Schematic of image correlation

In equations (3.8) and (3.9) u and v are the displacement vectors of point P and $\partial u/\partial x$, $\partial u/\partial y$, $\partial v/\partial x$ and $\partial v/\partial y$ are the first-order displacement gradients. It is clear that the zero-order shape function considers no shape deformation of the subset, and the first-order shape function assumes the deformations inside a subset are linear. If more complex deformation occurs inside the subset, second-order or high-order shape functions can be employed [91], but image correlation with high-order shape functions consumes much more computing time than that with the zero- and first-order shape functions.

To evaluate the similarity of the speckle pattern between the reference subset and the deformed subset, the correlation criterion must be defined. Two commonly adopted correlation criteria include cross-correlation (CC) and sum-squared different (SSD). These are described as follows [91]:

$$C_{CC} = \sum_{i=-N}^{N}\sum_{j=-N}^{N}[f(x_i, y_i)g(x_i', y_i')]$$
$$C_{SSD} = \sum_{i=-N}^{N}\sum_{j=-N}^{N}[f(x_i, y_i) - g(x_i', y_i')]^2 \quad (3.10)$$

Where N is the size of the subset (i.e. number of pixels in the x and y directions), $f(x_i, y_i)$ is the intensity/grey scale value in the reference subset and $g(x_i', y_i')$ is the intensity value in the deformed subset. The location of the deformed subset is determined by searching for the correlation coefficient extremum (a maximum value of C_{CC} or a minimum value of C_{SSD}) and the displacement (u, v) of point P can be obtained according to the differences in the positions of the reference subset centre and the deformed subset centre. The search scheme can be implemented in the spatial domain by searching for point P', pixel by pixel, in a specified region. Alternatively, the search routine can also be

employed in the frequency domain. In the frequency domain, the correlation between two subsets can be obtained as the complex multiplication of the reference subset frequency spectrum by the frequency spectrum of the deformed subset using a fast Fourier transform (FFT). As the methods described above can only provide 1 pixel displacement resolution, several sub-pixel intensity interpolations are commonly adopted, and sub-pixel displacements can be obtained by different algorithms such as coarse-fine searching, peak-finding and Newtown-Raphson iteration [91]. With these sub-pixel routines, the displacement resolution can be improved to 0.01-0.05 pixels.

3.4.2 LA vision DIC system

The DIC system used in this work is the commercial LaVision DIC System. The system includes two CCD (charge coupled device) cameras and the image correlation software. The CCD camera is the 'LaVision VC-Imager E-lite 5M' with a resolution of 2400 × 2400 pixels and 12 bit grey scale range. This system is able to perform both 2D and 3D DIC measurements by using one single camera (2D-DIC) or two cameras (3D-DIC). In 2D-DIC it is important that the imaging plane is parallel to the specimen deformation plane to avoid measurement errors resulting from differences in magnification across the field of view. In general, the effect is small for small misalignment angles; Meng *et al*. [116] concluded that a misalignment of 5° resulted in a displacement error smaller than 0.01 pixels. To enable the obtained displacements to be converted from pixels to length units, the DIC system requires a calibration for the camera setup. For 2D-DIC, the calibration can be conducted by simply defining the distance between two points on an image, e.g. using a known specimen dimension.

The image correlation is performed by the DaVis 8.1.3 software. The software performs the image correlation in the frequency domain using the SSD criterion and the first-order shape function. The sub-pixel displacements are derived using the peak-finding algorithm. The software provides a wide range of subset size with an overlap from 0% to 99%. As shown in Figure 3.5 (a) and (b), images with two different subsets are illustrated. Each square represents one subset and the arrows show the displacement of each subset. It is clear that the image with larger subset size contains more pixels with accordingly more variation in grey levels, and hence improved accuracy in the image correlation. However, the large subset size offers low spatial resolution. As the example shown in Figure 3.5, the image correlation by 64 × 64 pixel subset provides a 4 times lower spatial resolution compared to that of the 32 × 32 pixel subset. Therefore, the selection of a suitable subset size is extremely important for DIC. A proper subset should contain the minimum number of pixels that provide adequate displacement resolution for the expected displacements. A compromise can be achieved by allowing adjacent subsets to overlap, thereby increasing the apparent density of displacement points obtained while maintaining the same

displacement precision, as shown in Figure 3.5 (c) where the 64 × 64 pixel subset with 50% overlap is used. It is worth noting at this point that adjacent subsets share grey level content and that the true increase in spatial resolution is not a simple function of the density of the displacement points. More detailed discussion on this issue can be found in [117].

For images with an optimum intensity contrast and speckle pattern, the expected displacement accuracy obtained from the LaVision system is listed in Table 3.2 [118]. The displacement accuracy in mm can be obtained by the value of pixel/mm determined by the setup of the camera and lens. In practice, the displacement accuracy obtained via the DIC is influenced by the quality of the captured images. The speckle pattern (size, density and distribution), intensity contrast and lighting are important factors that influence the accuracy of the correlation. For example, very large speckles and over illuminated speckles within a subset reduce the uniqueness of the subset which in turn increases the chance of a poor or even false correlation. Also, higher image contrast that utilises the full dynamic range of the detector (but without saturation) provides more precise displacement measurement. This is achieved by using suitably high contrast paints for the speckle and the background, appropriate illumination of the specimen surface and ensuring that the lighting is uniform across the entire image.

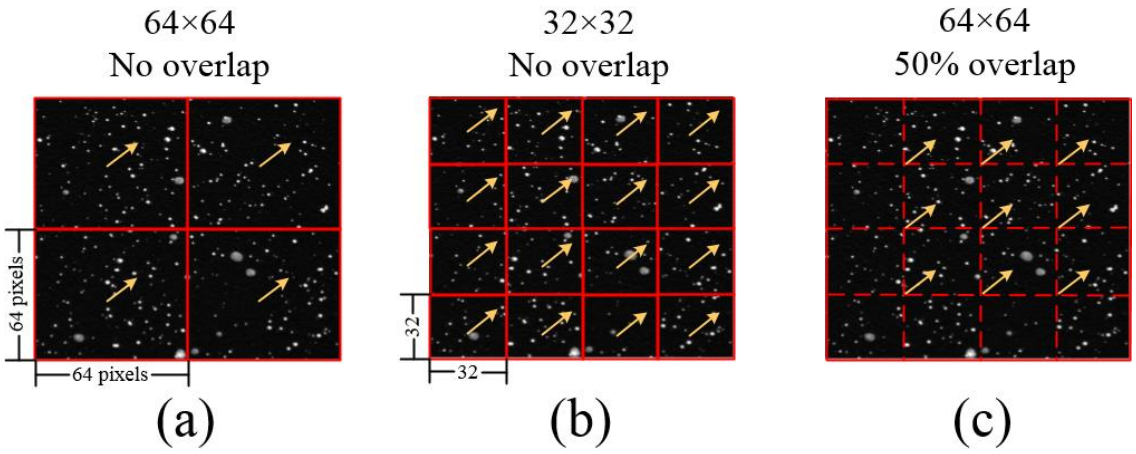

Figure 3.5: Image with different subset sizes and overlap

Table 3.2: Displacement accuracy of DaVis 8.1.3 [118]

Subset size (pixel)	Displacement accuracy
16 × 16	0.05 pixel
32 × 32	0.025 pixel
64 × 64	0.01 pixel
128 × 128	0.005 pixel

3.5 Summary

In Chapter 2 TSA and IR thermography have been identified as two attractive candidates for characterising the interfacial fracture behaviour in sandwich structures. TSA is capable of establishing the stress state around an interfacial crack with high spatial resolution. The high speed IR thermography shows the potential to characterise the fracture toughness by relating the measured thermal energy with the fracture energy required for crack propagation. Challenges associated with the characterisation of the interfacial fracture behaviour using these techniques can be summarised as follows.

1. To date TSA has not been used to study interfacial cracks in sandwich structures. A major consideration which impedes an accurate thermoelastic response is the discontinuous motion around the crack tip caused by the detachment between the face sheet and the core. This requires the development of a new MC method, capable of eliminating the effect of such a complex motion field.

2. The use of high speed IR thermography provides the possibility of capturing the dissipated heat during fracture. However, no experiments have been conducted in the past to capture the dissipated heat at the crack front using high speed IR thermography. New calibration approaches for high speed IR thermography now provide an opportunity to explore this avenue. This will require a suitable test setup for obtaining a reliable and accurate measurement to be developed.

In summary, the work described in this thesis aims to develop TSA and high speed IR thermography as two reliable measurement techniques to enable the study of the interfacial fracture behaviour in foam cored sandwich composites. The focus is to address the challenges of using the techniques to establish the accurate measurement at the crack tip. A new MC method for TSA is described in Chapter 4 and an experimental validation of the methodology is provided. Chapter 5 applies the MC method to correct the complex motion at the crack tip of the DCB sandwich specimen. The stress fields before and after MC are compared. The aim is to show that TSA, together with the new MC method, can provide quantitative information regarding the stress fields in foam cored sandwich composites, with high spatial resolution. Chapter 6 investigates the feasibility of using high speed IR thermography to capture the heat generated at the crack front at the time of fracture. An experimental method is proposed to relate the heat generated at the crack front to the fracture toughness at the face sheet/core interface in foam cored composite sandwich structures. Chapters 7 and 8 study the efficiency of the peel stopper under mode I dominated loading. TSA with the MC method is used to investigate the local effects

introduced by the peel stopper when a crack approaches and to understand how these local effects influence the crack path at the tri-material junction.

Chapter 4

A high spatial resolution motion compensation method for TSA

4.1 Introduction

It has been demonstrated in Chapter 3 that a new MC method is indispensable to TSA for establishing the accurate stress field at the crack tip in a debonded sandwich structure. To compensate for the specimen motion in the TSA data, a full-field displacement map across the face sheet/core interface has to be obtained. A discussion of the different surface deformation measurement techniques have been provided in Chapter 2. It was shown that DIC is most suited to measure the displacements at the debond tip for three reasons: 1) the application of the paint for the speckle pattern for DIC does not affect the material behaviour, 2) the test setup for DIC is reliable and convenient, and 3) DIC provides suitable displacement resolution for assessing the deformation of the test specimen. In Chapter 3 the MC methods that use DIC to correct specimen motion for TSA has been reviewed. However, the methods that use an IR detector to capture images for DIC provide only limited image spatial resolution. The low spatial resolution does not allow the details of the discontinuous motion at the face sheet/core interface to be captured adequately, thereby resulting in a decrease in accuracy of the DIC.

The development of a high spatial resolution MC method for TSA is described. The focus is to establish a methodology that uses a high resolution white light sensor to capture images that enable the specimen displacement to be determined by DIC and apply a motion correction of the thermal images. To begin with, a description of the test arrangements and the data processing approach for the MC method is provided. The

method is then tested using a uniform matt black paint coating for the TSA, and subsequently applying a speckle pattern on top of the black coating for the DIC. For validation, the results with and without MC are compared with FE model results. Finally, a second set of tests is performed to assess the feasibility of capturing the images for TSA and DIC simultaneously, i.e. using the same surface preparation for both the TSA and the DIC, thereby allowing the MC method to be applied under fatigue loading. TSA is performed on the same specimen, but without removing the speckle pattern, and the results are validated against the TSA results obtained from the black matt coating.

4.2 High spatial resolution motion compensation method

The idea behind the high spatial resolution MC method is to use DIC to track the specimen displacement under the same loading conditions as used for the TSA and incorporate the displacement field for motion correction of the thermal images. The CCD camera (LA Vision VC-Imager E-lite) used for DIC provides a spatial resolution of 2400 × 2400 pixels which is much higher than that of the IR camera (typically 320 × 256 pixels in one image). Thus, images with high spatial resolution can be captured for DIC.

4.2.1 Test arrangements

The MC method captures the images for TSA and DIC as follows:

1. The specimen is coated with matt black paint to increase and homogenise the surface emissivity.
2. As images are acquired by two separate camera systems, for alignment purposes it is necessary to apply position marks on the specimen, which have strong contrast in both the IR and white light spectra.
3. The specimen is mounted into a test machine capable of cyclic loading.
4. The temperature time history is obtained by the IR detector during cyclic loading so that it can be used in the TSA.
5. Without removing the specimen from the machine, a random white speckle pattern is applied on top of the matt black coating for DIC.
6. White light images are captured at a rate of 1 Hz as the specimen is loaded *quasi* statically at rate of 1mm/min over a range equivalent to dynamic loading range used in step 4.

The use of the two camera systems requires the white light and thermal images collected from the specimen surface to be aligned as the cameras may rotate (both in-plane and out-of-plane) relative to the specimen surface. To facilitate alignment of the thermal images and the DIC displacement map, a specimen edge is used to provide a datum for in-plane rotation alignment as shown in Figure 4.1. When a magnifying lens is used, the edge of the position marks is used for the same purpose. To minimise out-of-plane misalignment (i.e. to ensure that the imaging plane is parallel to the specimen surface) a spirit level is placed perpendicular to the specimen surface pointing towards the camera, and the camera position is adjusted to be perpendicular with the spirit level.

4.2.2 Data processing

The displacement of the specimen is derived from the white light images using the DaVis software. To incorporate the displacement field for motion correction of the IR images, it is necessary to interpolate the displacement vector fields to fit to the IR data as the sensor arrays of the cameras are different and hence the spatial resolution of the IR and the displacement data are different. To make the data sets comparable, a linear interpolation procedure is applied to the displacement field. Figure 4.2 shows the interpolation process for deriving the displacement of one pixel in the IR data. The global image datum origin is at the top left corner of the white light image. The lower right corner of each pixel in the IR image is used as the reference datum for the interpolation. As the IR and white light images have been aligned by the position marks, the location of the IR datum in the displacement field can be determined according to the distance between the IR datum and position marks. The interpolation of the displacement field is performed using a bilinear interpolation. By referring to Figure 4.2 the displacement in the x-direction along the top and bottom of the cell relative to the IR datum is established as follows:

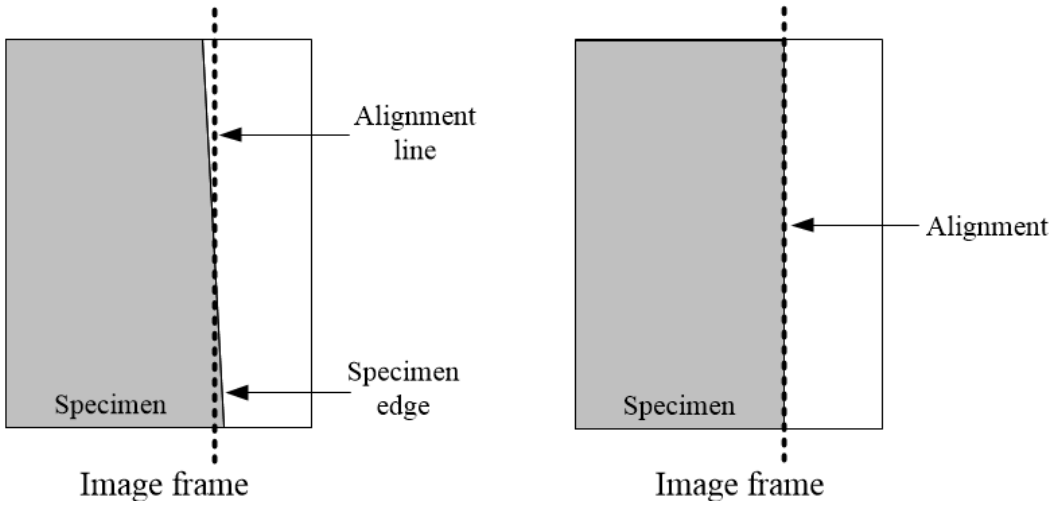

Figure 4.1: Specimen in-plane rotation alignment

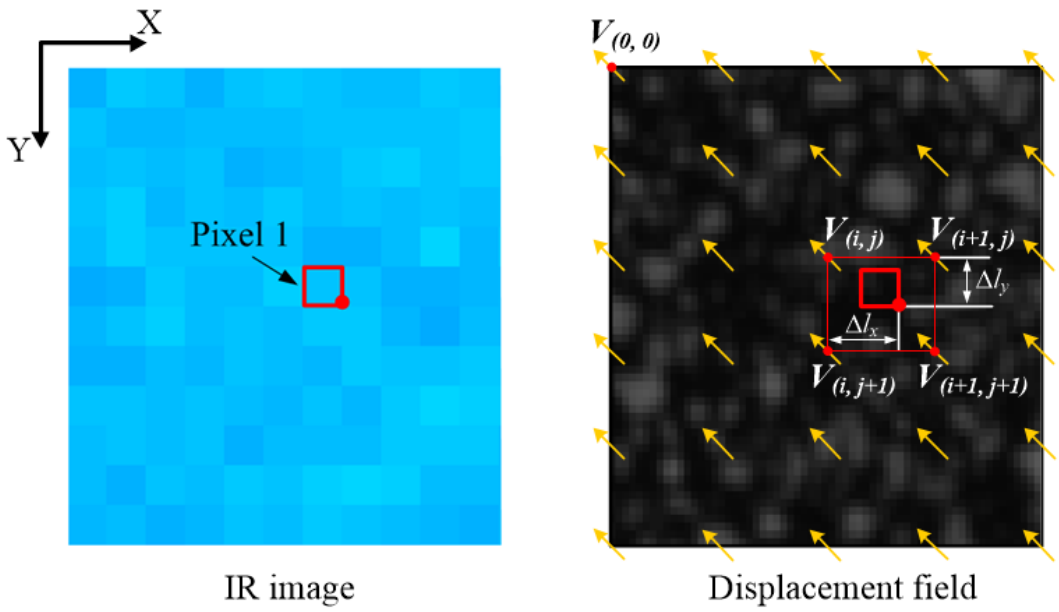

Figure 4.2: A typical thermal image and its corresponding displacement

$$D_{i+\Delta l_x, j} = \frac{d - \Delta l_x}{d} V_{i,j} + \frac{\Delta l_x}{d} V_{i+1,j}$$
$$D_{i+\Delta l_x, j+1} = \frac{d - \Delta l_x}{d} V_{i,j+1} + \frac{\Delta l_x}{d} V_{i+1,j+1} \quad (4.1)$$

where $V_{i,j}$ represents the displacement value at the mid-point of the DIC subset (i,j), Δl_x is the horizontal (x-direction) distance between an adjacent point on the displacement grid and the IR pixel datum and d is the spatial resolution of the displacement field, ($d = N \times S$, where N is the subset size and S is the percentage of the overlap). The displacements given by equation (4.1) are then interpolated in the vertical (y-direction) to provide the displacement vector at the IR datum as follows:

$$D_{i+\Delta l_x, j+\Delta l_y} = \frac{d - \Delta l_y}{d} D_{i+\Delta l_x, j} + \frac{\Delta l_y}{d} D_{i+\Delta l_x, j+1} \quad (4.2)$$

Equation (4.2) gives the displacement value of a single pixel in the IR image. By locating each pixel in the displacement field, the displacement vector of each pixel in the IR image can be obtained.

The images for the DIC are captured during *quasi* static loading over a range equivalent to that of the cyclic load in the IR data capture. This gives the displacements at the extremes of the load cycle. However, the IR data are sampled at many points throughout the loading cycle. Hence, the image displacement correction needs to be interpolated

between the maxima and minima depending on the time of IR image capture within the loading cycle. For this it is assumed that the load-displacement relationship is linear. The displacement at each frame can then be calculated as a proportion of the maximum displacement for each pixel in the IR image. The position of an IR image in the loading cycle is obtained from the load cell signal recorded synchronously with each IR image, i.e. the IR detector system incorporates a reference signal input that is recorded with each IR image. This reference signal is scaled to vary between zero and one, shown schematically in Figure 4.3 (blue line); i.e. the IR image at the minimum load is defined as the zero displacement image over which all other IR images are overlaid. A corresponding displacement curve can then be generated for each IR image pixel represented by the black line in Figure 4.3. These displacement curves are calculated for each IR image pixel according to:

$$D = D_{\max}[(\sin(\theta n + \frac{3}{2}\pi) + 1)/2] \tag{4.3}$$

where $D_{\max}$ is the displacement interpolated at each pixel in the IR image when the maximum load is applied, θ is the interval between IR images expressed as an angle in radians such that $\theta = 2\pi f_l / f_r$, where f_l is the loading frequency and f_r is the frame rate of the IR detector (both in Hz) and n is the image number.

According to the computed displacement field, the position of each pixel can be redefined for each frame, and a series of corrected IR images can be constructed. The corrected pixel position was rounded to the nearest integer (i.e. sub-pixel displacements and associated temperature interpolations have been omitted as their effect was found to be negligible in the current work). The magnitude of the temperature change for each pixel is

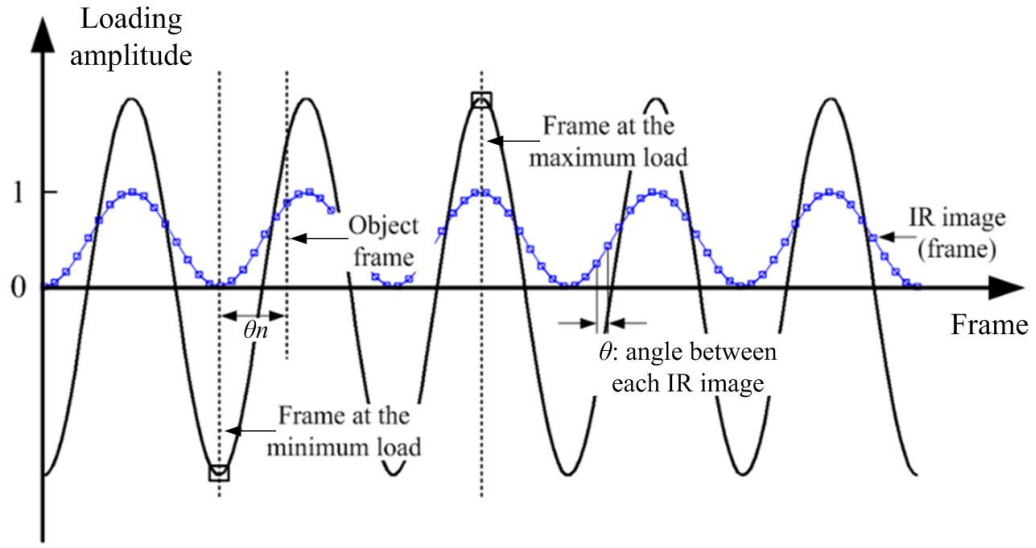

Figure 4.3: IR images associated with the load signal and the periodic wave

obtained from the motion compensated temperature time history using a FFT method. For the purpose of computational efficiency, the corrected IR and interpolated displacement images are not stored. Instead, each IR image pixel is processed in turn, a corrected temperature vector is constructed and input into FFT. The magnitude and phase values at the loading frequency are then stored in two output images; one for the magnitude data and one for the phase data. As described in Chapter 3, the phase data enables the identification of compressive and tensile stresses, with a 180° shift between the two. Moreover, it is also used to determine if the response is being influenced by factors other than the thermoelastic coupling (e.g. heat transfer by conduction and dissipation).

4.3 Experimental validation

4.3.1 Experimental arrangement

The feasibility of the MC method is demonstrated by correcting for the motion from TSA data captured around the edge of a circular hole in an aluminium alloy specimen. The material properties of the aluminium alloy were obtained experimentally and are shown in Table 4.1. The configuration of the specimen is shown in Figure 4.4 (a). The specimen was 2 mm thick by 50 mm wide with a length of 600 mm. An 8 mm diameter hole was produced using electro-discharge machining and located 190 mm from the end of the specimen, i.e. closest to the actuator of the servo hydraulic test machine. This was done to ensure sufficient motion, i.e. greater than an IR image pixel, around the hole during cyclic loading. The tests were conducted using an Instron 8802 servo hydraulic test machine (fitted with a 100 kN actuator and load cell). A cyclic load with 4.2 kN mean load and 3.4 kN load amplitude, with a frequency of 15 Hz, was applied to the specimen, also to generate motion around the hole which is large enough to be observed in the IR images. However a simple calculation based on an stress concentration factor of 3 shows that this load level will generate some plasticity in the neighbourhood of the hole (Table 4.1 provides the yield stress of the material). It was considered more desirable to generate a loading that would provide a measurable displacement rather than to reduce the load and avoid the plasticity

Table 4.1: Material properties for aluminium specimen

	Elastic modulus (GPa)	Poison's ratio	Yield strength (MPa)
Aluminium alloy	70	0.33	110

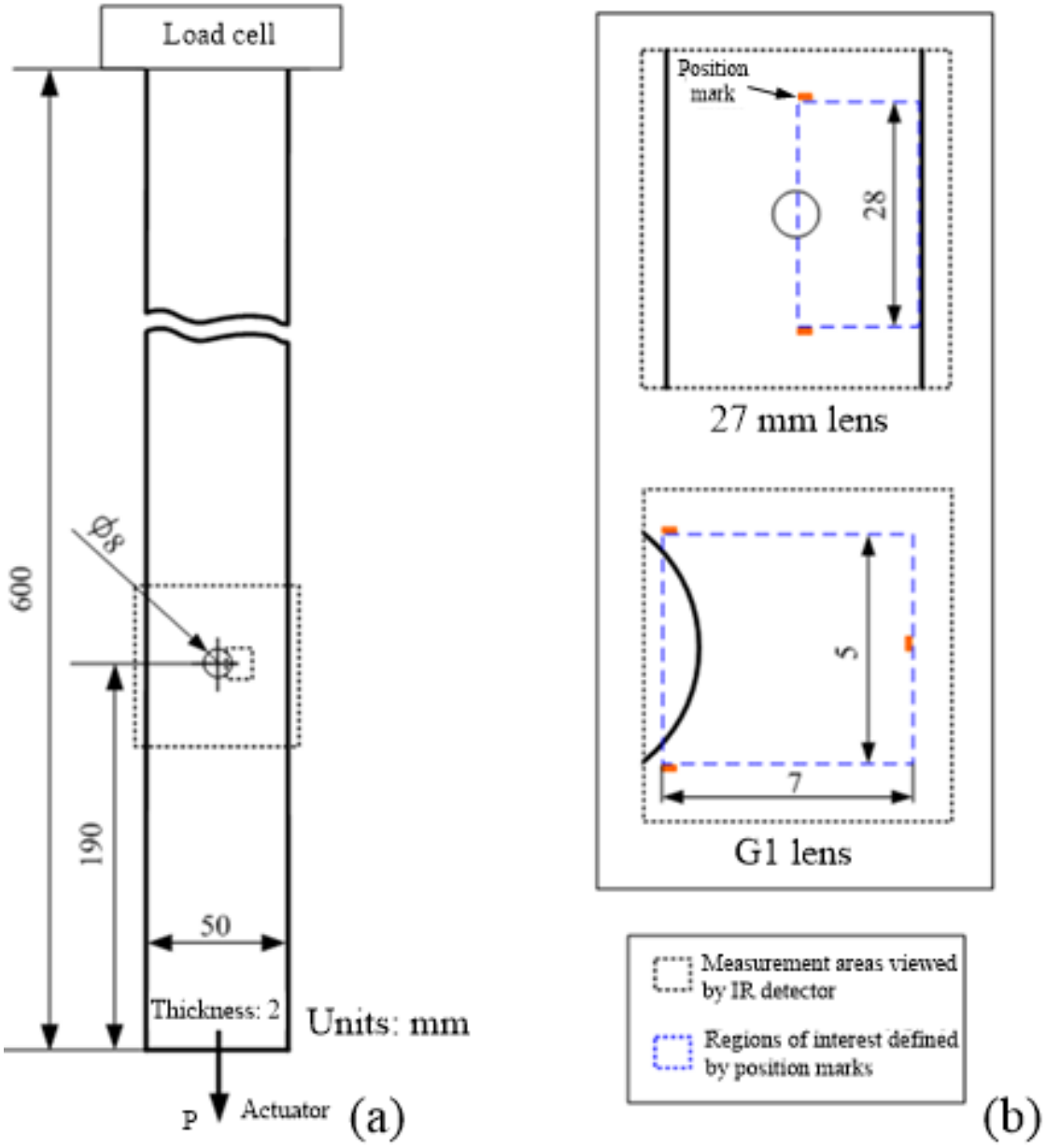

Figure 4.4: Test specimen and setup: (a) dimensions of the test specimen (b) measurement areas viewed by the IR detector with different lenses and the corresponding regions of interest

Prior to testing, the specimen was coated with two passes of RS matt back paint. The paint is required to provide a uniform and suitably high emissivity. The thickness of the paint can affect the thermoelastic response as a thick paint can attenuate the heat emitted from the specimen surface. As suggested in [119], the paint was applied so as to be in the range of 15 to 25 μm, which was confirmed using a Thikstik Dual Gauge produced by Sheen Instruments. Several position marks comprising reflective metal tape were placed on the coated specimen surface as shown in Figure 4.4 (b) to align the IR and DIC images.

In both IR and white light images, the areas bounded by the position marks were processed.

The IR images were captured using a 383 Hz frame rate. Two IR lenses were used. The IR images captured by the 27 mm lens conduct the MC at a relatively large scale with a resolution of 0.24 mm/pixel. The G1 lens was also used to evaluate the effectiveness of the MC at greater magnifications with a resolution of 0.03 mm/pixel. The measurement areas on the specimen surface of each of these two lenses are shown in Figure 4.4 (b).

The speckle pattern required for DIC was generated by spraying Ambersil matt white paint randomly onto the black coating. To achieve a similar field of view to that of the IR data capture, two different lenses were used to capture the white light images. A 105 mm lens (SIGMA) was set with a scale factor of 0.018 mm/pixel to provide a measurement area (45×37 mm^2) comparable to the 27 mm lens. A 65 mm macro lens (CANON MP-E) provided a field of view comparable to the G1 lens (8×7 mm^2 with a scale factor of 0.0033 mm/pixel). The specimen displacement was measured over the same loading range (from 0.8 kN to 7.6 kN) as used for the collection of the IR images.

4.3.2 Specimen motion analysis

It has been demonstrated that the accuracy of image correlation for DIC is mainly dependent on the subset size. A larger subset size increases the uniqueness for the correlation as more speckles are considered, thereby offering better displacement precision, but increasing computing time and reducing spatial resolution. To select an appropriate subset size, the displacement field extracted from the recorded images of two different lenses were computed using three different subset sizes: 32×32 pixels, 64×64 pixels and 128×128 pixels. The displacements at maximum load (7.6 kN) along the white dashed line in the inserts in Figure 4.5 were calculated for each of the three subset sizes and compared. The origin of the coordinate system was set at the centre of the hole; this coordinate system was used in all the plots in the following sections. As shown in Figure 4.5, the results from 64×64 and 128×128 exhibit almost the same trend, while the results from 32×32 present significant fluctuation. As the large subset size provides less spatial resolution, 64×64 was selected here as the optimum subset size. In Figure 4.5 the displacement divided from DIC shows an approximate 0.4 mm displacement at the edge of the hole. When comparing to the pixel size in the IR image, this displacement will introduce a 2 pixel movement when using the 27 mm lens and more than 10 pixels movement when the G1 lens is used.

Figure 4.6 shows the displacement field corresponding to the specimen images (the inserts in Figure 4.5) derived using the 64×64 subset size. The magnitude and direction

of the specimen deformation is presented by the vector arrows with different colours. It is reasonable to observe that the displacement field measured by the 105 mm lens shows a clear displacement gradient and vectors are straight downwards under the unidirectional load. Almost the same displacement vectors are observed in the small area close to the edge of the hole when 65 mm lens was used.

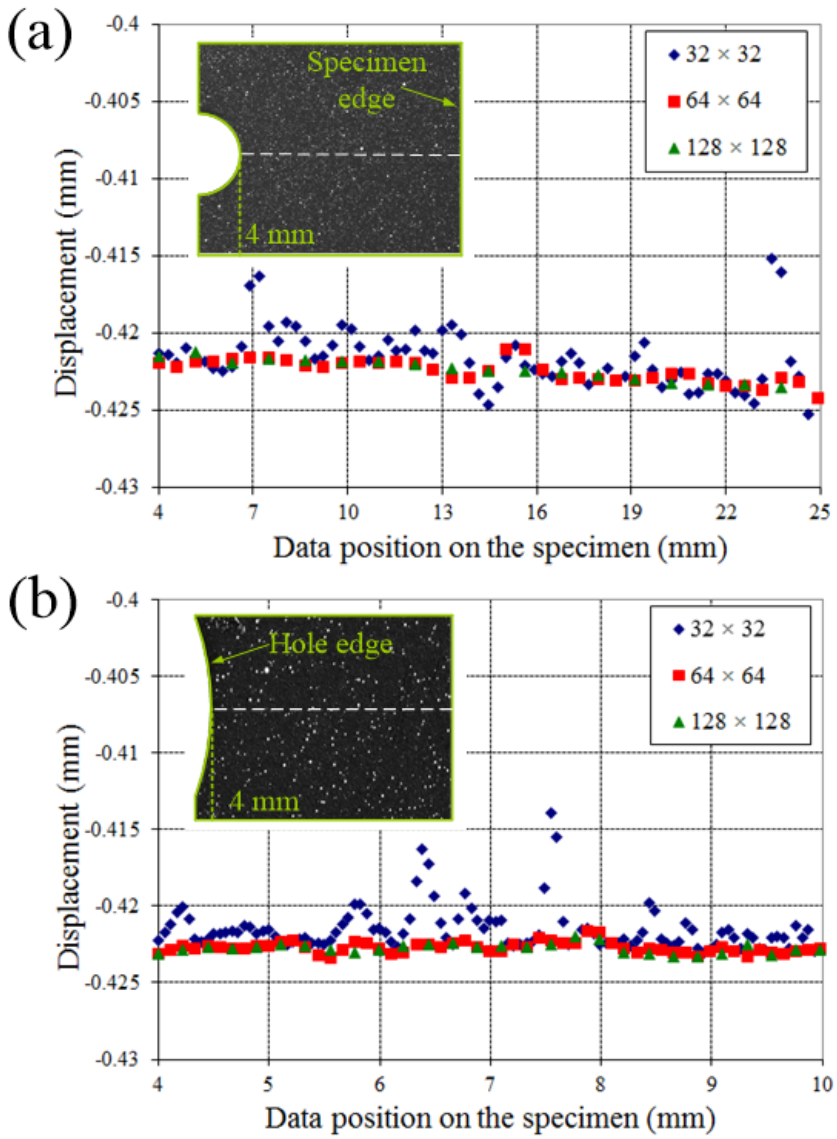

Figure 4.5: Displacements derived with different subsets: (a) 105 mm lens and (b) 65 mm lens

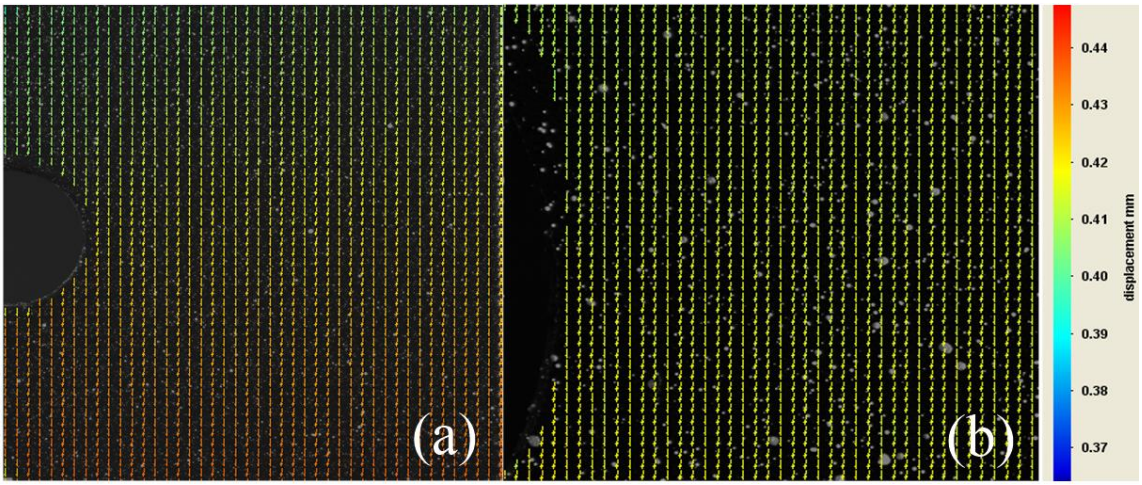

Figure 4.6: Specimen deformation obtained using the 64 × 64 subset size: (a) 105 mm lens (b) 65 mm lens

4.3.3 FE modelling

A 2D elastic-plastic FE model for the aluminium plate specimen was constructed using ANSYS FE software version 12.1 [120]. This model was used to evaluate the stress state around the circular hole and compare with the TSA results. A stress strain curve for the aluminium alloy was obtained experimentally to provide input into the model to describe the material plastic behaviour. A five point multilinear kinematic hardening plasticity model was used. The geometric model with FE mesh and the boundary conditions are depicted in Figure 4.7. Displacement constraints in both x- and y-directions were applied to one end of the specimen (close to the load cell) and a uniform stress was applied to the other end (close to the actuator) without displacement constraints. Figure 4.7 (b) shows the close-up mesh details in the red rectangular region as shown in Figure 4.7 (a). The mesh was highly refined in the neighbourhood of the hole, hence 2-D 4-node structural solid element (PLANE 182) were used with the material properties as given in Table 4.1.

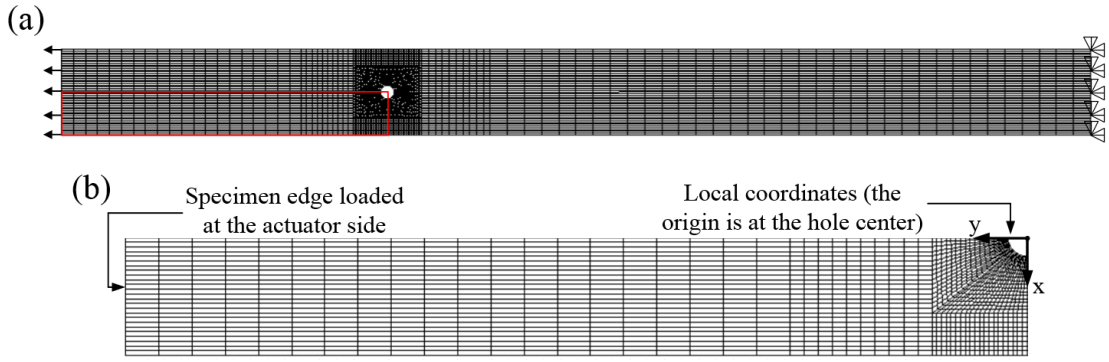

Figure 4.7: (a) FE model of the aluminium plate specimen with the boundary conditions and (b) close-up details of the mesh around the hole

4.3.4 Results

The stress data obtained from the TSA with and without applying the MC method are presented in this section and compared with the FE results. The stress states obtained from the setup of the 27 mm lens and the G1 lens are corresponding to the regions of interest as shown in Figure 4.4 (b). To enable a quantitative evaluation of the stress values obtained from the TSA, the thermoelastic constant, K_T, is required for the aluminium material. A value of $9.61 \times 10^{-12} \pm 0.16$ Pa^{-1} [119] was used to calibrate the TSA data.

The TSA results obtained with the 27 mm lens before and after MC are shown in Figure 4.8. In Figure 4.8 (a) the edge effect caused by calculations of the temperature difference between the specimen surface and the background is observed. The phase data in Figure 4.8 (c) also shows the edge effect. Figure 4.8 (b) shows that the MC enables data to be obtained close to the edge of the hole. A second artefact of motion, most noticeable in the lower half of the image in Figure 4.8 (a), is due to the surface roughness of the specimen. The emissivity is uniform at approximately 92%. Hence 8% of the environmental radiation is reflected back from the surface into the detector. The surface texture causes

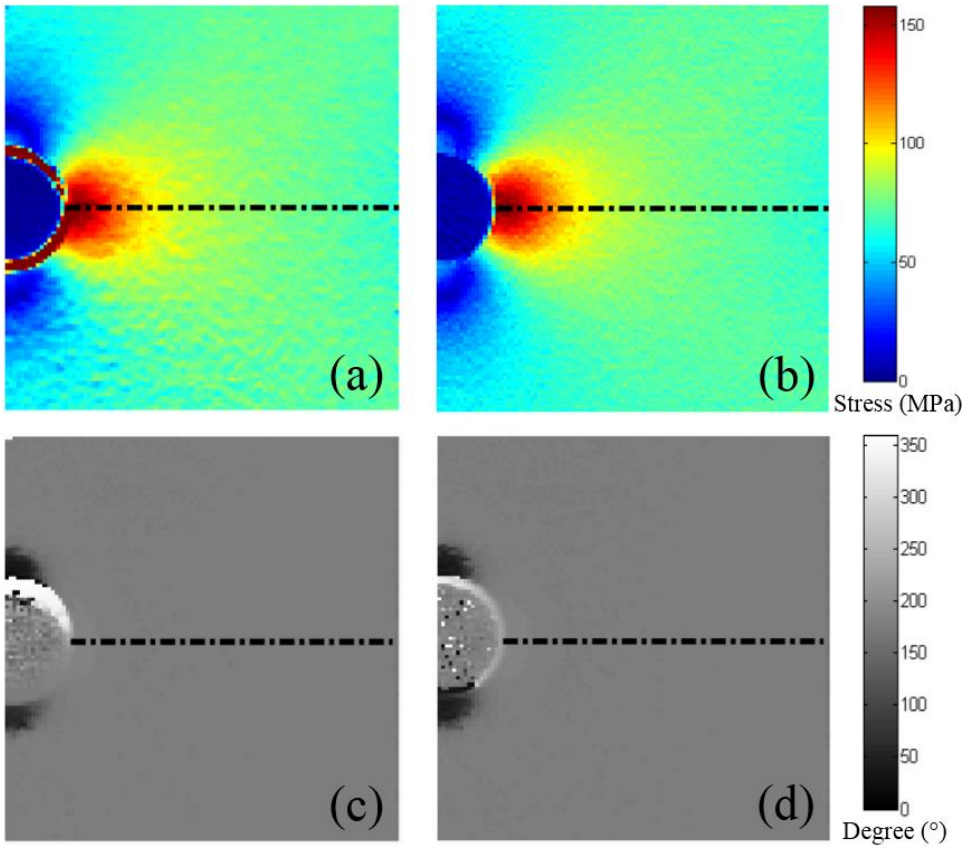

Figure 4.8: The change in the sum of principle stresses and phase shift obtained by 27 mm lens: (a) stresses without MC, (b) stresses with MC, (c) phase shift without MC, (d) phase shift with MC

this reflected radiation to have different sources. Where the surface is perpendicular to the line of sight of the detector, 8% of the detectors own emissions (76 K) are reflected back. In other locations on the specimen surface 8% of the background emissions (290 K) are reflected into the detector because the surface is not perpendicular to the line of sight. At low spatial resolutions, this texture is mostly averaged within a single pixel, but a slight effect is still visible in the processed data. Once MC has been applied, the reflected portion of the temperature measurement is a constant offset at each measurement point (i.e. each point on the specimen surface is always reflecting the same background source) and hence has a negligible influence on the FFT processing which evaluates only with the sinusoidal component of the signal.

To provide a quantitative comparison of the data sets before and after MC, line plots along the back dashed line in Figure 4. 8 are shown in Figure 4.9. Little difference can be seen in the data before and after applying MC, especially away from the edge of the hole. This is because the motion has little effect when the stress field is relatively uniform. The scatter is, however, slightly larger without MC due to the surface texture effect. The results after MC show a good agreement with the FE results. The discrepancy between the TSA and FE results very close to the edge of the hole results from the localised plasticity modifying the thermal response and hence the calibrated stress values. A further, and possibly more important, influence is the large stress gradient in the neighbourhood of the hole, so heat transfer within the specimen cannot be entirely eliminated. This is confirmed by the phase data (see Figure 4.9 (b)) where the heat diffusion leads to a phase shift coincident with change in the stress gradient. The influence of the plasticity and the heat transfer on the response warrants a further study but is outside the scope of the present work where the focus is on developing the MC technique. For this purpose the MC approach is demonstrated by the significant improvement in the experimental data.

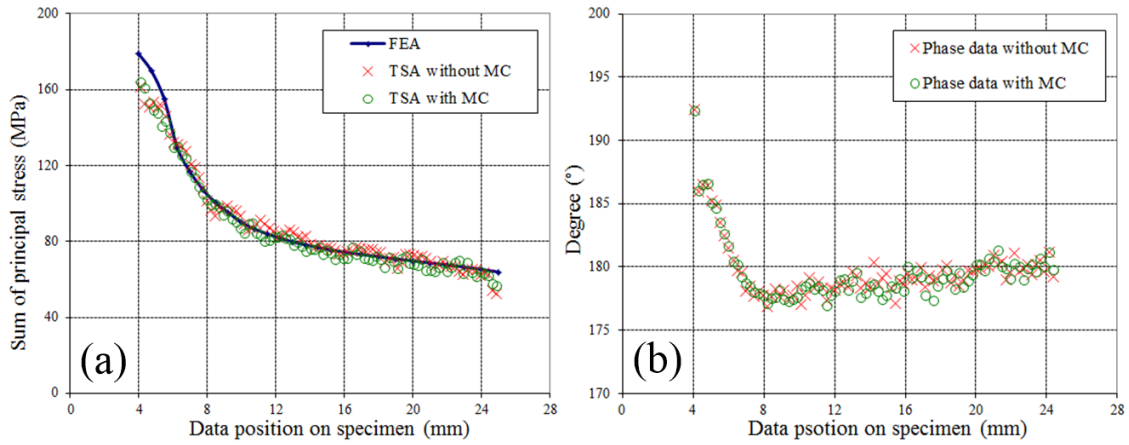

Figure 4.9: Line plots of the TSA data and the FE results: (a) the comparison of the stresses from TSA with the FE analysis, (b) phase data before and after MC

The effect of motion is more significant when the G1 lens is used. The TSA data adjacent to the hole before MC are shown in Figure 4.10 (a). The specimen motion can be observed by a large shift of the position marks, the two regions of very large stress where the hole edge curves towards the horizontal and the effect of the surface texture (barely visible in the raw IR images), that completely masks the stress field, causing the entire image to appear blurred. After employing the MC method (Figure 4.10 (b)), a clear stress gradient in the vicinity of the hole can be observed. The profile along the edge of the hole can be clearly identified which indicates that the influence of the motion has been significantly reduced. The data along the line marked in Figure 4.10 is plotted alongside the FE results and with the TSA data obtained with the 27 mm lens in Figure 4.11. There is a very large scatter in the data collected with the G1 lens before MC, which is significantly reduced after the MC was applied. The results obtained from the G1 lens after MC are similar to the results obtained from the 27 mm lens.

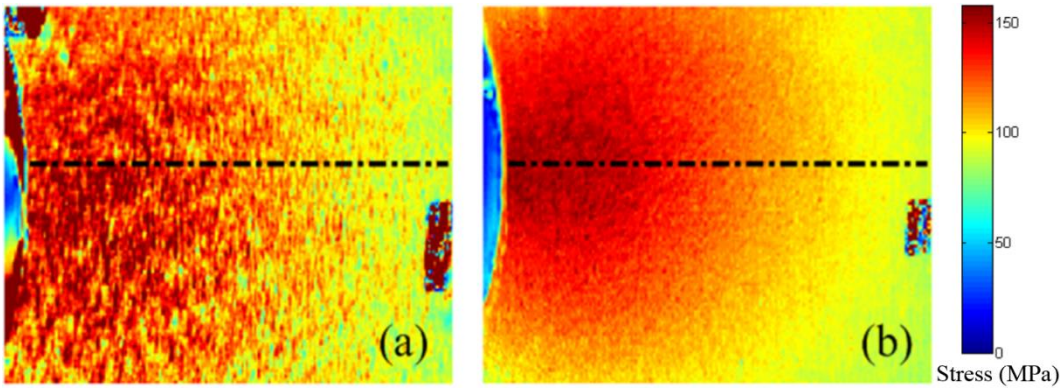

Figure 4.10: The change in the sum of principal stresses obtained with the G1 lens: (a) without MC, (b) with MC

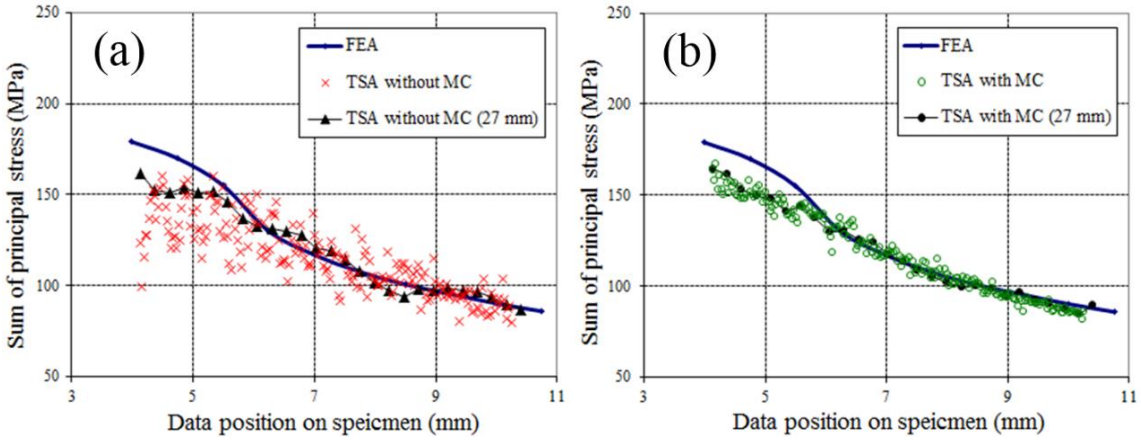

Figure 4.11: Line plots of the FE results and TSA data obtained from both the G1 lens and the 27 mm lens

4.4 Practical considerations

The work in the previous section validated the proposed MC approach using a best practice surface preparation for the DIC and the TSA. This presupposes an unchanging field between conducting the TSA and the DIC. However in many situations, such as fatigue testing it would be desirable to collect the IR images for the TSA and the images for the DIC at the same time. This would require a single coating that can be used for both the TSA and the DIC. The purpose of the present section is to show that a speckle pattern can be applied that provides sufficient contrast for the DIC but does not influence the TSA. This is possible as the emissivities in the white light and IR spectra are not necessarily the same. Hence, if a suitable combination of black and white paint is used, IR images can be collected without any influence of the speckle pattern. Tests were conducted using the same aluminium specimen as used in the first set of tests.

The test specimen was painted with both the black coating and the black and white speckle pattern. Data were collected from the vicinity of the hole using the G1 lens to magnify any influence of surface irregularities. The speckle pattern used in this work observed in the neighbourhood of the hole is shown in Figure 4.12 (a). To assess the speckle characteristics, the edge detection method developed in [121] was used to evaluate the size and number of the speckles in the speckle pattern. As an example shown in Figure 4.12 (b), the edge detection method converts the speckle pattern image to a binary speckle pattern from which the speckle size and the number of speckles can be analysed. Figure 4.13 shows the frequency distribution of the speckle sizes present within the pattern in Figure 4.12 (a). The predominant speckle size is 0.2 mm^2 which is equivalent to 60 pixels per speckle at high resolution. The pattern has a speckle density of about 36 pixels per mm^2.

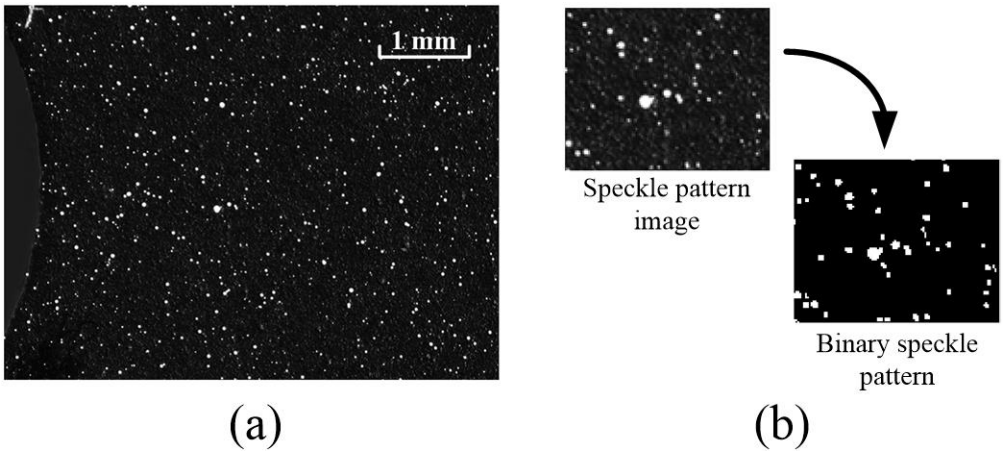

Figure 4.12: (a) Speckle pattern in the vicinity of the hole and (b) conversion of the speckle pattern image to the binary speckle pattern

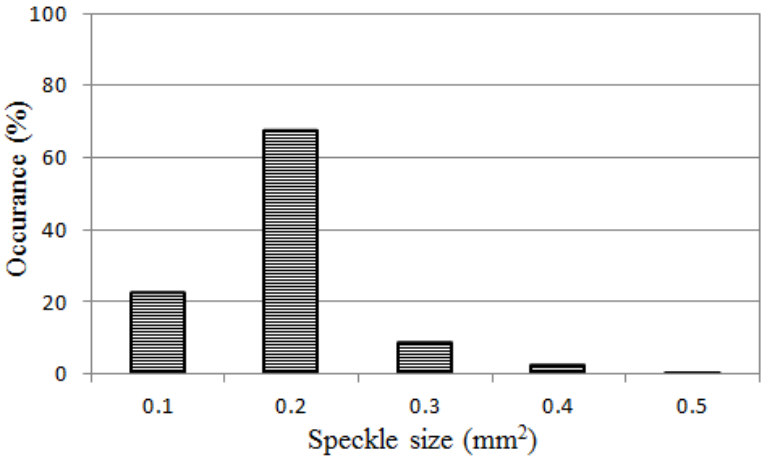

Figure 4.13: The frequency distribution of the speckle size within the pattern

The IR images captured from the specimen without and with the speckle pattern are shown in Figure 4.14 (a) and (b) respectively. It can be seen that the IR images show a similar temperature distribution, with almost no discernible differences that can be attributed to the speckle pattern shown in Figure 4.12 (a). This indicates that the speckle pattern used in this work has almost the same emissivity as that of the matt black coating. To evaluate the influences of the speckle pattern on TSA, the proposed MC method was applied to the IR images; Figure 4.14 (c) and (d) show the stress amplitude around the edge of the hole obtained without and with speckle pattern respectively. In both images the stress distributions around the edge of the hole present a comparable geometry and magnitude.

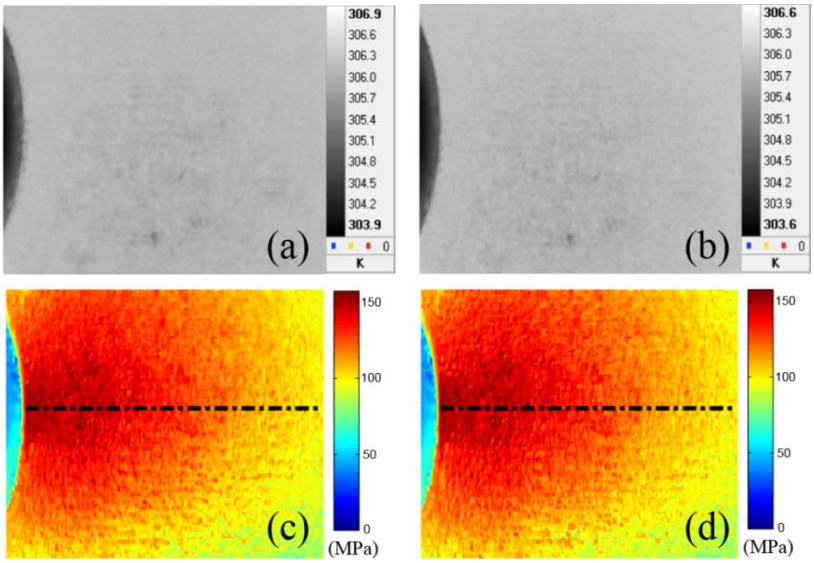

Figure 4.14: Comparison of the IR images and TSA data with different coatings: (a) IR image with black coating, (b) IR image with black-white speckle pattern, (c) TSA with black coating, (d) TSA with black-white speckle pattern

To provide a quantitative comparison of the two data sets, the data along the line marked in Figure 4.14 (c) and (d) are plotted and compared with the FE results in Figure 4.15. Little difference can be observed from the stress data collected from the black coating and the speckle pattern. This shows that the speckle pattern used in this work has almost no influence on the TSA data. Thus, the possibility to perform the measurements for TSA and DIC from the same specimen surface preparation is confirmed.

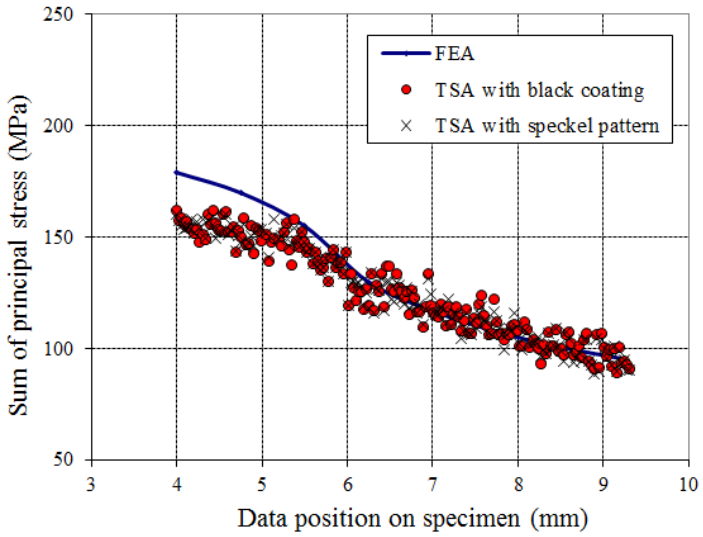

Figure 4.15: Line plots of the TSA data obtained from both black matt paint and speckle pattern

4.5 Summary

A high spatial resolution MC method based on DIC has been developed for TSA. This method enables the use of a white light camera with high spatial resolution to capture images for DIC thereby increasing the accuracy of the MC. The feasibility of the MC method for TSA was investigated by studying the thermoelastic response around the edge of the hole using two lenses with different resolutions. It has been shown that the MC method can significantly improve the accuracy of TSA measurements, especially when a magnifying lens is used.

It has been demonstrated that by using a suitable combination of black and white paint, a high contrast speckle can be used that has a uniform emissivity in the IR spectrum. This enables high spatial resolution and high fidelity displacement fields to be obtained without any need to reapply the surface preparation between DIC and TSA data capture or to interpolate across low emissivity speckles in the TSA data. Thereby this approach to MC enables the monitoring of fatigue crack growth, and other applications with complex

and time varying motion fields. The speckle pattern used in this work has a speckle density of about 37 pixels per mm^2 and most of the speckle has sizes between 0.1 and 0.2 mm^2. This kind of speckle pattern is used through the following work to allow the measurements for TSA and DIC to be taken from the same specimen surface during the tests.

Chapter 5

TSA of interfacial cracks in foam cored sandwich structures

5.1 Introduction

The primary motivation to develop the MC method described in Chapter 4 is to correct for the discontinuous motion field at the debonded area in sandwich structures, and hence enable reliable TSA data to be obtained at the crack tip. Furthermore, the aim is to apply the MC method to interfacial cracks in a foam cored sandwich structure to demonstrate the feasibility of using TSA to determine the interfacial crack tip stresses.

The test was conducted using the double cantilever beam (DCB) test method (see section 2.4.3). This test configuration has been widely used for characterising the interfacial debonding of sandwich beams under mode I loading conditions. Compared to other test methods such as the cracked sandwich beam (CSB), three-point sandwich beam (TPSB) and mixed mode bending (MMB), the DCB test configuration is much less complicated as only two hinges bonded on the upper and lower face sheet are required. However, as the load is applied directly to the hinges, the motion of the sandwich specimen is much greater and complex as rotation of the specimen will occur with the opening of the debond making motion compensation challenging. Hence the DCB test configuration was selected to demonstrate the capability of the MC method for the correction of complex motion across the face sheet/core interface.

The thermoelastic constants of the face sheet and core material are determined so an FE model of the sandwich specimen loaded in the DCB test configuration can be calibrated

for comparison with the TSA. It is shown that the MC method can correct for the complex and non-uniform motion, thereby enabling useful thermoelastic data to be obtained from the vicinity of the crack tip.

5.2 Test specimens

Sandwich specimens consisting of 25 mm thick Divinycell H100 cross-linked PVC foam cores and E-glass/epoxy composite face sheets were studied as shown in Figure 5.1. The face sheet comprised eight layers of plain woven, 210 g/m^2 E-glass textile, giving a face sheet thickness of 1.6 mm. The through-thickness direction of the foam was placed along the y axis and the in-plane direction was placed along the x axis (as defined in Figure 5.1).

Firstly, a sandwich panel was manufactured using the RIM approach as described in Chapter 2. The epoxy resin used to form the sandwich structure was Prime 20LV from Gurit, cured using their fast hardener. During the material lay-up, a 25 μm thick Teflon strip was placed between the upper face sheet and the core to create a controlled debond region across the width of the panel.

Test specimens of 200 mm length and 32 mm width were cut from the sandwich panel and loaded as in Figure 5.1. The specimen includes a 50 mm initial crack length at one end of the specimen. The steel hinges were especially made for the DCB test with a thickness of 1.25 mm and 35 mm width. Importantly, the hinge joint is friction free so that no extra force is introduced under the peel load during the test. The hinges are shown in Figure 5.1; these were adhesively bonded to the upper and lower face sheets using an Araldite^{TM} epoxy resin and cured at room temperature for at least 12 hours.

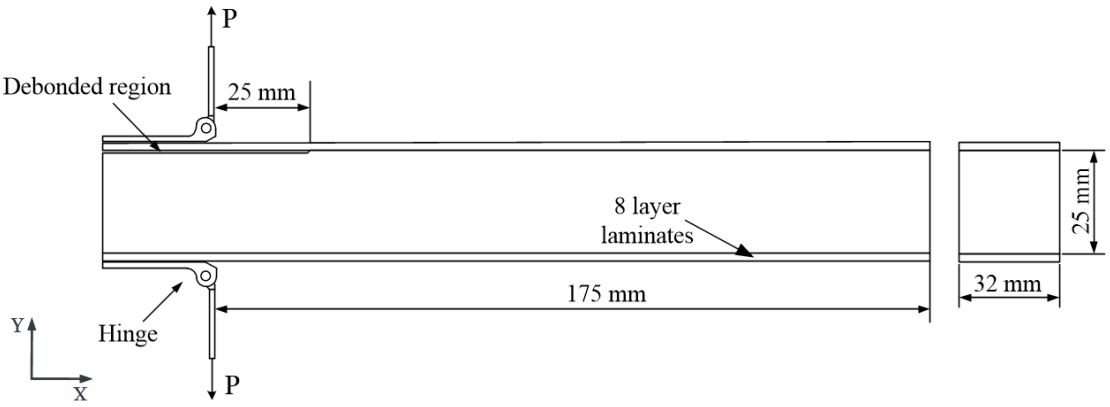

Figure 5.1: The dimension of the DCB sandwich beam specimen

The foam material has been macroscopically considered as an orthotropic material in previous studies [122, 123]. The yielding strength along the in-plane direction of the foam is around 2.5 MPa which is almost 36% lower than its through-thickness strength (around 4 MPa) [123]. An image of the microstructure of the foam taken from the foam surface after cutting is shown in Figure 5.2. The highly irregular cellular structure of the foam can be clearly seen in the image. The individual cells can be clearly identified in most of the areas, while in some parts of the image (e.g. the red marked region) almost no cells can be observed on the surface. The morphology variations may introduce inhomogeneous stress states in the foam material.

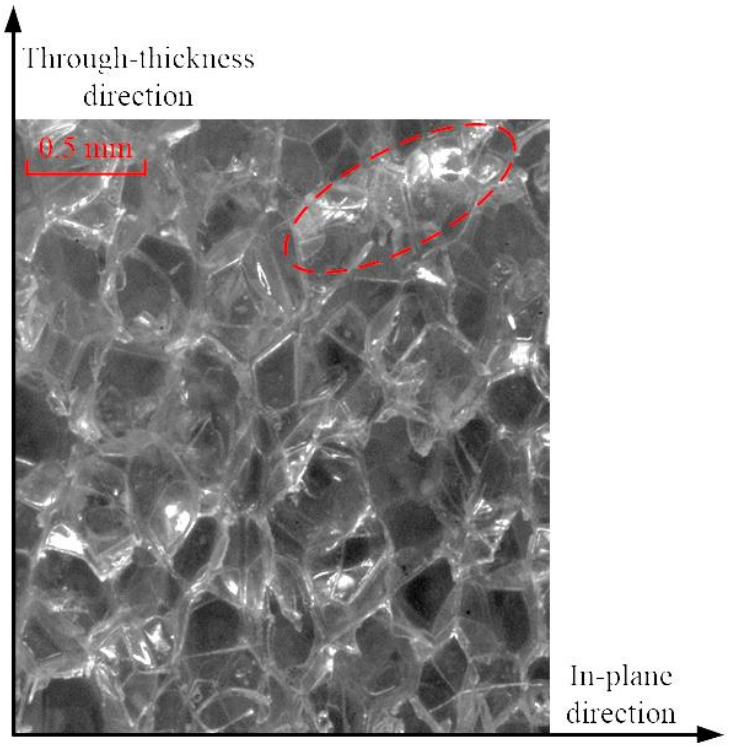

Figure 5.2: Micro-structure of Divinycell H100 foam

5.3 Evaluation of thermoelastic constants of the face sheet and core material

5.3.1 Core material

The experimental setup for obtaining the thermoelastic constant of the foam material is shown in Figure 5.3. As the foam is orthotropic, the thermoelastic constants along its in-plane direction and through-thickness direction are different. Thus, two different specimens were prepared in which the uniaxial load was applied along the material in-

plane direction and through-thickness direction separately as shown in Figure 5.3 (1 represents the through-thickness direction, 2 and 3 are the in-plane directions). The length of the through-thickness specimen was 65 mm which is the maximum length along the through-thickness direction of the foam provided by the manufacturer. For the in-plane specimen, the length of the specimen is not limited. A length of 80 mm was chosen in this work aiming to produce a uniform uniaxial tensile stress in the middle of the specimen. The foam specimens were adhesively bonded to the steel end tabs using the Araldite^{TM} epoxy resin. The foam surface was coated with two passes of RS matt black paint to produce a uniform high emissivity which was also used for the DCB test. The calibration tests were conducted using an Instron E1000 test machine (a 1 kN actuator and load cell) with a loading frequency of 3 Hz (the loading frequency is the same as that used for the DCB test). The thermoelastic constant was derived from a several tests with different stress amplitudes applied to the in-plane (0.08 MPa, 0.16 MPa and 0.32 MPa) and through-thickness specimens (0.16 MPa, 0.32 MPa and 0.48 MPa). The average $\Delta T/T$ value in the region of interest (20 mm × 20 mm) in the middle of the specimen as in Figure 5.3 was used for calculating the thermoelastic constant.

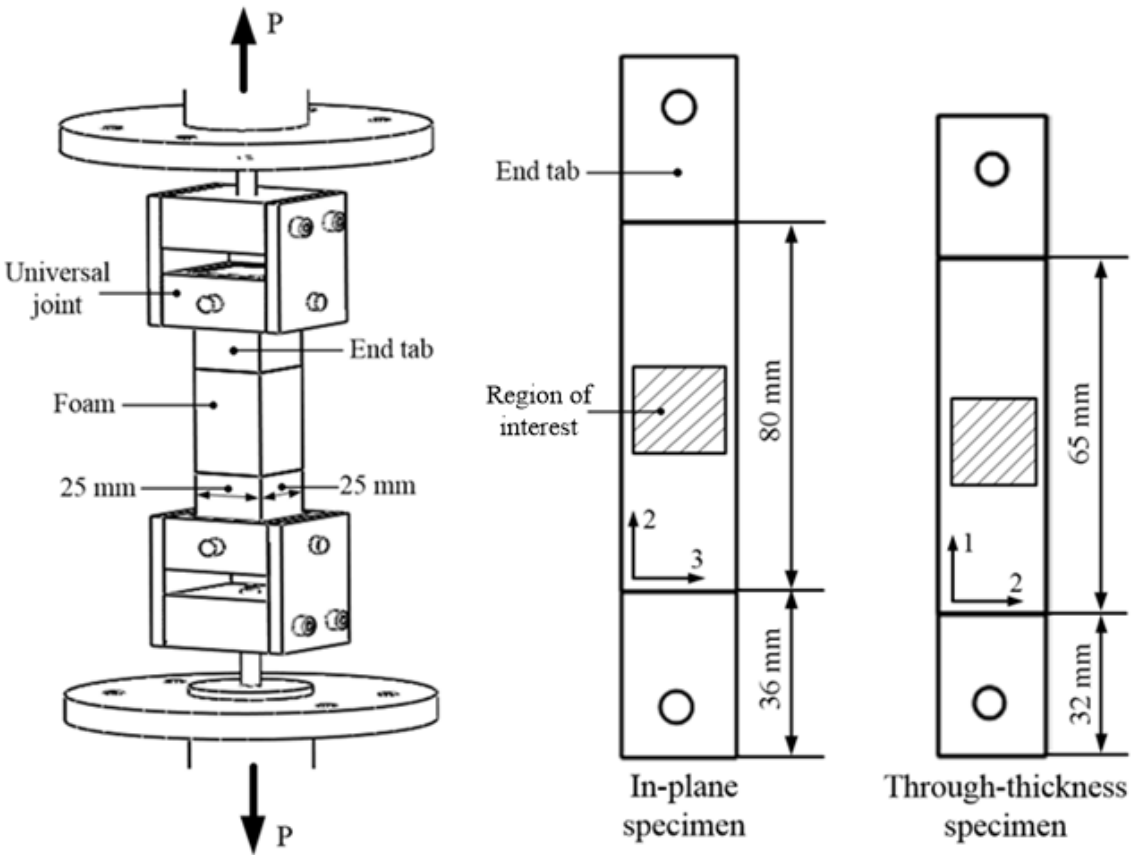

Figure 5.3: Experimental setup for obtaining the thermoelastic constants of the foam in its in-plane and through-thickness directions

It should be noted that a nonuniform stress state may exist in the specimen as the lateral displacement at the top and bottom of the specimen is constrained by the bonding of the specimen to the end tabs [122, 124]. The nonuniform stress state can be significant when the length of the specimen is too short. In this case the length in the through-thickness direction of the specimen is limited. As has been described in Chapter 3, thermoelastic constant, K_T, is calculated based on the $\Delta T/T$ value obtained from the specimen surface and the corresponding changes in the sum of principal stresses as:

$$K_T = (\frac{\Delta T}{T})/(\Delta\sigma_1 + \Delta\sigma_2) \tag{5.1}$$

Under the nonuniform stress state, K_T cannot be calculated directly from the applied stress amplitudes on the specimen. This is because the $\Delta T/T$ value obtained for TSA correspons to the specimen surface stress which cannot be represented by the global response of the specimen. To investigate the stress state of the foam specimen, a FE analysis was performed to assess the relationship between the surface stress and the average stress applied on the specimen. A 3D elastic FE model was constructed using the commercial software ANSYS 12.1. Figure 5.4 (a) shows the model of the through-thickness foam specimen. Both through-thickness and in-plane models were built using 8 node linear-elastic elements SOLID185 with the minimum element size of 1 mm^3 used for the foam. The adhesive layer between the foam and the end tabs was not considered as its influence on the stress distribution in the foam has been proved to be negligible [122]. A tensile stress with 0.5 MPa was applied on the surface of one end tab, while displacement constraints in the 1, 2 and 3 directions were applied to the surface of the other end tab. The material properties are shown in Table 5.1 [122].

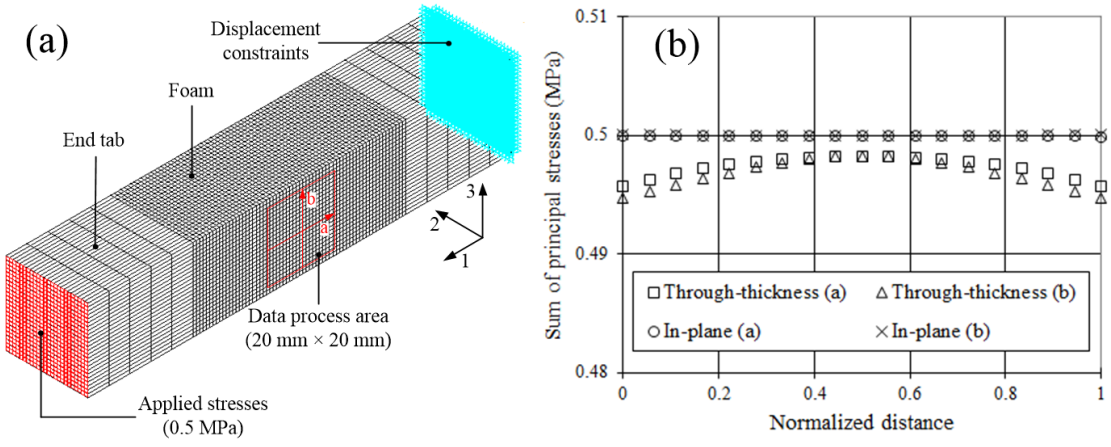

Figure 5.4: (a) FE modelling of the through-thickness foam specimen, (b) line plot of the sum of principal stresses along line a and b obtained from the through-thickness specimen and the in-plane specimen

Table 5.1: Material properties of H100 PVC foam [122]

Material	E_1 (MPa)	E_2, E_3 (MPa)	Gs_{12} (MPa)	Gs_{23} (MPa)	v_{12}	v_{21}	v_{23}
Foam	132	58	33	19	0.41	0.17	0.4
Steel	210000	210000	87500	87500	0.32	0.32	0.32

Figure 5.4 (b) plots the sum of principal stresses along the lines a and b at the specimen surface (see Figure 5.4 (a)) obtained from the FE solutions. Here a normalised distance is shown. For the in-plane specimen, a uniform stress state can be seen in the middle area of the specimen and the stress value is almost the same as the global stress (0.5 MPa). For the through-thickness specimen, the stress is nonuniform over the specimen surface with values lower than the average stress. Therefore the relationship between the surface stress and the global stress applied on this specimen must be established. A stress correction factor, ϱ, for the through-thickness specimen was obtained from:

$$\varrho = \frac{\Delta\sigma_s}{\Delta\sigma_g} \tag{5.2}$$

where $\Delta\sigma_s$ is the average stress values in the region of interest (20 mm × 20 mm) on the specimen surface and $\Delta\sigma_g$ is the global stresses applied on the specimen. The value of ϱ was 0.99, indicating a small effect on the derived thermoelastic constant.

Figure 5.5 shows the thermoelastic constants obtained from different specimens subjected to different applied stress amplitudes. Figure 5.5 (a) and (b) show the results obtained from the in-plane and the through-thickness specimens respectively. It can be seen that the values vary more at lower stress amplitudes (0.08 MPa) in Figure 5.5 (a). This is because the temperature change was low so that the influence of the noise was large. In both figures, as expected, the thermoelastic constant shows almost no dependence on the applied stress amplitudes. It can be seen that the obtained thermoelastic constant along the through-thickness direction is approximately 1.5 times higher than the value along the in-plane direction. The average values of the thermoelastic constants are calculated as shown in Figure 5.5 which are 2.29×10^{-10} Pa^{-1} for the in-plane direction and 3.47×10^{-10} Pa^{-1} for the through-thickness direction.

The thermal properties of the Divinycell H100 foam from the data sheet in [125] are listed in Table 5.2. The foam material is treated as isotropic in the data sheet. The thermoelastic constant calculated from the values given in Table 5.2 is 2.06×10^{-10} Pa^{-1} which shows a fair agreement with the results for the in-plane direction obtained in

current work. It is clear that the thermal properties provided in the data sheet were measured from the material in-plane direction.

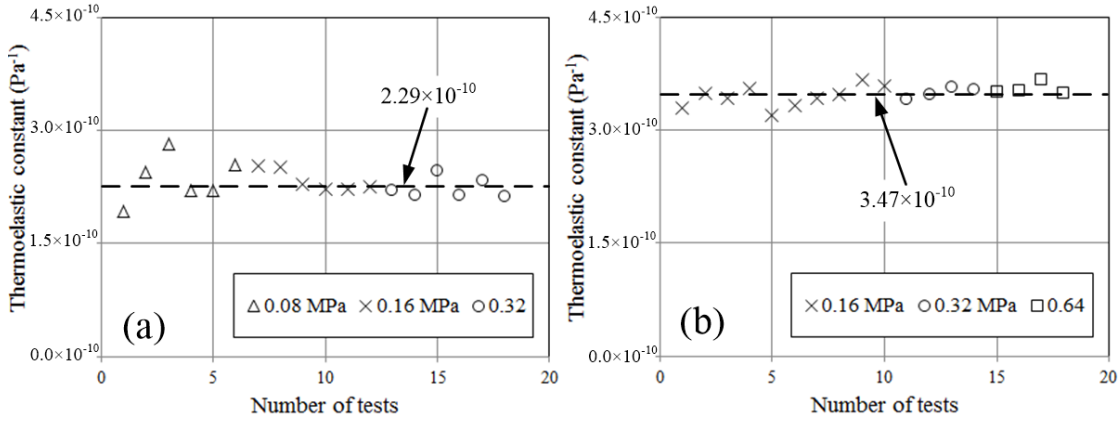

Figure 5.5: Thermoelastic constant obtained from the foam specimens (a) in-plane direction and (b) through-thickness direction

Table 5.2: Thermal properties of the Divinycell H100 foam [125]

Material	Test method	Results
Density	____	100 kg/m^3
Coefficient of linear thermal expansion	ASTM D696	35 (10^{-6}/°C)
Specific heat capacity	____	1.7 (J/g °C)

5.3.2 Face sheet material

A test specimen was constructed from the same eight-layer glass/epoxy laminate as the face sheet in the sandwich specimen; see Figure 5.6 (a). The specimen was 300 mm in length and of 30 mm width and fitted with 1.5 mm thick aluminium end tabs (50 mm long). The specimen was loaded in tension to obtain the thermoelastic constant for the face sheet material in the through thickness plane in the in-plane direction. Since the stress state in the face sheet is dominated by in-plane normal stresses with very small transverse normal stresses, it was decided that it was only necessary to derive the thermoelastic constant in the in-plane direction, thereby neglecting any contribution from the transverse stress. This was assessed as a reasonable assumption based on the output from the FE analysis.

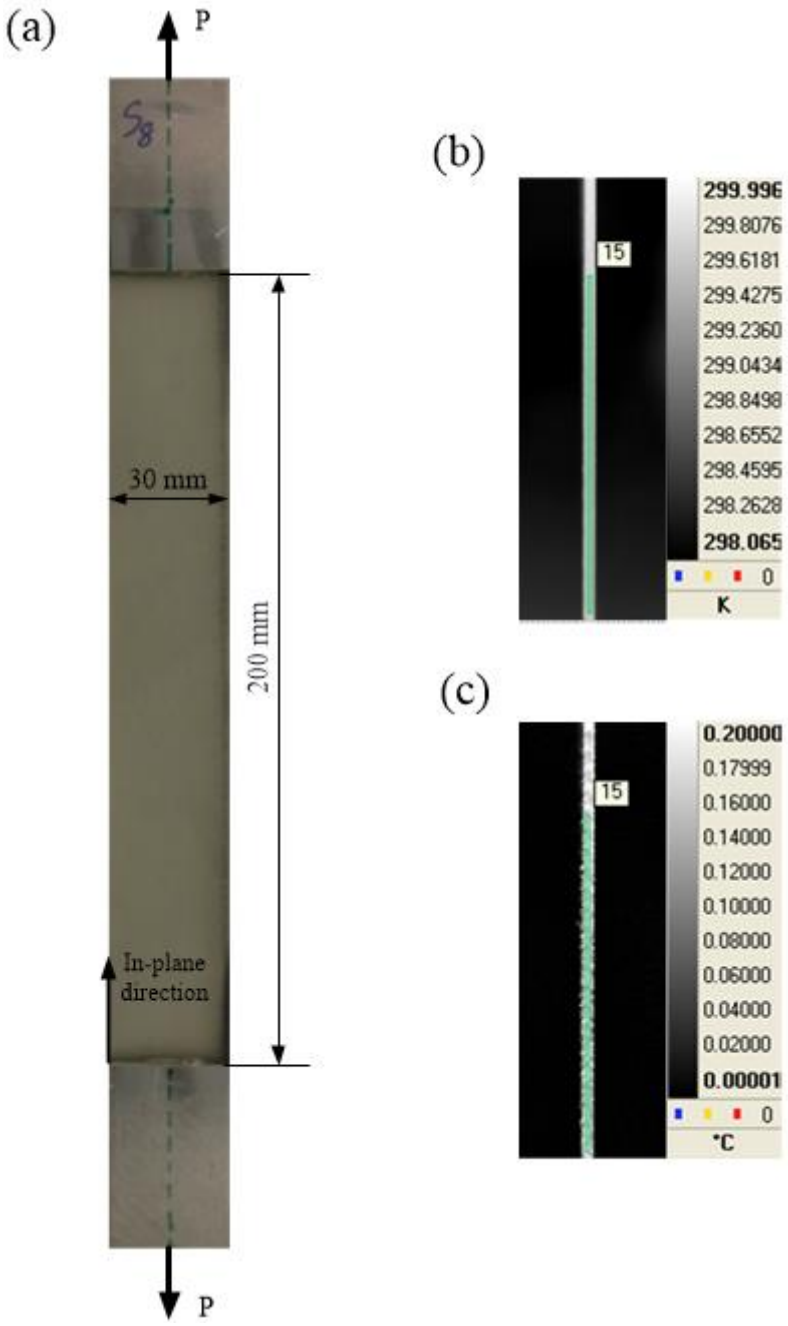

Figure 5.6: The composite specimen for stress calibration for the face sheet of the DCB test: (a) specimen dimensions, (b) thermal image and (c) ΔT image obtained from the side of the specimen

The specimen was cyclicly loaded with 3 Hz loading frequency. 1 kN loading amplitude and 2 kN mean load were applied. The surface was painted with two passes of RS matt black paint. Figure 5.6 (b) and (c) show an example of the thermal image and the ΔT image obtained from. The measurements were taken from the middle area of the specimen. Three specimens were tested in an Instron 8802 servo hydraulic test machine (fitted with a 100 kN actuator and load cell). For each specimen the $\Delta T/T$ value was

derived from the average value in the same rectangular area as shown in Figure 5.6 (b) and (c). The thermoelastic constant was then calculated from the applied stresses (i.e. 2 kN divided by the cross-section area) and the $\Delta T/T$ value. Figure 5.7 shows the values of thermoelastic constant obtained from the three different specimens. The error bar represents the standard derivation (SD) of the values in the rectangular area in Figure 5.6 (b). The obtained thermoelastic constant has an average value of about 1.1×10^{-11} Pa^{-1}. It is shown that the thermoelastic constant of the composite is about 20 times smaller than that of the foam material.

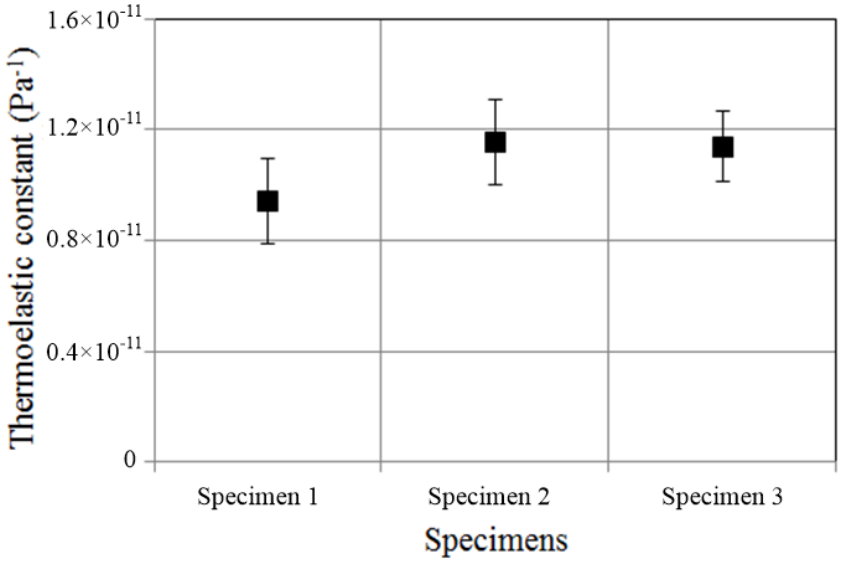

Figure 5.7: Thermoelastic constant of the composite derived from different specimens

5.4 TSA of a stationary crack tip

5.4.1 FE modelling

A 2D FE model of the DCB sandwich specimen was constructed in the commercial software ANSYS 12.1. The DCB sandwich model is shown in Figure 5.8 (a) with a highly refined mesh at the crack tip (see Figure 5.8 (b)). The total number of elements used in the model was 21266 and the minimum element size the crack tip was 0.1 mm. The model was built using a four-node plane element PLANE182. Since there is a considereble stiffness difference between the steel hinge and the composite face sheet, the model includes the steel hinge (see red rectangular area in Figure 5.8 (a)). The boundary conditions were applied directly to the steel hinge as a unidirectional load in the y direction with a displacement constraint imposed in the x direction. The constituent material properties input into the model are shown in Table 5.3.

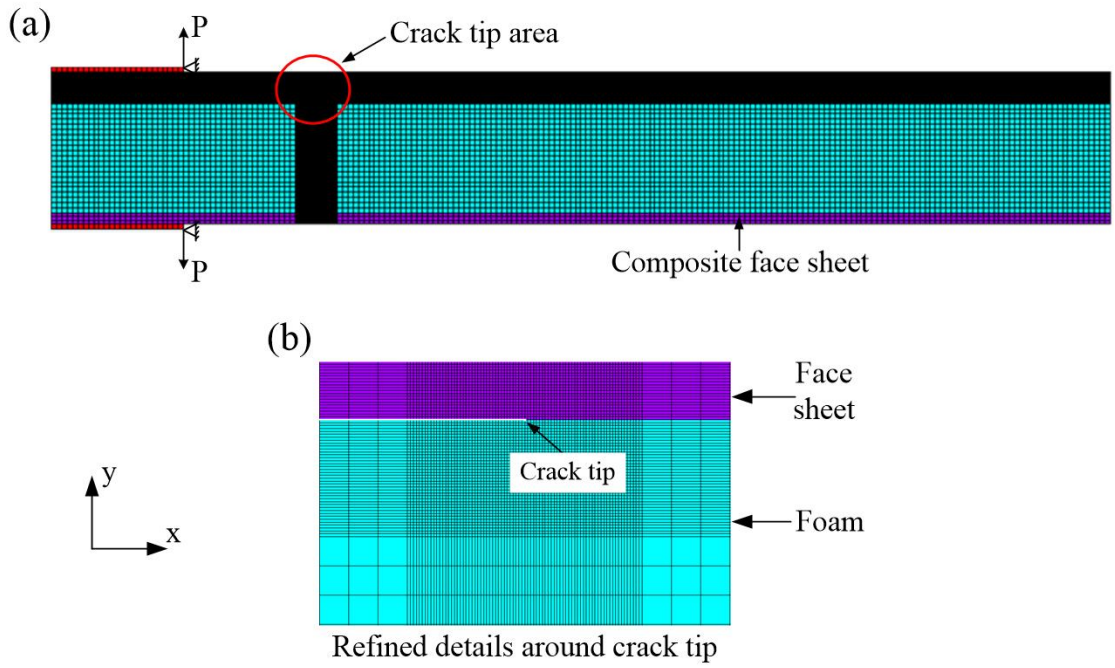

Figure 5.8: 2D DCB specimen model: (a) the DCB specimen and boundary conditions and (b) crack tip details

Table 5.3: Properties of the constituent materials of the sandwich beams [122]

	E_x (MPa)	E_y (MPa)	Gs_{xy} (MPa)	υ_{xy}
Composite	17000*	___	6841*	0.31*
Foam	58	132	33	0.17
Steel	210000	___	___	0.32

* Obtained experimentally

5.4.2 Experimental arrangements

The DCB test was conducted using an Instron E1000 test machine with a 1 kN actuator and load cell capacity. The specimen was clamped via the steel hinges in the standard Instron mechanical grips. The DCB specimen was loaded using displacement control with an amplitude of 1 mm, giving an approximate load amplitude of 30 N at a frequency of 3 Hz. The low cyclic loading frequency was chosen to avoid any heating of the foam around the crack tip [100].

Thermal images were collected from the side of the specimen using both the 27 mm lens and the G1 lens as shown in Figure 5.9. The cellular structure of the foam material can be observed in the thermal image (Figure 5.9 (b)) when the high magnifying G1 lens was used. The fields of view with the setup of the 27 mm and G1 lens were approximately 80 × 60 mm^2 and 9.5 × 7.5 mm^2 respectively. The areas of interest are indicated by the black dashed line in Figure 5.9. The areas are divided into two regions: an upper region which contains the upper (partly debonded) face sheet, and a lower region that comprises the foam core and the lower fully attached face sheet (just the foam core in the G1 lens image).

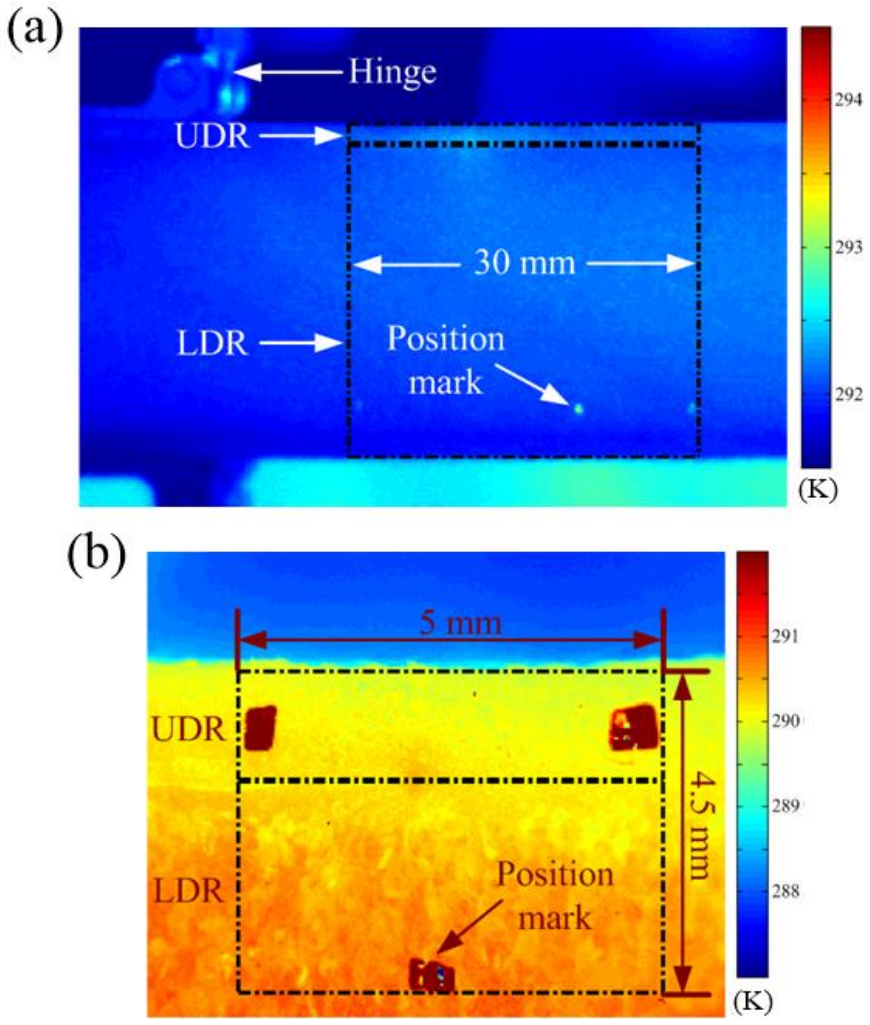

Figure 5.9: Thermal images measured by: (a) 27 mm lens and (b) G1 lens

The 105 mm and 65 mm lens were used to provide a comparable measurement area for the 27 mm and G1 lens respectively. Figure 5.10 shows the speckle pattern collected using the two lenses. The scale factor was set with 0.022 mm/pixel for 105 mm lens and 0.0033 mm/pixel for 65 mm lens. Different interrogation cell (subset) sizes used for image correlation have been studied, and the cell size of 64 × 64 with 50 % overlap as

shown in the images (see the overlaid grid) was used. The specimen displacement across the face sheet/core interface obtained by DIC is shown in Figure 5.11. The vector arrows indicate the magnitude and direction of the displacement field. A large variation in displacement across the area of interest is clearly shown. The discontinuity in the displacement field necessitates the high resolution images provided by the white light camera.

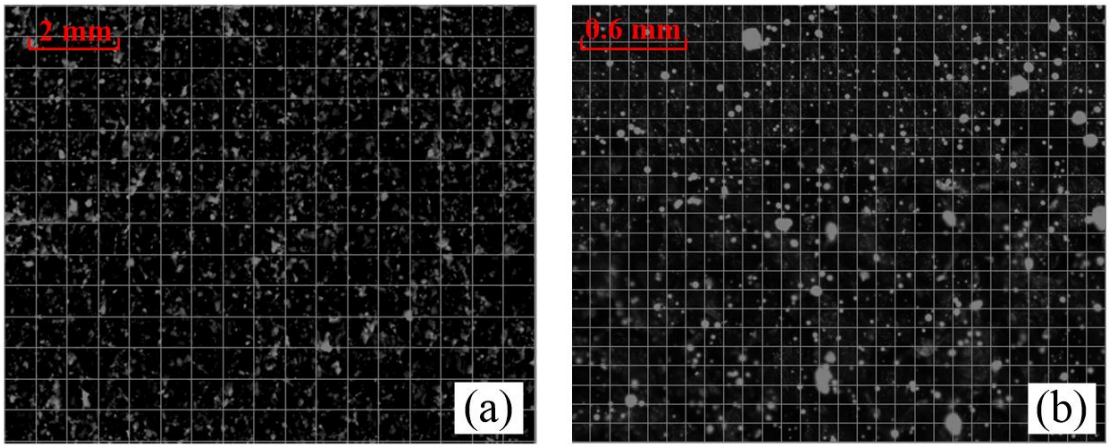

Figure 5.10: The black-white speckle pattern applied on the specimen surface and the applied interrogation cell: (a) 105 mm lens and (b) 65 mm lens

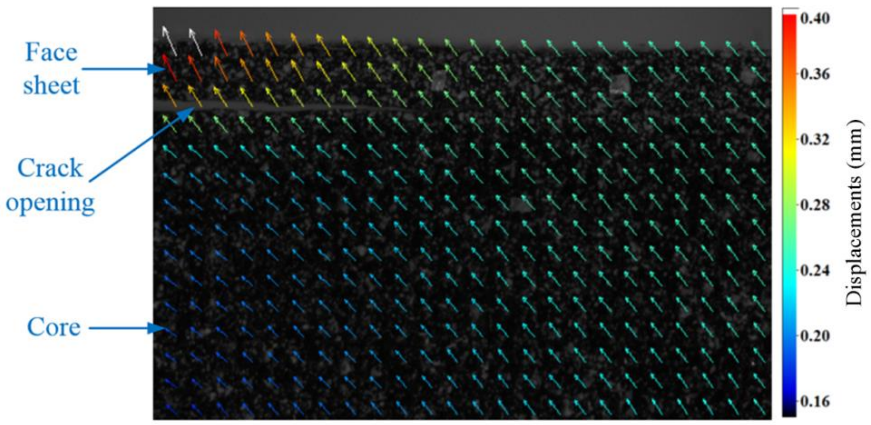

Figure 5.11: The displacement field around the crack tip obtained using DIC

5.4.3 TSA results

The TSA results obtained from the DCB sandwich specimen with and without applying the MC are presented and compared with the results obtained from FE analysis. The stress state obtained from the TSA is presented as a non-dimensional stress metric, $\Delta T/T$

(i.e. $\Delta\sigma \times K_T$), in this section. The results were adjusted for tension and compression by multiplying the amplitude data (ΔT) by +/- 1 in accordance with the phase data.

Figure 5.12 (a) shows the $\Delta T/T$ data before applying the MC method obtained from the 27 mm lens. At first glance, the data appears to be reasonable with the stress gradient showing in the debonded face sheet and a stress concentration at the crack tip. There is some indication of the edge effect at the debonded part of the upper face sheet and a kind of shadowing of the stress concentration. The only clear indication that motion may be affecting the data is the blurred position markers in comparison to what is observed in the stationary IR image in Figure 5.9 (a). The TSA results after applying the MC are shown in Figure 5.12 (b), by comparing the image in Figure 5.12 (b) with that of Figure 5.12 (a) the effect of motion on the TSA data becomes apparent. A clear through-thickness stress gradient from compression to tension can be observed in the debonded face sheet. The cellular structure of the foam clearly leads to small variations in the reflected radiation and hence a textured image; following the MC a clear $\Delta T/T$ gradient is observed in the foam. The localised increase in $\Delta T/T$ in the face sheet at the end of the debond region, i.e. the crack tip, is clear in Figure 5.12 (b).

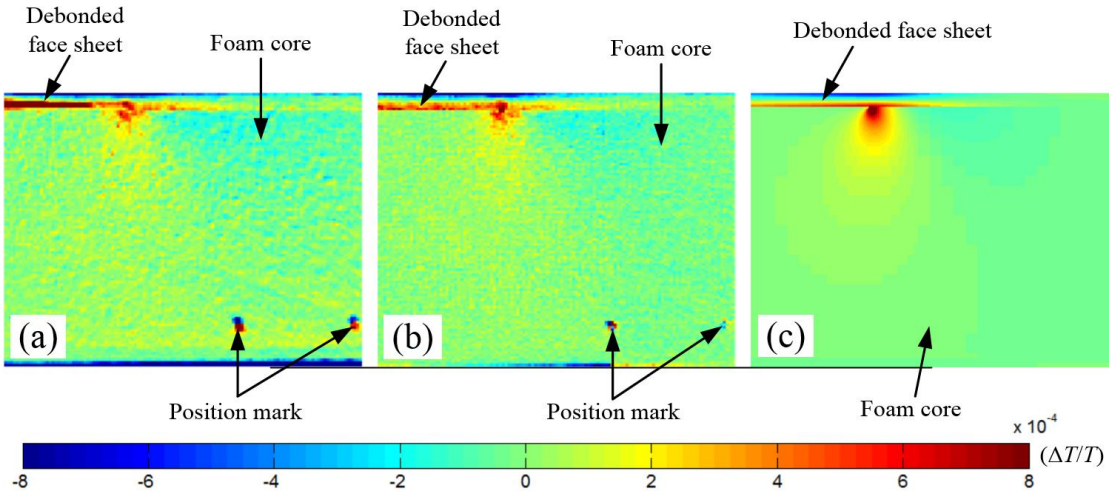

Figure 5.12: $\Delta T/T$ distribution obtained from TSA and FEA: (a) TSA without MC, (b) TSA with MC and (C) FE result

To compare the TSA results with the FEA, the thermoelastic constants of the face sheet and the core materials described in section 5.3 were applied to convert the stress data obtained from FEA to $\Delta T/T$ values. For the foam core material, the stresses along the x and y directions (σ_x and σ_y) were multiplied by the in-plane and through-thickness thermoelastic constants. Figure 5.12 (c) shows the $\Delta T/T$ distribution obtained from the FE results. There is good qualitative agreement between the FE and the TSA results after MC. To provide a quantitative comparison of the TSA and FE results, line plots of $\Delta T/T$ along

the x-direction, taken 1 mm below the interface crack in the foam, is shown in Figure 5.13. The TSA results after MC shows a good agreement with the FEA. A region of negative $\Delta T/T$ is present ahead of the crack tip which is introduced by bending of the upper face sheet. The $\Delta T/T$ values are slightly different to those predicted by FEA. This can be explained as the foam in the FE model is treated as a homogeneous material while the actual cellular structure of the foam results in a redistribution of the stress concentration in the vicinity of the crack tip.

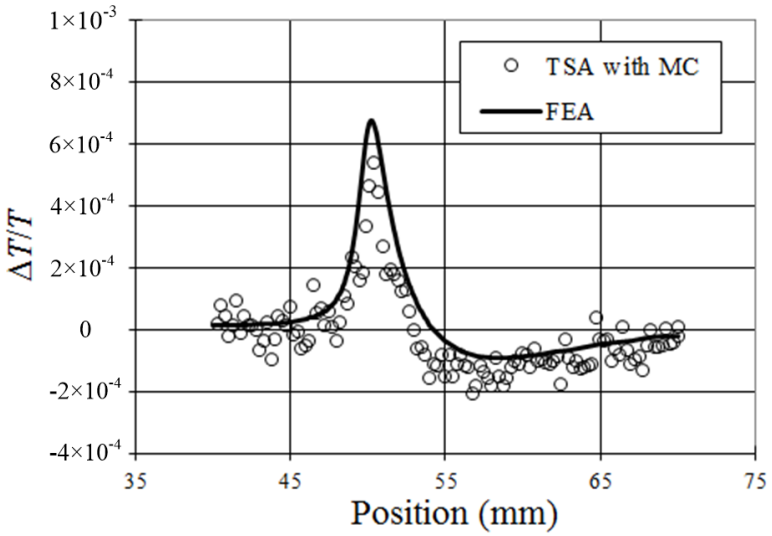

Figure 5.13: Line plot of the $\Delta T/T$ values obtained from TSA and FEA taken 1 mm below the interface.

$\Delta T/T$ results from the set-up with the G1 lens before and after MC are shown in Figure 5.14. The importance of compensating for specimen motion is highlighted even more clearly at these high spatial resolutions, as is evident by comparing the two images. In Figure 5.14 (a) the position marks appear twice as does the crack path. In Figure 5.14 (b) the through-thickness $\Delta T/T$ gradient from compression to tension in the upper face sheet is clearly identifiable, as is the stress concentration at the crack tip, both in the face sheet and the foam, including a small area but clearly identifiable area of compression in the foam. The textured nature of the foam is clear in $\Delta T/T$. The high spatial resolution data obtained from TSA allow small scale stresses that related to the meso-scale material structure to be investigated. This is important for studying the influence of the small features (e.g. localised and non-uniform stresses) in the vicinity of the crack tip on the crack propagation mechanism. Furthermore, the TSA result demonstrates the feasibility to study the interfacial fracture behaviour when crack arresting devices [18] are introduced at the face sheet/core interface where the complex material combinations at the interface require the local effects introduced by the crack arresting device to be investigated experimentally.

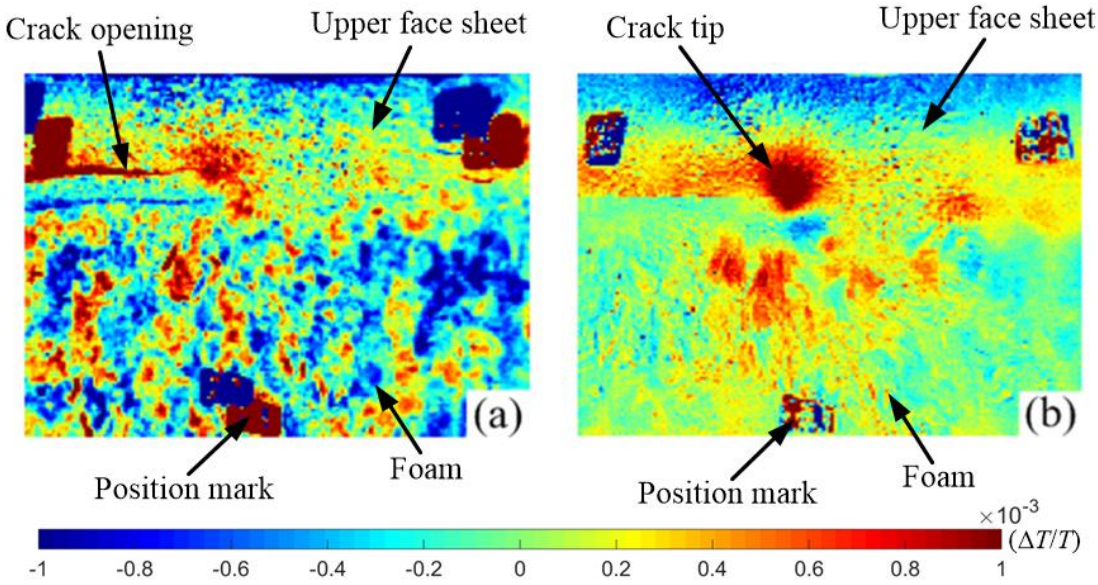

Figure 5.14: $\Delta T/T$ distribution obtained from TSA with the setup of G1 lens: (a) TSA without MC, (b) TSA with MC

5.5 Summary

The MC method developed in Chapter 4 has been applied to the DCB sandwich specimen for correcting the specimen motion for TSA. The thermoelastic constants for the composite face sheet and the foam core materials were obtained experimentally which enable the stress state in the vicinity of the crack tip to be obtained from the TSA data following application of the MC routine.

Chapter 6

A methodology for characterising the interfacial fracture toughness of sandwich structures

6.1 Introduction

In section 2.4.3 the test methods that can be used to characterise the mixed-mode interfacial fracture toughness were reviewed. Current approaches to obtain mixed-mode fracture toughness values are based on FE models with input from measurements. For specimens loaded using the MMB test methods, analytical solutions for the fracture toughness have been derived for isotropic face sheets only; these have shown good agreement with FEA. However, the derivation of generally valid analytical solutions for the fracture toughness for sandwich materials is generally complex and possibly elusive due to the complex loading configuration, anisotropic material properties and specimen geometry. Thus, no analytical solution has been developed for the TSD and DCB-UBM methods which can be used to examine the FE models, boundary conditions and solutions. This results in unreliable fracture toughness values obtained from these test methods. Accordingly, the work described in this chapter seeks to develop an experimental method for obtaining the fracture toughness of foam cored sandwich composites which can be applied to different specimen dimensions and loading configurations.

The approach is based on the use of IR thermography for capturing the temperature change developed at the crack front and relates it to the interfacial fracture toughness. Compared to traditional single point measurement sensors such as thermocouples, IR

thermography allows the surface temperature to be measured in a non-contact manner with high spatial and temporal resolutions. As the interfacial fracture toughness is derived directly from the measured temperature value, the method does not require knowledge of the global response of the test/rig/specimen and can be applied to different loading conditions.

A significant challenge associated with the temperature measurement is that, there is rapid heat dissipation at the newly created fracture surfaces as the crack front progresses. Furthermore the crack propagation can be very fast, especially in brittle materials, so a high frame rate is required to measure the temperature at the crack front. For example, it has been shown in [126] that the crack propagation velocity in PMMA materials can be higher than 200 m/s at loading rates of less than 0.5 mm/min. Thus, to capture the short-lived temperature increase during crack growth, IR thermography must be employed with very high frame rates. Therefore a key objective of the work is to demonstrate that the high speed IR thermography with 15 kHz frame rate can be used to capture the temperature evolution at the crack front during fracture, which again can be used directly for determining the interfacial fracture toughness for sandwich structures.

Firstly, the methodology and the experimental setup for obtaining the crack front temperature associated with crack growth are introduced. The feasibility of the methodology is then examined by obtaining the interfacial fracture toughness of sandwich structures loaded in the MMB test fixture. The MMB loading configuration was used because it is a well-established method which enables investigations of mixed mode interfacial crack propagation. Sandwich specimens containing cross-linked PVC foam core and E-glass/glass epoxy composite face sheet as descried in Chapter 5 are studied.

6.2 Methodology

Fracture in solids occurs when the potential energy stored at the crack tip is large enough to overcome the energy required to create new surfaces [43]. The fracture toughness, G_c, is a parameter that defines the required energy for an increment of crack extension in a unit area [45]:

$$G_c = -\frac{dW_s}{dA} \tag{6.1}$$

where W_s is the energy required to create new surfaces and A is the area of the crack increment.

During the fracture process part of the potential energy (stored during elastic deformation) is consumed by the plastic deformation at the crack tip, while the rest of the energy is dissipated as heat. According to the first law of thermodynamics, the work required to create new surfaces can be described as:

$$W_s = -(W_p + Q) \tag{6.2}$$

where W_p is the plastic work and Q is the heat released during fracture process.

For ductile materials, plastic deformation is induced ahead of the crack tip which results in almost all the potential energy being consumed by plastic work [127]. Previous work has shown the majority part of the plastic work is converted into heat, amounting to nearly 90 percent in metals [128] and 60 percent in polymers [129]. For brittle materials like glass and ceramics, the plastic deformation at the crack tip is negligible and almost all the potential energy is dissipated as heat released during the fracture process [43]. Figure 6.1 illustrates the generated heat at the crack front (the grey dashed line area) associated with a crack advance of length a. During fracture, heat is generated at the newly created crack surface (the area with length a and width b) as well as into the region below the crack surface with depth t according to the material thermal diffusivity. As two crack surfaces are created during the fracture process, heat is generated in two volumes (V_1 and V_2) and can be evaluated from:

$$Q = \rho C\left(\int_{V_1} \Gamma(V_1)\mathrm{d}V_1 + \int_{V_2} \Upsilon(V_2)\mathrm{d}V_2\right) \tag{6.3}$$

where ρ is the material density, C is the specific heat, and Γ and Υ are functions of temperature change related to the dimensions of the two crack volumes.

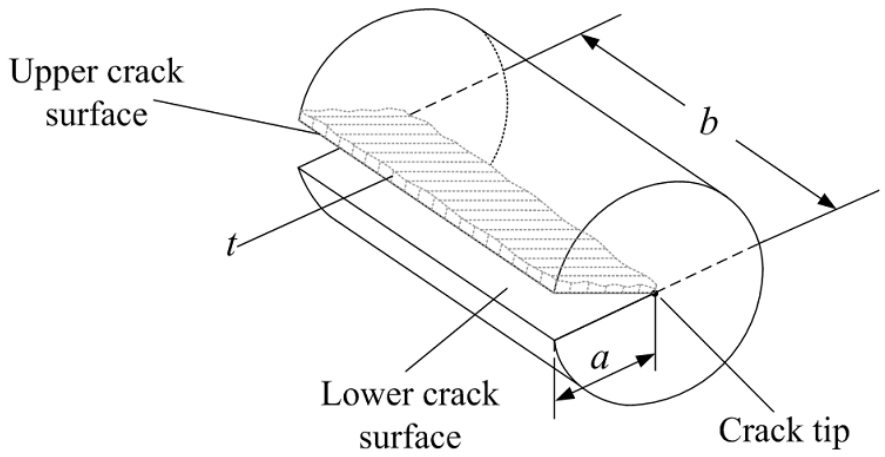

Figure 6.1: Temperature increase at the crack front during crack propagation

To simplify the expression in equation (6.3), the integral terms in the bracket are notated together as ΔT_V in the following treatment. By substituting equations (6.3) into equation (6.2) and then into equation (6.1), the fracture toughness can be related to the increase in temperature at the crack front as:

$$G_c = \frac{W_p + \rho C \Delta T_V}{2\Delta A} \tag{6.4}$$

As described above, when considering the fracture in brittle or semi-brittle materials two assumptions can be made: 1) the plastic deformation at the crack tip is highly localised and very small; 2) the heat generated in the area below the crack surface is small and negligible. Since the foam core material considered in this investigation is a cross-linked PVC foam which is generally considered as brittle [130, 131], the two assumptions stated above can be adopted. Accordingly, it is possible to reduce equation (6.4) so that the material fracture toughness can be expressed through the following proportionality:

$$G_c = \psi \frac{\Delta T_S}{\Delta A} = \psi \frac{\Delta T_S}{a \times b} \tag{6.5}$$

where ΔT_S is the integral of temperature over the two crack surfaces and ψ is a constant of proportionality with units of J $K^{-1}m^{-3}$.

It can be seen that equation (6.5) provides a simple linear relationship between fracture toughness and temperature, without recourse to knowledge of the applied load or displacement in a test. Accordingly, by experimentally determining ψ for different materials, it is possible to derive the material fracture toughness simply from a direct temperature measurement in any loading configuration. The shortcoming is that to determine ψ, G_c must be known for given interfacial materials. It is proposed that G_c is determined from a validated FE model (or analytical model if available) for a well-defined test configuration and used in equation (6.5) to obtain ψ. Once ψ is known for given interfacial materials then the temperature measurement alone can be used to determine G_c for any test configuration and mode-mixity.

The possibility of using equation (6.5) to determine the fracture toughness was studied by measuring the temperature change at the crack tip of the face sheet/core interface of a sandwich specimen. Figure 6.2 shows the experimental methodology that was devised to obtain the temperature change per unit area, i.e. $\Delta T_S / \Delta A$ in equation (6.5). The adopted experimental procedure is as follows:

1. The sandwich structure (specimen) that contains an initial debond is loaded statically until a pre-manufactured debond starts to propagate.

2. An IR detector captures the temperature change associated with crack growth across the entire crack front.
3. A high speed camera is used to capture the crack advance by taking white light images from the side of the specimen. Thus, the crack increment area (ΔA in equation (6.5)) can be obtained by multiplying the crack advance a by the specimen width b.
4. The load and displacement data from the test machine are collected and analysed in real-time using a LabView program. When the load starts to decrease the program sends a trigger signal to both IR and high speed cameras to initiate data capture.
5. The cameras are set up in pre-trigger mode and are continuously capturing data. When the trigger signal is received IR images captured within 6 seconds before and after crack propagation are recorded.

6.3 Temperature measurement

In Chapter 3 the use of the IR camera for temperature measurement has been described. It has been shown that the conversion of the detector DL into temperatures normally requires two steps: the temperature calibration of the detector array and the determination of the surface emissivity of the objects. Since the standard temperature calibration curves provided by the manufacturer are not valid for the frame rates in the kHz region, a bespoke calibration process for high speed thermography developed in [24] was described in section 3.3 which enables a quantitative temperature measurement at high frame rates.

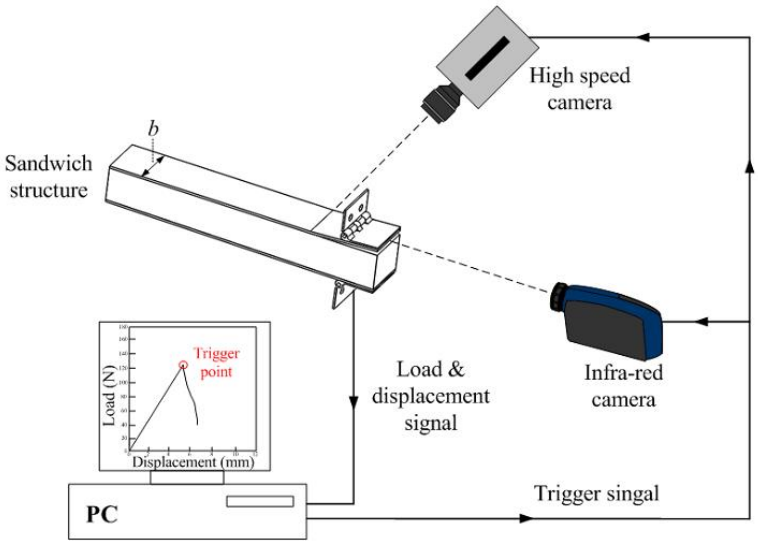

Figure 6.2: Test setup for measuring temperature change per unit area at the crack surface

In [24] the calibration approach has been experimentally validated using the same IR camera system as used in this work. Thus, the developed calibration approach for high speed thermography was adopted in this work.

When estimating the surface emissivity at the crack surfaces, it is possible to treat the crack surface area as a V-groove cavity as shown in Figure 6.3 (a), where δ and a represent the crack opening distance and the crack increment, respectively. Thus, the effective emissivity (e_0) of the cavity can be estimated as follows [132]:

$$e_0 = \frac{e[1+(1-e)(\frac{\delta}{\delta+2a} - \sin^2(\frac{\phi}{2}))]}{e(1-\frac{\delta}{\delta+2a}) + \frac{\delta}{\delta+2a}} \tag{6.6}$$

where e is the surface emissivity of the cavity material, and ϕ is the vertex angle of the groove. Figure 6.3 (b) plots the effective emissivity against the material surface emissivity values for different δ/a values (with ϕ calculated correspondingly by the law of cosines).

From the experimental results conducted in this work, a δ/a value of about ¼ was commonly observed for all the test specimens (estimated from the dimensional data collected in the white light images). As shown in Figure 6.3 (b), for the composite and PVC foam materials used in this work, it is reasonable to assume that the apparent emissivity at the crack surface is close to that of the blackbody with the value of 1.

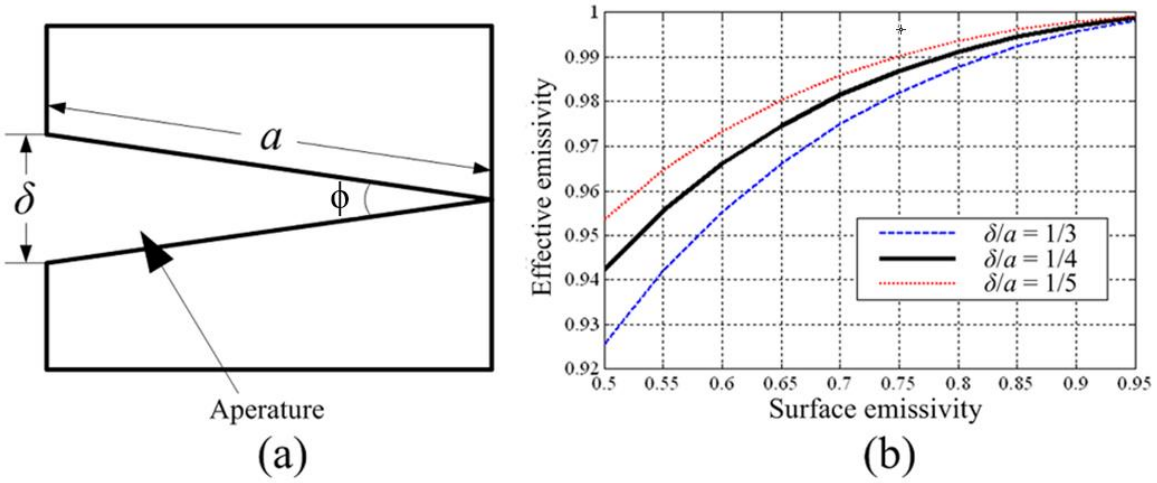

Figure 6.3: (a) V-groove cavity geometry with: crack opening distance δ, vertex angle ϕ and crack increment a; (b) Cross-linked PVC foam core material: effective emissivity vs. material surface emissivity values for different δ/a values.

6.4 Experimental arrangements

6.4.1 Test specimens and materials

The constituent materials and manufacturing process of the sandwich specimens are kept constant as those used in Chapter 5. Sandwich specimens were tested using the MMB test rig shown in Figure 6.4. The rig was loaded by a downward force, P, introduced through the loading yoke, and transferred to the beam specimen via roller and steel hinges. Hinges were bonded on the specimens using an Araldite^{TM} epoxy resin cured for 12 hours at room temperature. The MMB rig allows variation of the loading conditions between mode I (tensile normal) and mode II (sliding shear) mainly by changing the lever arm distance, c, and the core thickness, t_c [62]. For instance, mode I dominated loading can be applied at the crack tip by using a large lever arm distance and a high core thickness. The increase of the face sheet thickness (t_f) or decrease of the span length (L) also promotes a mode I dominated loading.

The constant of proportionality, ψ, given in equation (5) was obtained under different loading modes by changing the constituent material dimensions and loading configurations to develop different G_c values for each specimen. A summary of the dimensions and loading conditions of the test specimens is shown in Table 6.1. The specimen has a span length ($2L$) of 150 mm. The specimen dimensions and initial crack length are average values taken from 5 measurements; in all cases the standard deviation (SD) was less than 0.033 mm. Furthermore, the applied loading modes also influence the crack propagation path (e.g. the crack can propagate either in the core, face sheet or at the face sheet/core interface) [63, 133]. The aim is that the test specimens generate different crack propagation paths to allow different interfacial conditions to be evaluated.

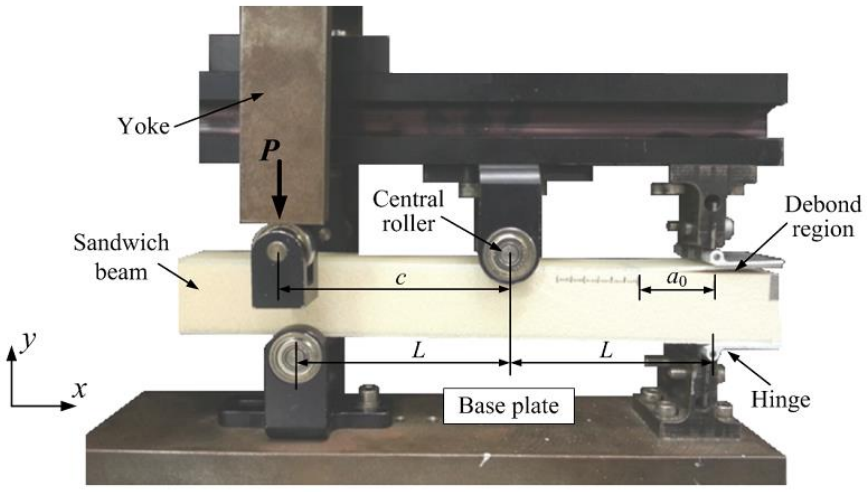

Figure 6.4: Sandwich beam specimen with initial debond loaded in the MMB test rig

Table 6.1. The dimensions (units: mm) and loading conditions of different test specimens (SD not included as they were less than 0.033 mm in all cases)

	S1	S2	S3	S4	S5	S6	S7	S8	S9	S10	S11
t_f	1.68	1.69	1.70	1.70	1.87	1.91	1.51	1.52	1.50	1.51	1.49
t_c	25	25	25	25	15	15	15	15	15	15	15
b	28.83	31.30	31.27	30.02	30.09	30.09	29.58	29.47	29.60	29.52	29.68
a_0	28.12	27.48	23.51	28.50	26.03	26.44	24.47	25.21	23.30	26.89	24.61
c	65	50	50	50	45	45	40	40	55	55	55

6.4.2 Experimental setup

Sandwich specimens mounted in the MMB rig were tested in an Instron ElectroPuls machine (E1000) with a 1kN actuator and load cell capacity. The load cell is calibrated by the manufacturer and has a quoted accuracy of ± 0.5% [134]. The actuator/load cell was connected to the loading yoke and a compressive load was applied to the MMB test fixture. The specimens were loaded at a rate of 1 mm/min.

The crack front of the specimen viewed by the IR camera is shown in Figure 6.5. The reduced detector array at 15 kHz results in a small field of view which is indicated by the yellow rectangular area in the middle of the image. To enable the temperature measurement across the entire crack front, the small field of view must be positioned properly. As indicated in the image, for the measurement of each specimen, the detector focal length is adjusted to allow the length of the rectangular area to be the same as the width of the specimen and the rectangle is positioned just above the foam core. This arrangement enables the crack front temperature to be measured with maximum spatial resolution. The metal tape shown in the image is bonded to the foam core surface to highlight the edge of the core and the area of the crack front. Before the measurements, the IR camera is rotated 15 degrees down relative to the horizontal plane so that the upper and lower crack surfaces at the crack front can be observed. Together with the IR images, the corresponding load data output from the test machine is recorded by the IR camera system at 15 kHz, hence the collected load data has the units of DL.

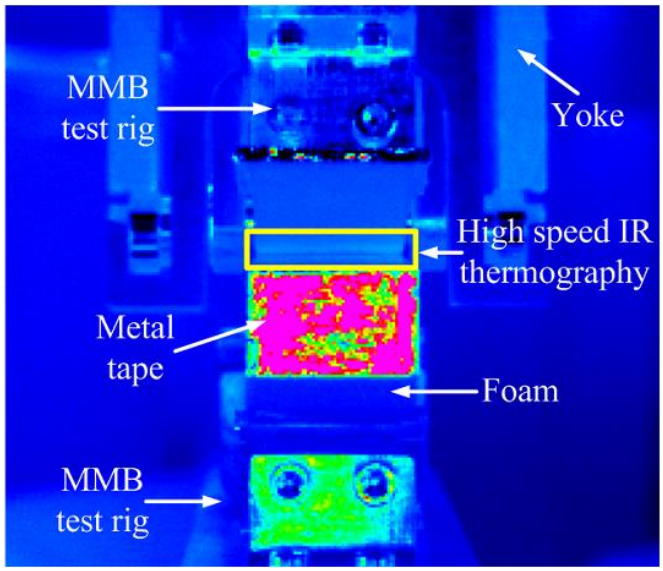

Figure 6.5: Crack front viewed by the IR detector and the field of view (yellow rectangle) at 15 kHz frame rate

To obtain the crack increment area (ΔA), the crack advance is measured using a Photron SA-3 high speed camera with a frame rate of 5 kHz. A lower frame rate is acceptable for the high speed camera than for the IR camera because the crack length was determined from two stationary points between the initial crack tip and the crack tip after fracture. The white light images obtained from the high speed camera were calibrated using a pre-applied scale of 15 mm on the specimen surface. To determine the number of pixels over the 15 mm scale, the measurements were taken five times and an average value from these measurements was used for calibrating the image spatial resolution. The image resolutions were approximately 0.026 mm with a SD smaller than 1.414×10^{-4} mm. As the recording capacity of the IR and high speed cameras are limited (only images captured within 6 seconds can be saved in the memory), a LabView code was designed to trigger image capture of both cameras when the crack propagated. Both cameras were setup so that an equal number of images recorded before and after the triggering were saved to the memory.

The LabView code acquired the load and cross head displacement from the test machine using a NI USB-6211 analogue to digital data acquisition system with a sampling rate of 10 Hz. When the crack starts to initiate there is a sudden decrease in the applied load as shown in Figure 6.6 (a). However, due to the electronic noise, there is not a monotonic increase in the load signal during the initial loading (see the red zoomed insert in Figure 6.6 (a)). Therefore simply using a reduction in the load signal as a trigger is not appropriate; instead the loading rate is used as the trigger to capture data. Figure 6.6 (b), shows the loading rate can be obtained by performing a linear fit of a straight line over '*n*' number of data points. This means that the crack initiation is identified when the loading

rate becomes negative. It is clear that the accurate measurement of the loading rate depends on the choice of the integer '*n*'. If *n* is too small the true trend of the load-displacement curve is not captured. Also if *n* is too large, identification of the crack initiation will be inaccurate. Therefore '*n*' was determined from the load-displacement curve of a pre-tested specimen in which linear fitting was applied using different values of *n* from 5 to 50. When *n* was chosen to be smaller than 10, the derived loading rates did not capture the true load-displacement behaviour of the specimen, because the loading rates were recorded randomly as positive and negative due to the electronic noise. As *n* was incremented in steps of 10 from 10 to 50, it was shown that for $n = 20$ and above the turning point of the load displacement curve happened at the same data point. Therefore it was concluded that using a value *n* of 20 provided the most effective identification of the crack initiation.

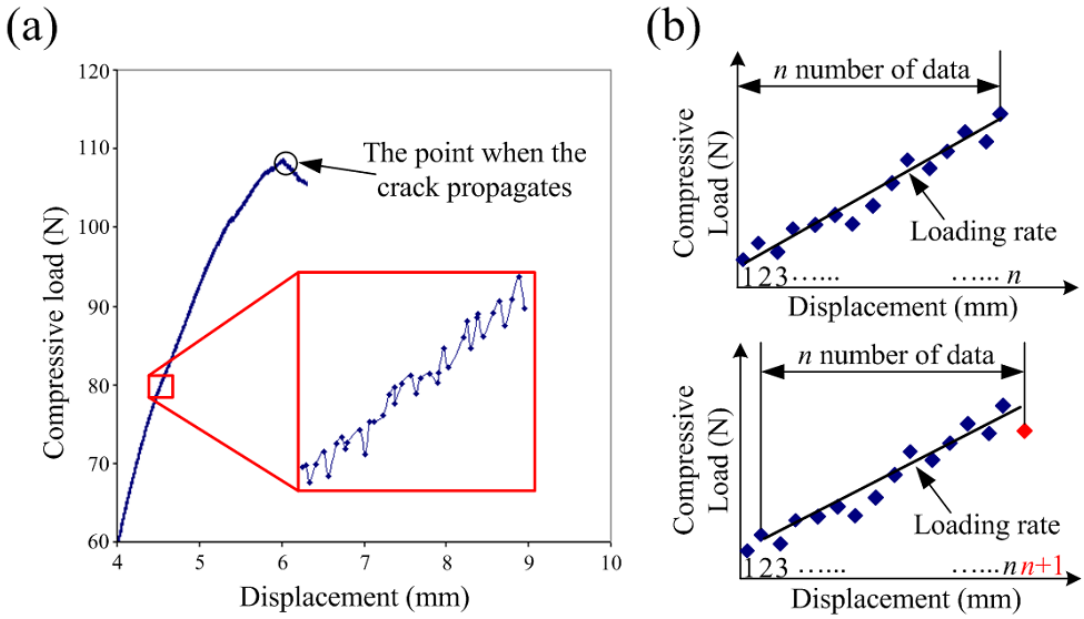

Figure 6.6: (a) Load-displacement data collected from LabView code; (b) Derivation of the loading rate.

6.5 FE analysis

FE analysis was performed to extract the values of the interfacial fracture toughness and the crack tip loading mode-mixity (i.e. the relative amount of mode I and mode II stresses applied at the crack tip) for different specimens. As described by the FE analysis of the MMB specimen in [62], the interfacial fracture toughness G_c and the mode-mixity φ were derived from equations (2.9) and (2.10) using the CSDE method as described in section 2.4.1. The values of δ_y and δ_x in equations (2.9) and (2.10) were directly extracted from

the crack node displacements of the FE model using the loading condition that the critical load (P_c) at the onset of crack propagation was applied.

2D FE models of the specimens loaded in the MMB test rig were developed in the commercial FE package ANSYS 12.1. The geometry of the model with the applied boundary conditions is shown in Figure 6.7. The MMB loading arrangements were obtained from the static beam analysis [62]. The model uses an 8-node 2D plane strain elements (PLANE 183). A highly refined mesh with a minimum element size of 0.01 mm was used at the crack tip to accurately capture the crack tip displacements.

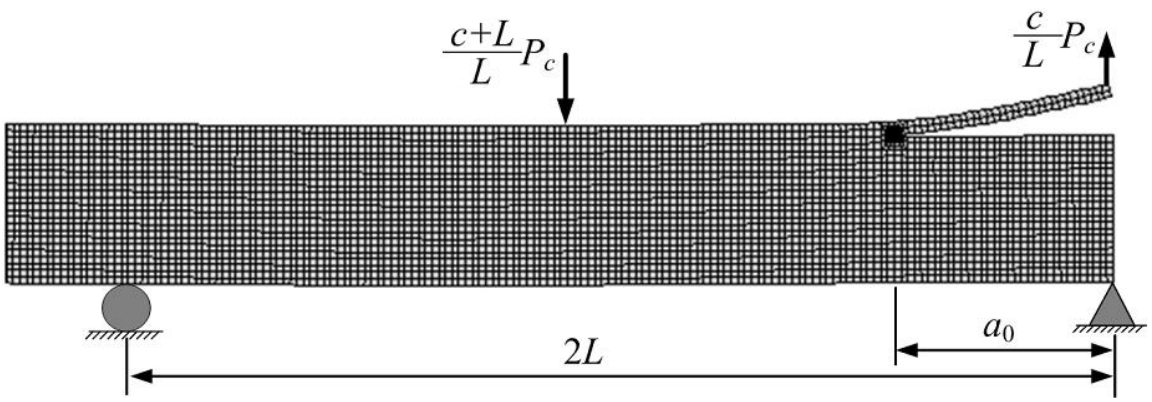

Figure 6.7: FE model of the specimens loaded under the MMB loading conditions

6.6 Fracture test results

Specimens with different loading conditions given in Table 6.1 were tested. The critical load (P_c) for crack propagation and the crack propagation paths observed form the fracture tests are summarized in Table 6.2. For each specimen, the applied crack tip mode-mixity φ and the interfacial fracture toughness G_c were calculated from the FE models.

Two different crack propagation paths were observed. When the specimen was subjected to a mode I dominated loading (small magnitude of φ), the crack propagated in the foam core just below the face sheet/core interface. As φ increases the crack tended to propagate at the face sheet/core interface. This can be attributed to the increased negative shear stresses acting at the crack tip that forces the crack to propagate along the interface. The observed crack propagation paths for the different loading mode-mixities agree well with results reported in [63].

Table 6.2. Fracture test results for different specimens

Specimens	P_c (N)	Crack propagation path	φ_F (°)	G_c (J/m^2)
S1	106.2	Core	-18.16	796.2
S2	159.8	Core	-19.15	886.2
S3	178.7	Core	-19.08	861.2
S4	151.3	Core	-19.72	912.7
S5	188.1	Core	-25.19	657.9
S6	200.8	Core	-25.82	763.2
S7	134.2	Interface	-24.45	519.1
S8	163.7	Interface	-25.38	801.1
S9	112.3	Interface	-21.58	622.0
S10	103.9	Interface	-22.34	688.2
S11	110.2	Interface	-21.92	655.2

When the crack propagation path is at the bi-material interface, the crack surface may contain different material constituents, and this makes the proportionality between G_c and temperature change, defined as ψ in equation (6.5), questionable. The constituents on the fracture surface from both sides of the interface were inspected post-mortem. Figure 6.8 shows microscopic images of the fracture surfaces that indicates an interfacial crack propagation path. The fracture surface on the face sheet side shows a resin surface texture without any foam attached. For the fracture surface on the core side, open foam cells (see Figure 6.8 (c)) can be observed. These are (at least partially) covered by a resin layer, which indicates that the interfacial crack was propagating along the resin layer between the face sheet and core. Thus it is theorized that equation (6.5) is valid also for the specimens displaying interfacial crack propagation paths.

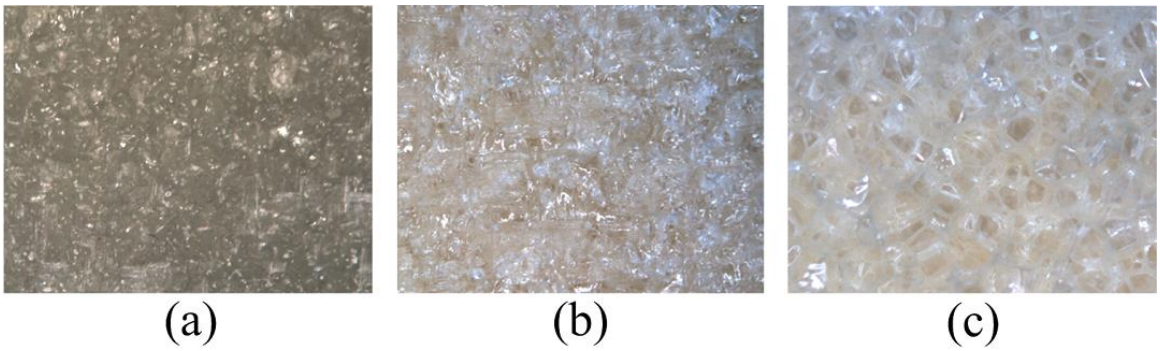

Figure 6.8: (a) Crack surface on the face sheet side, (b) crack surface on the core side, (c) surface texture of the foam

6.7 Characterization of interfacial fracture toughness

6.7.1 Temperature field associated with crack propagation

The temperature change associated with the crack growth was studied by correlating the thermal data captured at the crack front with the load signal. Figure 6.9 plots the average temperature value taken across the crack front (i.e. the yellow rectangular area in Figure 6.5) obtained from two specimens (S3 and S11) with different crack propagation paths. The corresponding load trace in DL shown in the plots was collected simultaneously with the temperature by directly connecting the analogue output of the test machine to the IR camera system and recording alongside the IR output. As a specimen was loaded under displacement control, the decrease of the compressive load shown in the plots indicates that the crack started to propagate. From the temperature trace obtained from different crack propagation paths, an increase of the average temperature value can be observed at the time when the compressive load starts to decrease. This clearly indicated that the increase of the temperature at the crack front was caused by the energy release associated with the crack growth. In both plots, the average temperature values observed before the

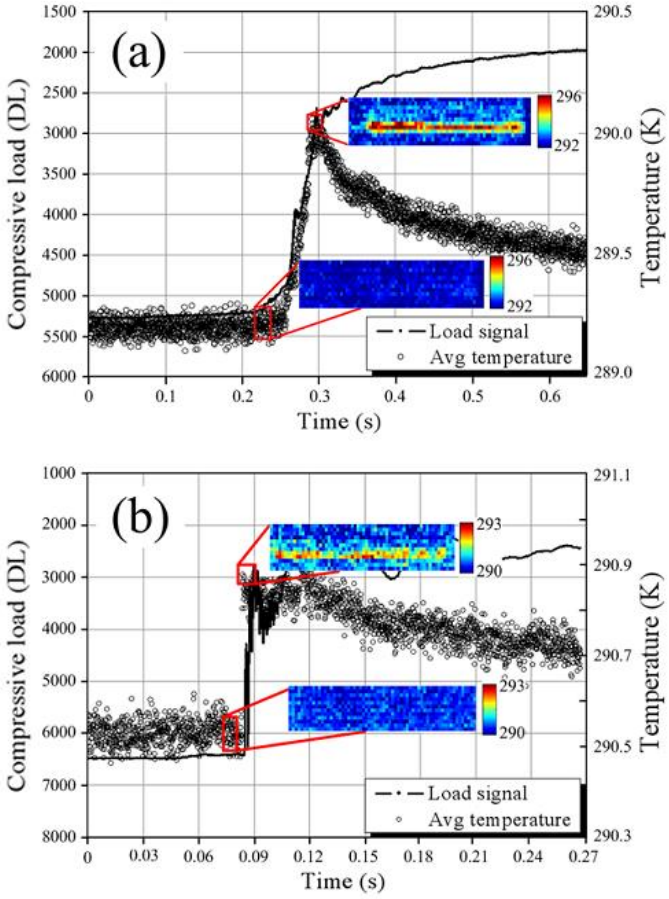

Figure 6.9: Load and average temperature trace obtained from specimens with (a) crack propagation path in the core, and (b) crack propagation path at the face/core interface

crack propagation vary within the range about 0.1°C which can be attributed to the detector noise. As some heat must be dissipated during plastic deformation, and as there is little or no increase in temperature prior to the crack initiation, the temperature trace in Figure 6.9 provides the evidence that the plastic deformation at the crack tip is very small. Hence the assumption of negligible plastic deformations made in deriving equation (5) is confirmed. A close-up of the average temperature value shown in Figure 6.9 is plotted in Figure 6.10 from which it is observed that a large number of data points were collected close to the maximum average temperature value before the temperature started to decrease. This indicates that the 15 kHz frame rate used in this work was capable of capturing the temperature increment before the heat dissipated. In Figure 6.10 (b) the sudden change in the average temperature trace indicates that the crack was propagating very fast. Here only 2 data points were sampled before the average temperature reached the maximum value (see the small window in Figure 6.10 (b)). Thus demonstrating the necessity for high speed IR image capture to obtain the crack front temperature trace.

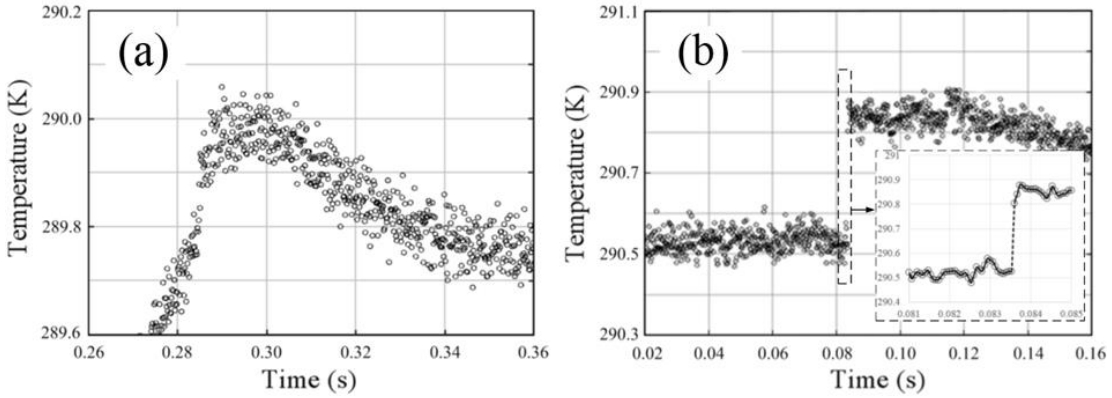

Figure 6.10: Close-up of the average temperature trace with: (a) corresponding to Figure 10 (a) and (b) corresponding to Figure 10 (b)

In Figure 6.9 thermal images before and after crack propagation are plotted. The red rectangular temperature maps shown in each plot represent the following: the thermal image before crack propagation was obtained as the average of 100 thermal images collected just before the crack growth, and the thermal image at the time when the average temperature reaches the maximum value showing the crack front temperature after crack growth. The thermal images show a clear temperature increase at the crack front immediately after the crack propagation has occurred. The temperature difference between the two thermal images before and after crack propagation gives the temperature change image (ΔT image) from which the overall temperature increase at the crack front (i.e. ΔT_S in equation (5)) can be obtained. Figure 6.11 shows examples of the ΔT images obtained from the specimens with the crack propagation path occurring within the core. Thus, the overall temperature increase collected at the crack front (ΔT_S) can be obtained as the sum of the ΔT values in the image.

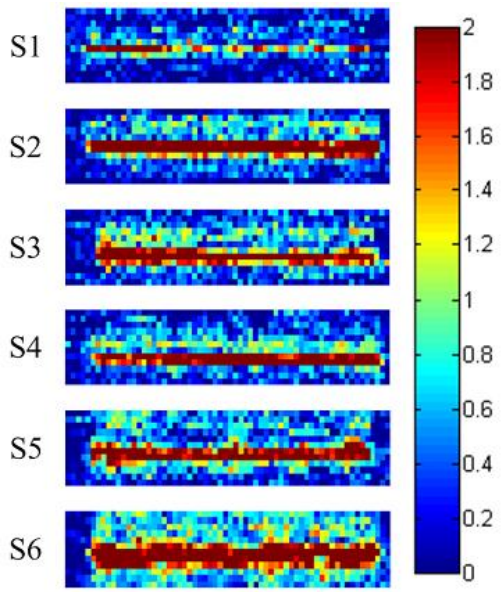

Figure 6.11: ΔT images obtained from specimens with the crack propagation path in the core

6.7.2 Determination of interfacial fracture toughness

In Figure 6.11 the temperature increase obtained in specimen S1 is seen to be relatively small compared to those obtained in the other specimens. It has been described in section 3.3 that the IR detector provides a thermal resolution (detector noise) about 0.3 °C at 15 kHz. This means that the detector noise may influence the accuracy of the ΔT value when the temperature/detector output is small. For specimen S1 the ΔT values were mostly in the range from 0 to 0.6 °C, which is close to the detector noise level. Therefore, the accuracy of the ΔT value can be largely influenced by the noise introduced during the measurements. To demonstrate the influence of the noise on the temperature change value obtained at the crack front, a threshold with values from 0 to 0.3 °C was applied to the ΔT images. This means that when the threshold is set to 0.1, ΔT values smaller than 0.1 are set to zero.

Figure 6.12 plots the $\Delta T_S/\Delta A$ values derived from different thresholds against the fracture toughness values for specimens S1-S6. It is shown that, with an increase of the threshold from 0 to 0.3, the $\Delta T_S/\Delta A$ value for specimen S1 decreases significantly, while there is little changes of the $\Delta T_S/\Delta A$ value obtained from other specimens. A similar investigation was also applied to the specimens where an interfacial crack propagation path was observed, and the results obtained were almost identical. Based on the analysis, it is shown that the influence of the detector noise to the ΔT_S value can be minimised for the current test by applying a temperature threshold of 0.3°C to the ΔT image.

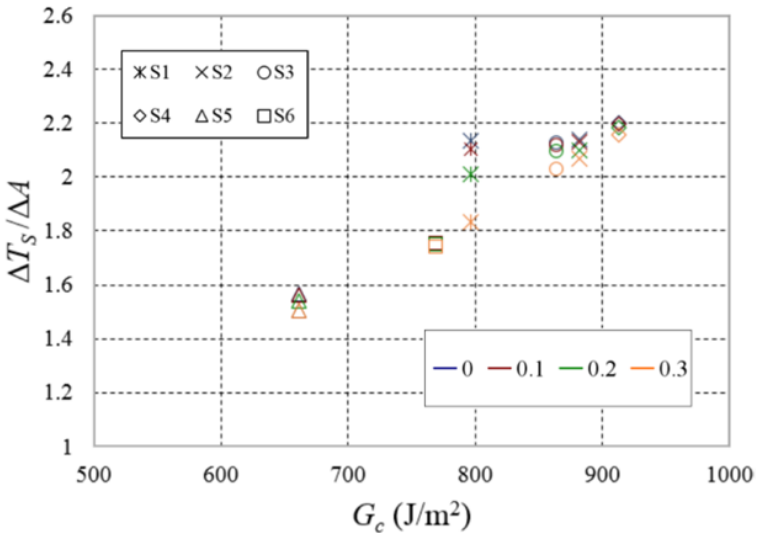

Figure 6.12: ΔT_s /ΔA against the fracture toughness obtained from different threshold values (0, 0.1, 0.2 and 0.3) for specimens with crack paths within the foam.

Figure 6.13 plots the fracture toughness determined for each specimen against the $\Delta T_S/\Delta A$ values using the 0.3°C temperature threshold. For specimens with different crack propagation paths, the results were plotted separately as the crack surface has different material properties. For each specimen, the relationship between the $\Delta T_S/\Delta A$ and G_c determines the constant of proportionality ψ described in equation (5). The vertical error bars indicate the measurement errors that might be introduced during the tests in determining G_c. The errors considered here include those generated as a result of the measurement errors of the specimen dimensions and crack lengths as well as the accuracy of the load cell readings. Accordingly, the range of the errors for G_c shown in Figure 6.13 was calculated based on the SD of the measurements and the accuracy of the load cell readings. The errors that might be introduced in the $\Delta T_S/\Delta A$ calculation include the calibration of the high speed images, the estimation of the crack tip location and the measurement of the specimen width. From the high speed images, the crack tip location was estimated to be within one pixel resolution i.e. 0.026 mm. The SD of the calibrated pixel resolution is smaller than 1.414×10^{-4} mm. Thus, the horizontal error bars shown in Figure 6.13 indicate the error in obtaining the crack progression and the SD of the specimen width measurements.

By linear fitting of the data points obtained from the specimens in each plot, a straight line can be obtained which shows that the values of ψ obtained from the same crack surface materials are identical, even though the mode-mixities are different. For the crack surface studied in this work, two values of ψ were determined, one representing crack propagation in the PVC core material, ψ = 401.27 J $K^{-1}m^{-3}$, and one corresponding to face

sheet/core crack propagation, ψ = 611.53 J $K^{-1}m^{-3}$. As specimens were tested with different dimensions (e.g. the face sheet and core thickness) and loading conditions between mode I and mode II, it is shown that the influences of the specimen dimensions and loading conditions on ψ are insignificant. This is expected as ψ directly relates the heat generated at the crack surface with the fracture energy. Thus, the values of ψ obtained in the results can be used to determine the fracture toughness in different loading configurations when the fracture surface contains the same materials as those studied in this work.

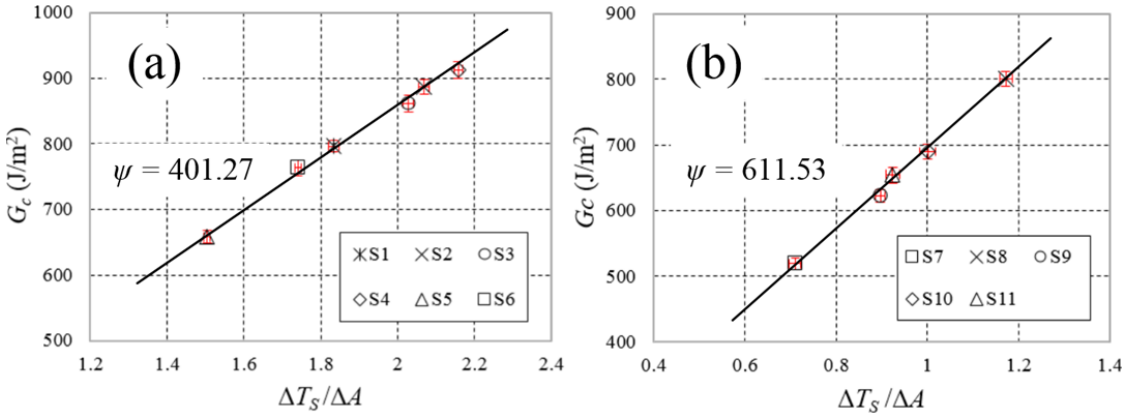

Figure 6.13: $\Delta T_s/\Delta A$ against fracture toughness for specimens with (a) cracks paths in the core, and (b) crack paths along the face sheet/core interface.

6.8 Summary

A methodology has been developed for capturing the temperature increase at a propagating crack using high speed IR thermography. It has been shown that the IR thermography with 15 kHz frame rate was capable of a quantitative measurement of the crack front temperature associated with the crack growth.

It has been proposed that by measuring the temperature alone the interfacial fracture toughness in foam cored sandwich structures can be determined. It is demonstrated that for given sandwich constituent materials, a constant of proportionality ψ can be derived between the measured temperature change per unit area ($\Delta T_S/\Delta A$) and G_c provided by an FE model for different interfaces. Once ψ is obtained from a known loading configuration it can then be used together with the temperature change per unit area ($\Delta T_S/\Delta A$) measured from any loading configuration to give the interfacial fracture toughness for a particular interface.

An initial demonstration of the method is provided for sandwich specimens with a cross-linked PVC H100 foam core and E-glass/epoxy face sheets. Specimens with an initial debond were loaded in a MMB test configuration subjected to different loading mode-mixities. Two different crack propagation paths were observed during the tests: 1) a debond growing in the core material just below the interface, and 2) a debond propagating along the face sheet/core interface. For both crack propagation paths, an increase of the temperature at the crack front associated with the crack growth was captured by the IR camera. For each specimen, the values of ψ were obtained from the relationship between the measured $\Delta T_S/\Delta A$ value and the known fracture toughness G_c obtained from the validated FE model. It was shown that ψ obtained from the specimens with the same crack propagation path was identical. Also, ψ was not influenced by change of the specimen dimensions and loading conditions. Thus, it has been demonstrated that by determining the values of ψ, the fracture toughness can be determined in any test configurations by a direct temperature measurement. Further work is required to fully validate this proposition but the work described in this chapter provides an important first step to show that the temperature measurement is possible and indeed feasible with high speed IR imaging, and further that the measured temperature change per unit area ($\Delta T_S/\Delta A$) can be linked directly to the fracture toughness G_c through a simple linear relationship.

Chapter 7

Static testing of crack arresting devices in sandwich structures

7.1 Introduction

In Chapter 2 the crack arresting approaches developed for foam cored sandwich structures have been discussed. The peel stopper has been demonstrated as an effective method that has the capability to arrest the propagation of debond damage in sandwich beams. It has been shown that the efficiency of the peel stopper is mainly dependent on crack deflection at the tri-material junction of the face sheet, core and the peel stopper [72, 73]. Although previous studies [72-74] have shown that the peel stopper can deflect the interfacial crack in sandwich structure beams loaded in three-point bending, the knowledge about the crack path at the tri-material junction under different loading conditions has not been studied in detail. Thus, the work presented in this chapter investigates the crack propagation mechanism at the tri-material junction under mode I dominated loading.

To facilitate the crack deflection at the tri-material junction, modifications of the peel stopper configuration are proposed and their effect on the ability to deflect the interfacial crack under static loading is examined. The second aim of this chapter is to validate the FE models (developed by PhD student Georgios Martakos, Aalborg University, Denmark) of different peel stopper configurations using the static testing results. The models are used for providing an energy release rate control approach of the fatigue testing performed in Chapter 8. The energy release rate amplitude is controlled in the fatigue test by adjusting the displacement amplitude (predicted by the FE model) applied by the test machine. This allows the crack to propagate in a stable manner during the fatigue test.

Initial tests were carried out on the original peel stopper design described in [18]. It is. shown that this peel stopper is ineffective under mode 1 dominated loading. Modifications of the peel stopper are suggested in the form of three different configurations that provide different conditions at the tri-material junction. A description of the design and manufacture of the sandwich structure specimens that incorporate the three new peel stopper configurations is provided. The FE models of the different sandwich specimens developed by Georgios Martakos are described, so that they can be validated by the experimental work which is part of this PhD project. Finally, the crack paths from the different configurations of the peel stopper observed in static tests are presented. It is shown that a change of small material features at the tri-material junction enables the crack to be deflected more effectively. The FE models are validated using load-displacement data obtained from the static tests. Thus enabling the displacements used in the in the fatigue tests described in Chapter 8 to be defined.

7.2 Initial investigations of the peel stopper

The peel stopper has the same constituent PU materials (a two-component PERMAlock 40496 polyurethane adhesive) and geometries as those described by Jakobsen *et al*. [18]. The peel stopper was embedded in a sandwich beam specimen as shown in Figure 7.1 (a) (an initial debond was created during the manufacturing of the panel as described in chapter 6). A detailed description of the sandwich specimen and the manufacturing process are described in section 7.4. To enhance the bonding between the peel stopper and the face sheet material, the surface of the peel stopper was roughened using emery paper prior to installing in the sandwich structure specimen. The specimen was loaded using the MMB test rig with a long lever arm distance of 60 mm (the span length is 160 mm) to provide a mode I dominated loading condition.

The initial tests were conducted using four specimens. In three specimens the crack path was not deflected at the tri-material junction as shown in Figure 7.1 (b). Here the crack is not deflected into the core unlike in the three-point bending tests in [18]. It is noted that the crack propagated along the face sheet/core interface when it reached the tri-material junction and the crack tip was located above a thin resin layer on the surface of the foam (indicated in Figure 7.1 (b)). However, in the three-point bending tests, the interfacial crack was initiated by core shear failure and the crack tip at the tri-material junction was below the resin layer in the foam. The thin resin layer may impede the crack deflection at the tri-material junction and the difference in the crack tip locations could be a reason that explains the different crack paths for the two loading configurations. To investigate the influence of the crack tip location on the crack path, two sandwich specimens were

manufactured without the initial debond. Instead a crack was introduced in the foam just below the interface using a thin blade. This allows the crack to propagate below the resin layer at the tri-material junction. However, the results show that the crack kinked back towards to the interface at the tri-material junction and was not deflected. This shows that the crack path is not influenced by the crack tip location.

The initial test results show that the crack cannot be effectively deflected by the peel stopper under mode I dominated loading. The mechanisms that determine the crack path at the tri-material junction must be established. Thus, it is necessary to identify the local effects at the tri-material junction that determine the crack path and propose a more effective design of the peel stopper. In the next section, the design modifications of the peel stopper (e.g. the peel stopper geometry and the configurations at the tri-material junction) proposed in this work are described.

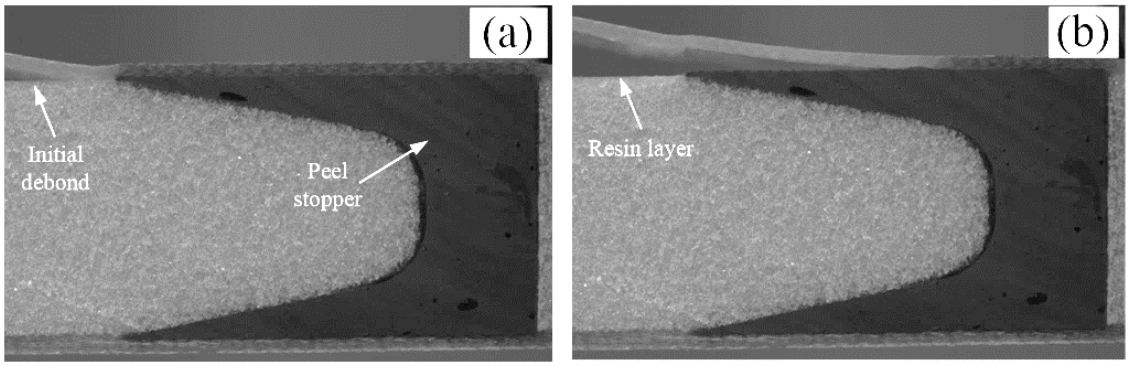

Figure 7.1: (a) Crack approaches and (b) crack passes the tri-material junction

7.3 Configurations of the peel stopper

Three different configurations of peel stoppers are studied. In all cases the peel stopper geometry is as shown in Figure 7.2 (a) which is a modification of the original design by Jakobsen et al. [18] (see Figure 7.1). Here the peel stopper is moulded into a 'U' shaped geometry so that the volume of material is significantly reduced, thus reducing the mass correspondingly. The PU material has a density of 1450 kg/m^3 [135] which is much higher than that of the PVC foam core material. Thus, the reduction of the peel stopper weight is important. The PU material used for the peel stopper is reinforced by a layer of glass fibre fabric as shown in Figure 7.2 (b). Comparing to the original design, the glass fibre fabric is introduced to enhance the peel stopper fracture toughness and to prevent the crack from penetrating into the peel stopper.

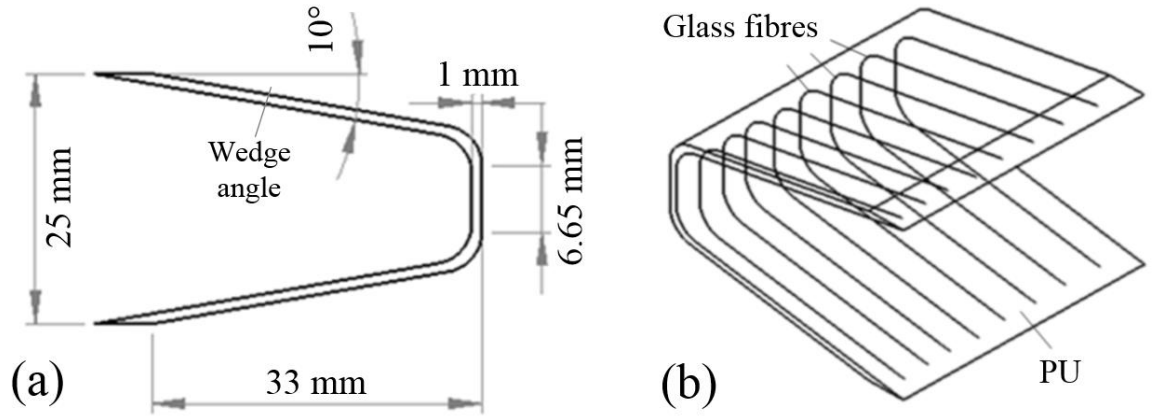

Figure 7.2: (a) Peel stopper shape and fibre reinforcement alignment inside the PU material and (b) the dimension of the peel stopper.

The peel stopper is moulded in a 'U' shape using a mould made of Polypropylene. The polypropylene does not bond with the PU material making it a good choice for the mould tool as extra coatings are not required. The mould is shown in Figure 7.3 (a) which includes two parts: the lower and upper parts. The fabrication firstly applies the PU material in the lower part of the mould. The PU material in liquid form and can take the shape of the mould. The UD fibres are then attached to the upper part with the main fibre direction following the arrows as shown in Figure 7.3 (a). Finally, the upper part of the mould together with the fibres are pressed into the lower part containing the PU adhesive. Figure 7.3 (b) shows the side view of the assembled mould where the gap between the upper and lower parts are filled with the PU and fibres. The mould is closed tightly using bolts and nuts to contain the material in the desired dimensions. When the mould is fully closed, the excess PU material is driven out by holes drilled in the mould body.

The three different configurations of peel stoppers are shown in Figure 7.4. In configuration 1 (C1), the PU material is directly bonded to the foam core (i.e. the same as that used in the original design [18]). As the 'U' shaped peel stopper has the same wedge angle (10°) as that suggested in the original design (see Figure 7.1), the configuration at the tri-material junction of C1 remains the same as that of the original peel stopper. In configurations 2 (C2) and 3 (C3) modifications of small material features at the tri-material junction are made. The aim is to change the local effects at the tri-material junction and thereby enabling crack deflection. In C2 the PU material is also directly bonded to the foam, but the glass fibre layer inside the PU material protrudes from the peel stopper tip. The fibre layer is infused together with the face sheet during the manufacturing process. The aim of C2 is to isolate the face sheet/peel stopper interface from the crack path by increasing the fracture toughness at the peel stopper tip. In C3 an extra fibre layer is introduced at the PU/foam interface when the PU material is bonded to

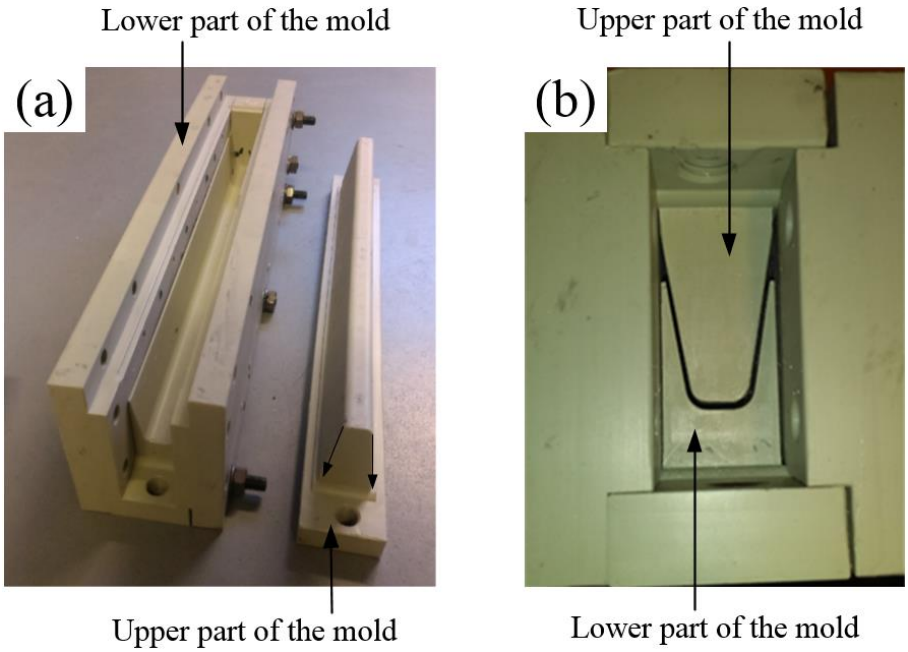

Figure 7.3: (a) The lower and upper parts of the peel stopper polypropylene mould and (b) side view of the assembled mould showing the peel stopper shape

the foam. The part of fibre layer behind the peel stopper is attached to the face sheet as for C2. C3 also seeks to isolate the face sheet/peel stopper interface from the crack path. Compared to C2, C3 seeks to alleviate the stress concentration at the tri- material junction. As shown in Figure 7.4 (C3), the local stress concentration that determines the crack path is shifted from the tri-material junction to the point behind (i.e. on the left hand) the peel stopper tip.

In the following sections, the modified peel stoppers are examined experimentally and their ability to deflect the interfacial crack under static loads is established. The experimental results are used to validate FE models of sandwich specimens containing the different peel stopper configurations.

7.4 Test specimens and loading conditions

The face sheet and core materials used in the sandwich specimens are identical to those used in chapters 5 and 6. The core materials include two blocks of PVC foam which have been machined to the required geometries using a CNC milling centre; the two blocks of foam are attachd to the inner and outer side of the peel stopper as shown in Figure 7.4. The fibre layers introduced inside the PU material (i.e. the peel stopper) and placed at the foam/PU interface in C3 are made from the same E-glass fabric that was used for the face sheet.

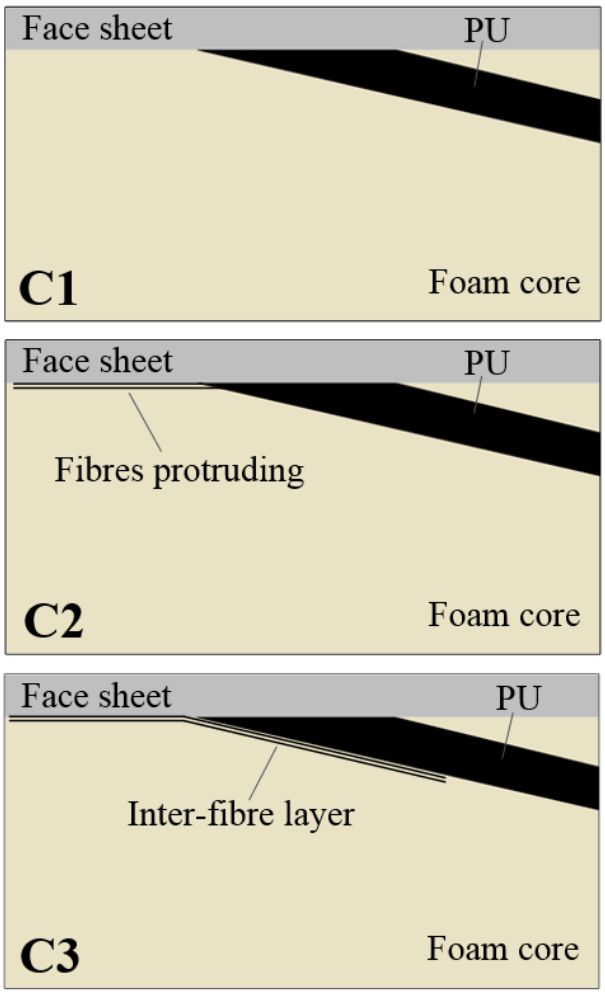

Figure 7.4: Peel stoppers with 3 different configurations at the tri-material junction

The sandwich panel that incorporates the peel stopper was manufactured using the RIM approach. Prior to the manufacturing, the peel stopper was adhesively boned to the foam using the Araldite 2000 epoxy adhesive as suggested in [18]. For C3, the extra fibre reinforcement layer was firstly placed on the foam (i.e. the block of foam that was attached to the inner side of the peel stopper) and the epoxy adhesive was applied (see Figure 7.5 (a)). The foam was then bonded to the peel stopper as shown in Figure 7.5 (b). To reduce the thickness of the extra fibre layer, the fibres along the transverse direction were removed which can be seen in Figure 7.5. This was also done for the fibres protruding from the peel stopper tip in C2. An initial debond was created between the face sheet and the core across the width of the panel.

Sandwich beams of 220 mm length were cut from the panels. Three specimens, each containing one configuration of the peel stopper were tested. The specimens were loaded using the MMB test rig as shown in Figure 7.6. The MMB test rig was used because the

applied loading mode at the crack tip remains the same during the crack propagation [62]. Thus, the fracture behaviour is not influenced by any change in mode-mixity during the crack propagation. The dimension of each specimen is shown in Table 7.1. To provide a mode I dominated loading at the crack tip, a lever arm distance of 60 mm with a 160 mm span length was used which provide a mode-mixity angle, φ_F, of about -13° for each specimen (predicted by the FE model described in section 7.5). The static tests were conducted in the Instron ElectroPuls machine (described in chapter 6) with a displacement rate of 1 mm/min.

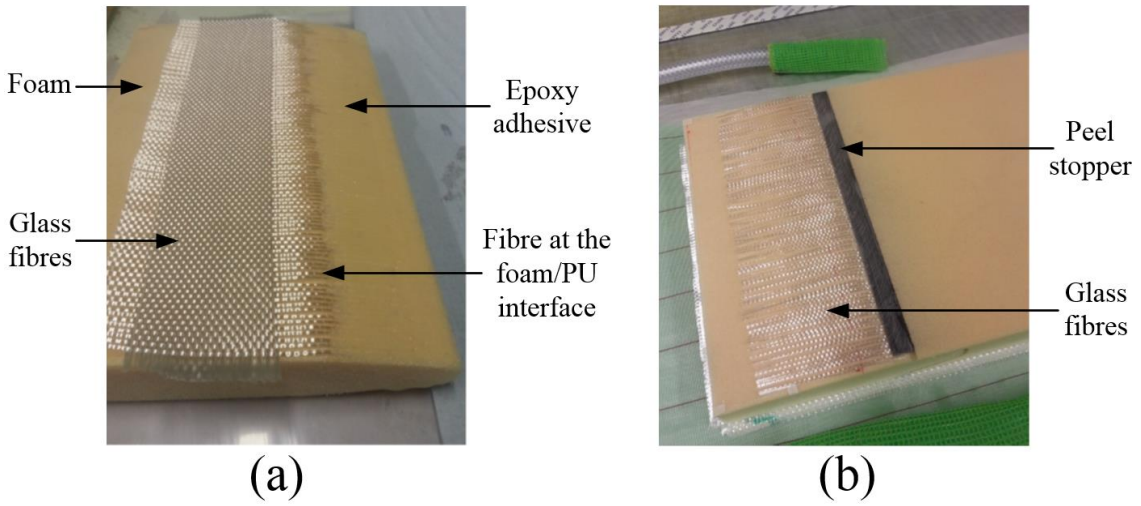

Figure 7.5: Assembling of the foam and the peel stopper for C2 with (a) fibres placed on the foam and (b) the bonding of the peel stopper, foam and the glass fibres

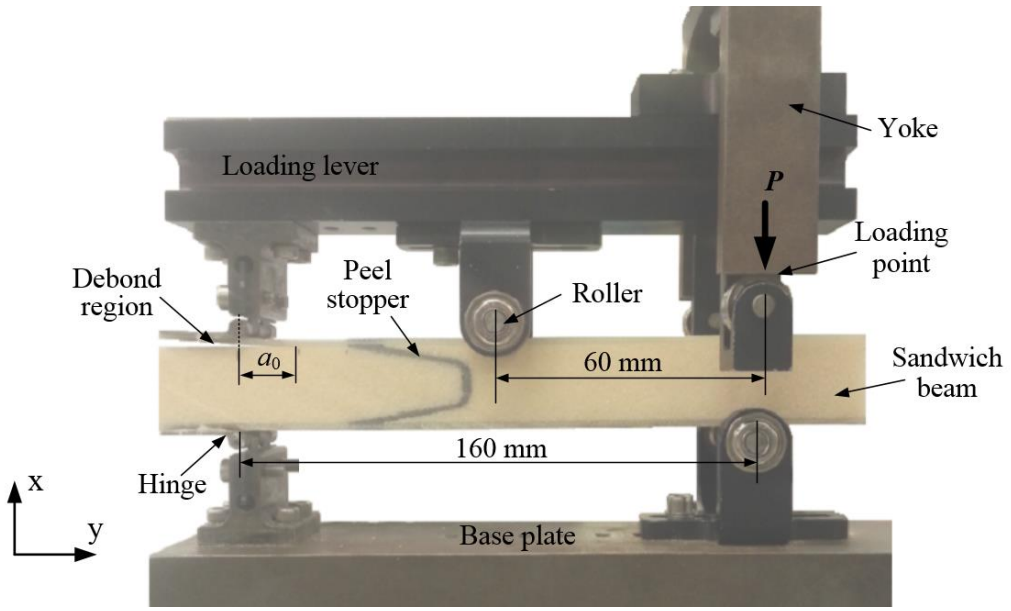

Figure 7.6: Sandwich beam specimen with peel stopper loaded in the MMB test rig

Table 7.1 Dimension of the sandwich specimen with different configurations

Specimen	Initial crack length (a_0)	Specimen width (b)	Face sheet thickness (t_f)
C1	14.0 mm	29.2 mm	1.6 mm
C2	13.5 mm	30.1 mm	1.7 mm
C3	14.0 mm	30.2 mm	1.7 mm

7.5 FE modelling

FE models of the test specimens have been built using the commercial FE package ANSYS 15.0. The FE models were developed by Georgios Martakos as a part of the research collaboration described in Figure 1.2. The FE models were used to predict the displacements applied to the specimen (i.e. the actuator displacement) at the required crack tip energy release rate and crack length. This allows fatigue tests to be conducted under a controlled crack tip energy release rate by adjusting the actuator displacement (predicted by the FE model according to the energy release rate and the crack length) during the crack propagation. A detailed description of the fatigue test methodology is provided in Chapter 8.

The FE models used 8-node 2D plane stress elements (PLANE 183) with an average element size of 0.5 mm. At the crack tip, the number of elements range from a minimum 36 to 144 and from 5 to 10 μm in size. Figure 7.7 shows the FE meshes corresponding to the three peel stopper configurations and the geometry of the sandwich beam model. The boundary conditions applied to the model were the same as those described in the MMB model in Chapter 6. The detailed models of different crack path scenarios around the tri-material junction for each configuration are shown in the images a-f in Figure 7.7.

In the models of C2 and C3, an extra layer of elements of 0.1 mm (element with orange colour) was used to simulate the protruding fibre layer and the inter-fibre layer for configurations C2 and C3, as shown in image c and e. In C2 the extra fibre layer was attached to the tri-material corner tip to simulate the fibres protruding from the peel stopper (see image c).

The FE model calculates the crack tip energy release rate and the mode-mixity using the CSDE method as has been described in Chapter 6.

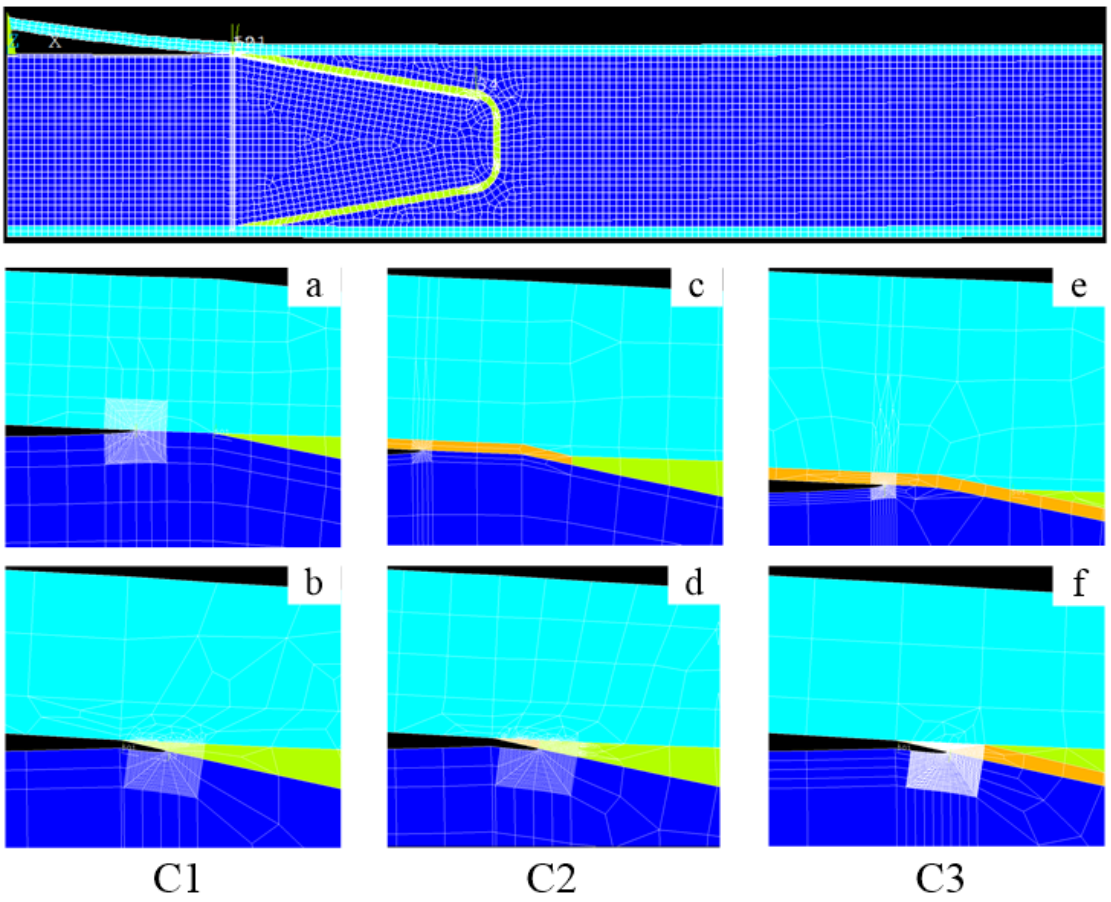

Figure 7.7: FE modelling of the sandwich specimens with different crack path scenarios around the tri-material junction for C1 (images a and b), C2 (images c and d) and C3 (images e and f).

7.6 Static fracture testing results

This section shows the crack paths observed for the different peel stopper configurations. Moreover, the load-displacement data obtained from the tests are compared to the FE results for validating the models. The crack lengths input into the FE models were obtained from the images recorded during the testing (recorded from the side of the specimen). The images were calibrated using a pre-applied scale on the specimen surface (as explained in chapter 6).

The crack paths observed from the two sides of specimen C1 are shown in Figure 7.8 (a) and (b) respectively. The crack propagated in the foam core just below the interface as it approached the peel stopper tip. However, it can be seen that the crack shows different paths on each side of the specimen after reaching the tri-material junction. The crack propagates along the face sheet/peel stopper interface on one side of the specimen as

shown in Figure 7.8 (a). On the other side of the specimen (see Figure 7.8 (b)), the crack is deflected into the core at the tri - material junction but a crack at the face sheet/peel stopper interface can be also observed. To demonstrate the crack propagation process observed in Figure 7.8 (b), the images collected during the tests are shown in Figure 7.9. In Figure 7.9 (a) the crack deflects at the tri-material junction. As the crack propagates, a debond occurs at the face sheet/peel stopper interface, see Figure 7.9 (b) (see the close-up area). The debond propagated rapidly along the face sheet/peel stopper interface with the increase of the bending in the face sheet as shown in Figure 7.9 (c) and (d).

Figure 7.10 shows the crack path observed from the specimen C2. It can be observed that the crack was successfully deflected at the tri-material junction on both sides of the specimen. No debond was observed that initiated at the face sheet/peel stopper interface in the specimen.

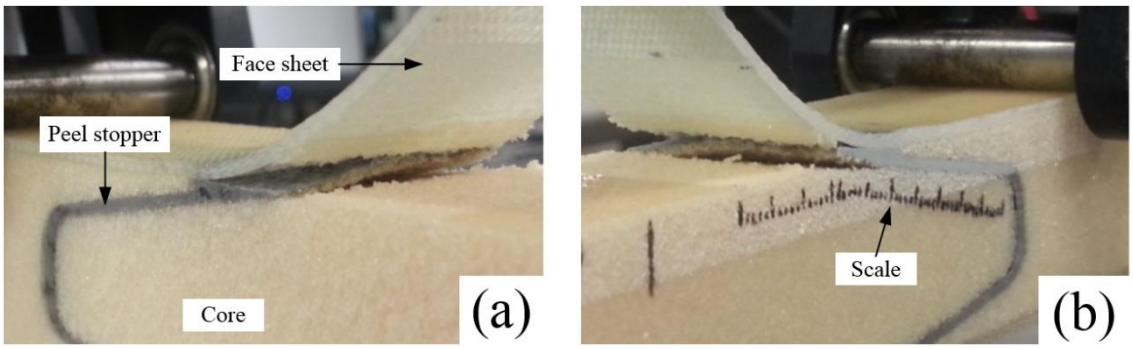

Figure 7.8: Crack path on each side of the specimen C1

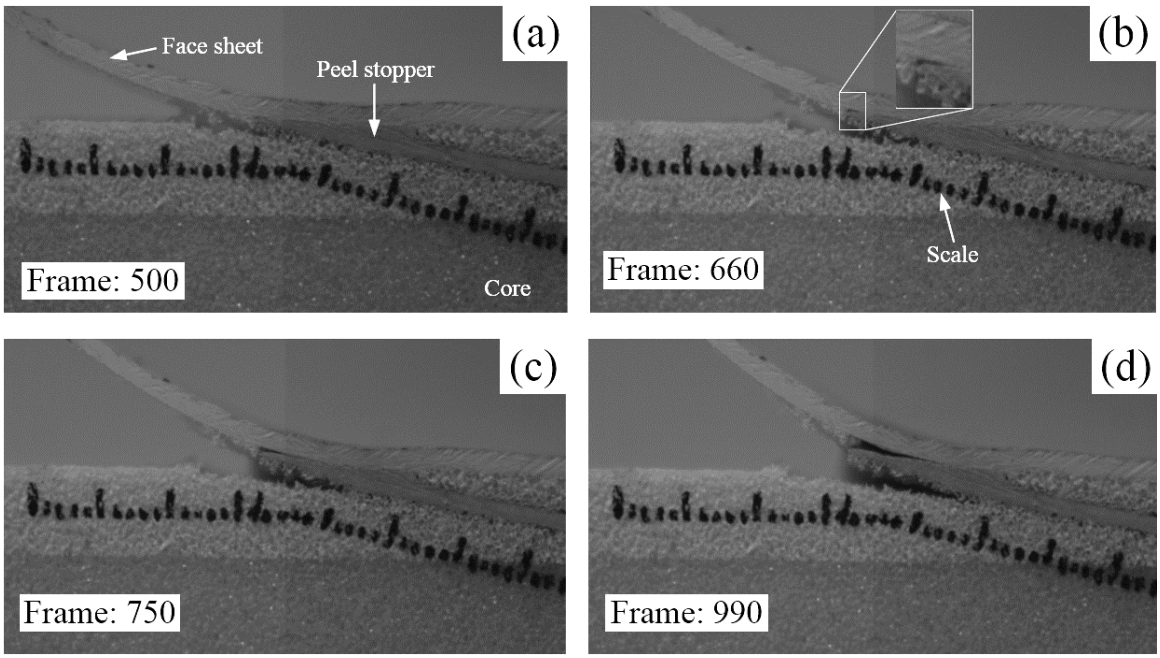

Figure 7.9: Images collected from one side of the specimen C1

The crack path observed in specimen C3 is shown in Figure 7.11. On both sides of the specimen, it is clear that the crack was successfully deflected into the core at the tri-material junction. In Figure 7.11 (b), a crack is observed that propagates at the face sheet/peel stopper interface on one side of the specimen. This crack propagation initiated from the debond damage that developed after the crack was deflected, and which can be seen in Figure 7.12 (b) (see the close-up area) at the face sheet/peel stopper interface.

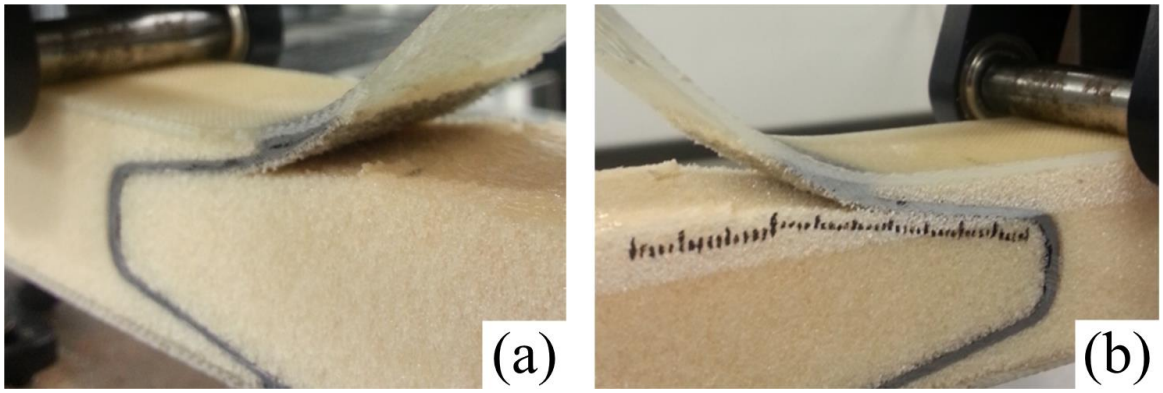

Figure 7.10: Crack path on each side of the specimen C2

It has been shown that the crack could not be deflected effectively by configuration C1. This was expected as the design features of C1 at the tri-material junction are identical to those of the original peel stopper design. However, for C2 and C3, the changes of design features at the tri-material junction proposed in this work were shown to be capable of the deflecting the interface crack. No strong conclusions can be drawn on the basis of just one single static test of each peel stopper configuration, but there is a strong indication that configurations C2 and C3 are more efficient peel stopper designs than C1. The debonding observed at the face sheet/peel stopper interface for both specimens C1 and C3 could be caused by defects introduced during the manufacturing process, whereas it is assessed that the manufacturing of C2 possess less risk of debond defects to be generated during the infusion process. To provide a further insight regarding the efficiency of the different peel stopper designs, an investigation of the mechanisms that result in crack deflection is required. Therefore, the local effects (or local stress concentrations) introduced by the peel stopper in the different configurations of the tri-material junction corresponding to C1, C2 and C3 are studied using TSA in Chapter 8, under cyclic loading.

To perform the FE analyses, images and corresponding load data output from the test machine were recorded simultaneously during the tests. The loads and the corresponding crack lengths (determined from white light images) were then input into the FE models for deriving the actuator displacement (δ_{MMB}, see Figure 7.13) based on the relationship given by [62]:

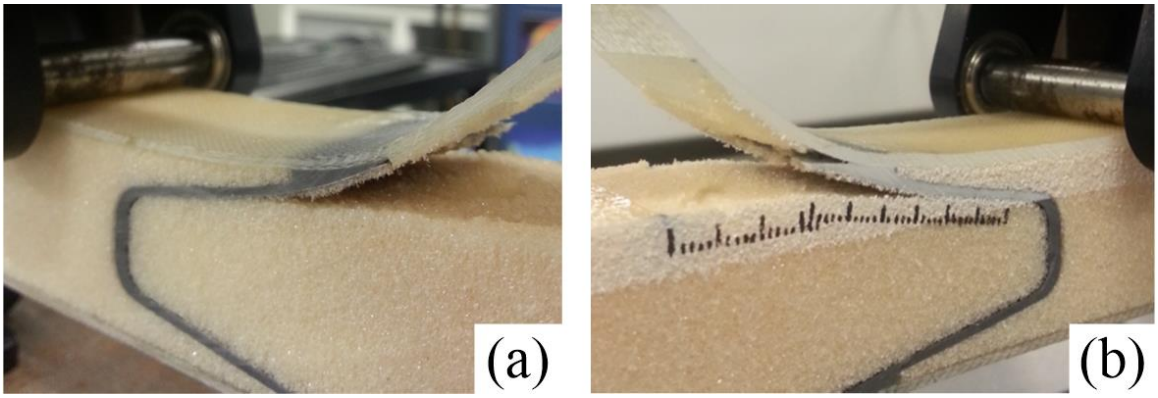

Figure 7.11: Crack path on each side of the specimen C3

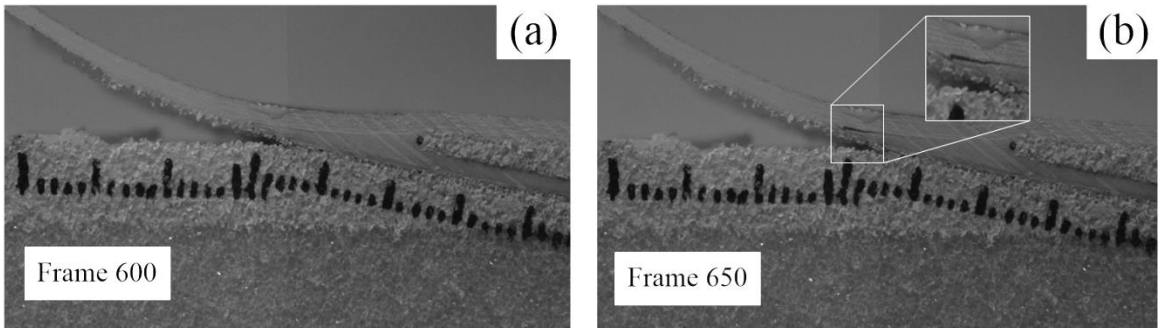

Figure 7.12: Images collected from one side of the specimen C3

$$\delta_{\mathrm{MMB}} = \delta_1 + \frac{c}{L}(\delta_1 + \delta_2) \tag{7.1}$$

where δ_1 is the displacement of the central 'roller' line of the sandwich beam specimen (see Figure 7.7) and δ_2 is the crack tip opening displacement. δ_1 and δ_2 were obtained from the nodal displacements derived from the FE models.

Figure 7.14 plots the load-displacement data obtained from the experiments and the FEA for the different peel stopper configurations. The red dashed line shown in the figures indicates the value of the actuator displacement when the crack tip passed the peel stopper tip, i.e. the load-displacement curve shown on the right hand side of the red line was obtained after the crack tip passed the peel stopper tip. For specimen C1, two crack paths were observed across the specimen width when the crack passed the peel stopper tip. Thus, the load-displacement data on the right hand side of the red line are not available from the FE model. For all the different peel stopper configurations, the FE results show a good agreement with the results obtained from the experiments. This indicates that the FE model can predict the specimen behaviour during the crack propagation.

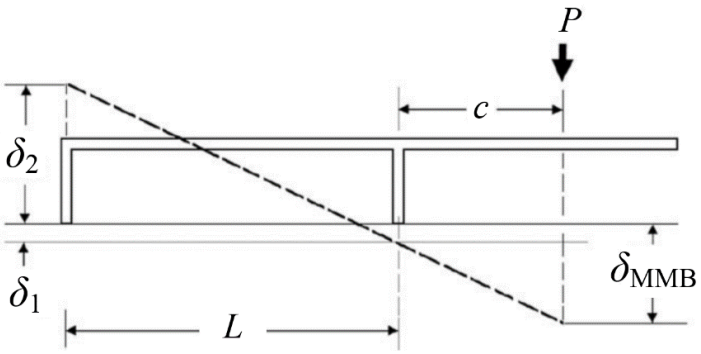

Figure 7.13: Displacement at the loading point [62]

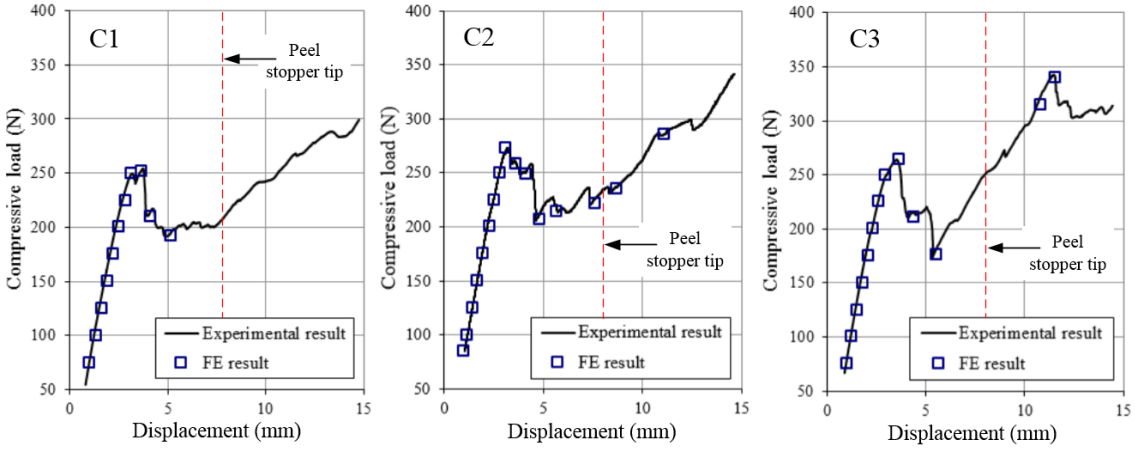

Figure 7.14: Comparison of the results between the experiments and the FEA for different peel stopper configurations

7.7 Summary

The crack path at the tri-material junction of the peel stopper proposed by Jakobsen *et al.* [18] (i.e. the original peel stopper) has been established under static, mode I dominated loading. It was shown that this peel stopper configuration could not deflect the crack into the core at the tri-material junction under Mode I loading. Moreover the crack tip location (i.e. in the face sheet/core interface or in the foam core) at the tri-material junction is shown to have no effect on the crack path.

Three different modifications of the peel stopper design have been proposed in the current work. The peel stopper geometry was modified to a 'U' shape to reduce the volume and mass, and glass fibre layers were introduced into the PU material to increase the fracture toughness of the peel stopper. The modified peel stoppers of three different configurations (C1, C2 and C3) were studied. C1 essentially was of the same design

configuration at the tri-material junction of the original peel stopper. For C2 and C3, modified design configurations at the tri-material junction were proposed. The aim was to influence the local effects (stress concentrations) introduced at the tri-material junction thereby allowing the crack to be deflected. In the static tests it was demonstrated that C2 and C3 were both capable of deflecting the crack at the tri-material junction. However, to achieve a thorough understanding of the efficiency of the peel stopper concept, an investigation of the local stress fields introduced by the peel stopper at the tri-material junction is required. Thus, in Chapter 8 TSA is used to investigate the local effects at the tri-material junction under fatigue loading conditions.

The FE models developed by Georgios Martakos have been validated using the load-displacement data obtained from the static loading experiments. Using experimentally obtained loads and corresponding crack lengths, it has been shown that the models can accurately predict the corresponding specimen displacements during the crack propagation process. This demonstrates that the displacements applied to the specimens at the required energy release rates and crack lengths can be determined, so the actuator displacements to achieve the required energy releases rate can be predicted. Thus, by adjusting the displacement applied on the specimen during crack propagation, the energy release rate at the growing crack tip can be controlled in the fatigue tests.

Chapter 8

Full-field analysis of stress distribution at crack arresting devices

8.1 Introduction

To enable the crack to deflect away from the face sheet, modifications of the peel stopper at the tri-material junction were described in Chapter 7. It was shown that the modified configurations can deflect the crack more effectively under static mode I dominated loading. So TSA can now be used with the new MC method described in Chapter 4 to determine the stress state in the neighbourhood of the tri-material junction under mode I fatigue loading conditions. The aim is to investigate the local effects at the tri-material junction introduced by different peel stopper configurations (i.e. C1, C2 and C3) and provide a further insight into the mechanical behaviour of sandwich structures in the vicinity of the peel stoppers.

The chapter opens with a description of the sandwich beam specimens studied in the fatigue. It is necessary to perform the fatigue tests using a controlled energy release rate, so that the FE model validated in Chapter 7 can be used to determine the displacements to achieve controlled crack propagation. A description of the fatigue test procedure and the experimental setup for the TSA is provided and the crack paths observed from different configurations of the peel stopper are presented. Finally, the local effects introduced by different peel stopper configurations are identified using the TSA data collected from the neighbourhood of the tri-material junction. The efficiency of the modified peel stopper configurations is evaluated.

8.2 Test specimens

Three sandwich panels each containing a peel stopper (i.e. C1, C2 and C3) were manufactured. The constituent sandwich materials and the manufacturing process for each configuration are the same as described in section 7.4. For each configuration, three sandwich beam specimens were cut from the panel. The specimens were loaded using the MMB test rig which is the same as used in the static test. A lever arm distance of 75 mm with a span length of 180 mm (see Figure 6.4) was used to provide mode I dominated loading. Table 8.1 summarises the dimensions of each sandwich specimen and the mode-mixity, φ_F. The distance between the initial crack tip and the peel stopper tip (a_d) was relatively long to allow the crack to propagate before reaching the tri-material junction. This is important, as a well-defined stable crack growth must be achieved ahead of the tri-material junction. Practically the same mode-mixity angle was applied to each specimen, thus enabling the fatigue crack path in different specimens and configurations to be examined under the same loading conditions.

Table 8.1 Dimensions and the loading conditions of each sandwich specimen

Specimen	Peel Stopper configuration	a_0 (mm)	a_d (mm)	b (mm)	φ_F (°)
C1_f1	C1	17	15	32	-10.2
C1_f2		18	15	32.5	-10.2
C1_f3		18	14	33.5	-10.2
C2_f1	C2	17	16	31	-10.4
C2_f2		19	15	32	-10.5
C2_f3		19.5	15	30	-10.5
C3_f1	C3	15.5	15	32.1	-9.7
C3_f2		19	15.5	30.5	-9.9
C3_f3		20	15.5	30.9	-9.9

8.3 Fatigue test methodology

Fatigue tests can be performed either in load control or displacement control modes. The displacement controlled tests generally offer more stable test conditions and promote stable crack growth. Thus, the tests were performed using displacement control with a displacement ratio R ($\delta_{min}/\delta_{max}$) = 0.2, and a loading frequency of 3 Hz.

A disadvantage of the displacement controlled fatigue test is that the energy release rate decreases with crack growth. This means that more loading cycles are required to achieve the desired crack length. The specimens were tested until the crack length was about 25 mm, i.e. 10 mm after the tri-material junction. During the crack propagation the energy release rate will decrease significantly, and the crack may stop growing before it has reached the tri-material junction. Therefore during the tests it is necessary to change the displacement amplitude to control the ΔG at the prescribed value (see Figure 8.1 (a)). The 'ΔG control' is described in Figure 8.1 (b). Firstly the FE model described in Chapter 7 is used to predict the maximum displacement (δ_{max}) shown by the black line in Figure 8.1 (b). A ΔG of 450 J/m^2 was selected (i.e. smaller than the interfacial fracture toughness obtained in Chapter 6). For the small displacement ratio of R = 0.2 the difference between ΔG and G_{max} is insignificant [133]. Thus, δ_{max} can be obtained directly using the value of 450 J/m^2, so δ_{max} was calculated in increments of 1 mm (note the 0 mm crack increment as shown in Figure 8.1 (b) corresponds to the initial crack length). The displacement amplitude (δ_{amp}) and the mean displacement (δ_{mean}) were calculated according to the δ_{max} and displacement ratio (R) as follows:

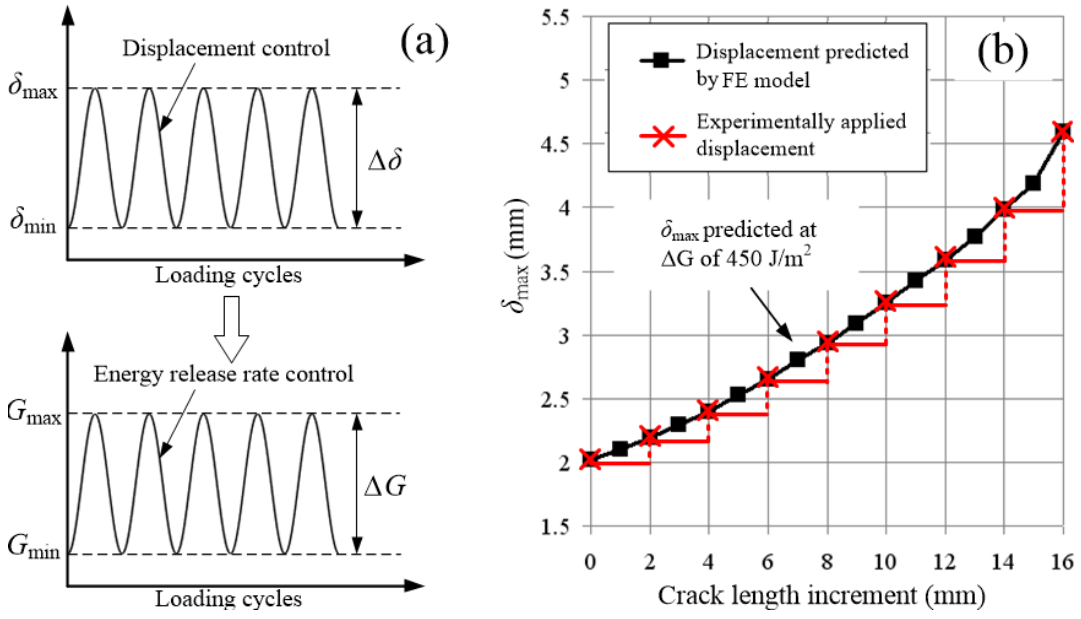

Figure 8.1: (a) Displacement control and energy release rate control in the fatigue test, (b) δ_{max} against crack increment at ΔG of 450 J/m^2

$$\delta_{amp} = \frac{\delta_{max} - R\delta_{max}}{2}$$
$$\delta_{mean} = R\delta_{max} + \delta_{amp} \quad (8.1)$$

The fatigue test was initially setup by using the δ_{amp} and δ_{mean} calculated at 0 mm crack increment. This allowed the fatigue test to be started with ΔG of 450 J/m^2. The δ_{mean} and the δ_{amp} were then adjusted for each 2 mm crack increment as indicated by the red line shown in Figure 8.1 (b). By doing this, the ΔG value was maintained close to 450 J/m^2 throughout the test.

8.4 Experimental arrangements

The experimental setup for the TSA is shown in Figure 8.2. The IR camera captured the thermal images for TSA with a frame rate of 383 Hz. To perform the MC, images for DIC were captured by a white light camera (LaVision VC-Imager E-lite) placed behind the IR camera. Both cameras were aligned perpendicular to the specimen surface. The IR camera was placed on a tripod which allows the camera to be moved up and down vertically.

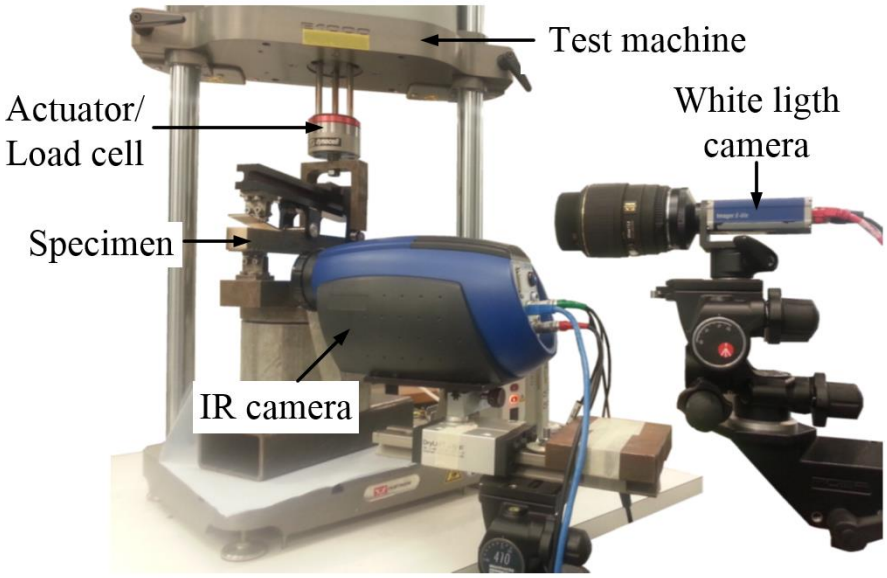

Figure 8.2: Test setup for the TSA measurement in the fatigue test

The fatigue test procedure is described by the flowchart shown in Figure 8.3. The test was started using the δ_{amp} and δ_{mean} derived at 0 mm as described in section 8.3. When the crack tip has moved by 2 mm, the test was paused. The δ_{amp} and δ_{mean} values were adjusted and the fatigue test was restarted using the new δ_{amp} and δ_{mean} values. This process was continued until the crack propagated into the neighbourhood of the tri-material junction (i.e. when the distance between the crack tip and the peel stopper tip was smaller than 6 mm). During the process, the crack tip location was determined from the live thermal images where the pixel resolution was calibrated beforehand using a pre-applied scale on the specimen surface. Once the crack tip reached the region of interest, the fatigue test was paused after a set of 1200 thermal images was recorded for the TSA, and the position of the IR camera adjusted, so the white light camera could observe the specimen. The images for DIC were then captured as the specimen was loaded *quasi* statically over a range equivalent to the dynamic loading range. The fatigue test was restarted using the new δ_{amp} and δ_{mean} values and the IR camera returned to its original position to observe the region of interest. For each 2 mm crack increment, the sequence of thermal and white light images captured was repeated until the crack had propagated 10 mm beyond the tri-material junction.

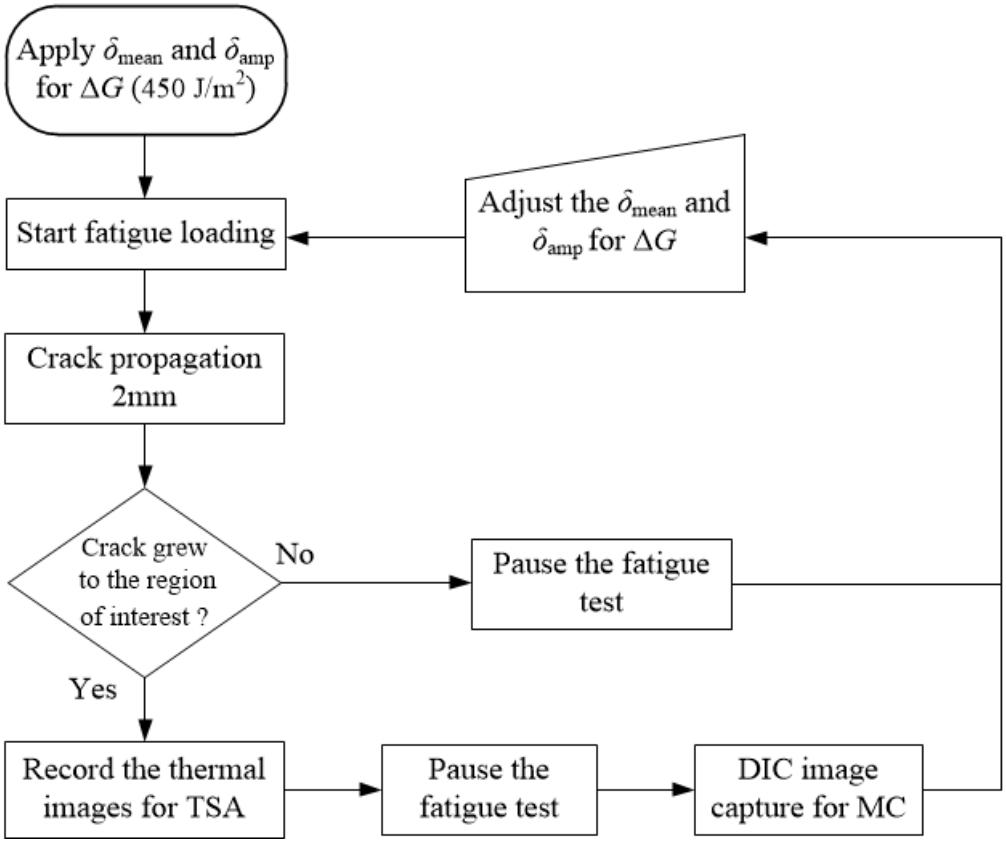

Figure 8.3: Flowchart of the fatigue test procedure

To provide an appropriate field of view with sufficient spatial resolution in the neighbourhood of the tri-material junction, the IR G0.5 lens described in section 3.4 was used. The IR camera equipped with the G0.5 lens was positioned 50 mm away from the specimen surface which provided a region of interest of 17.9 × 14.3 mm^2, with a spatial resolution of 0.06 mm/pixel. To achieve a similar field of view to that of the thermal data, the 105 mm lens was used with the white light camera. The lens was set with a scale factor of 0.01 mm/pixel to provide a region of interest of 24 × 22 mm^2.

The thermal and white light images collected in the neighbourhood of the tri-material junction are shown in Figure 8.4 (a) and (b) respectively. In both images the position of the peel stopper is marked by the red dashed line. A small piece of foil was attached to the face sheet to help identify the position of the peel stopper tip. The white rectangular area bounded by the position marks is the region of interest (i.e. the area where the MC was applied). The grid shown in Figure 8.4 (b) shows the interrogation cells used for the DIC.

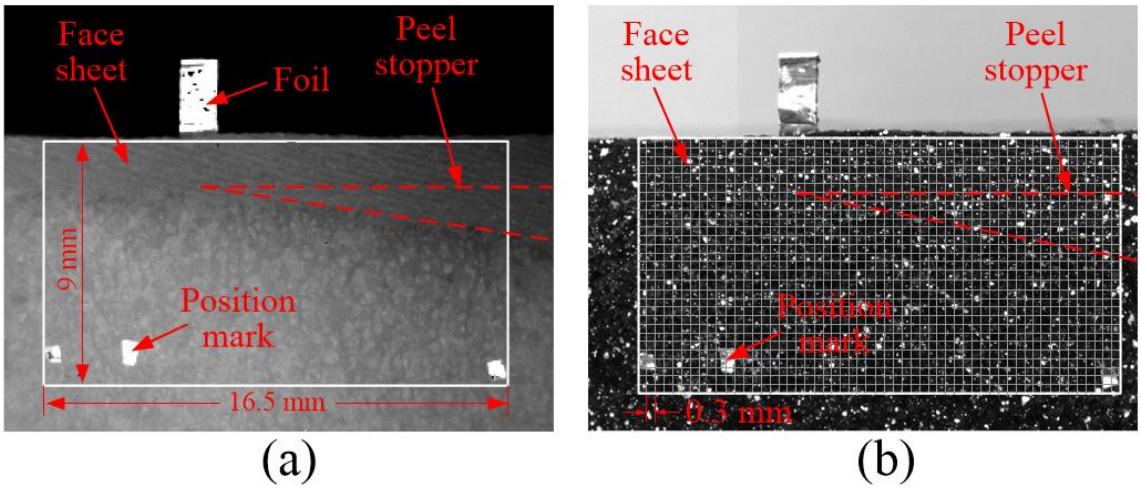

Figure 8.4: (a) Thermal image and (b) white light image collected from the specimen surface in the neighbourhood of the tri-material junction

8.5 Fracture testing results

Table 8.2 summarises the crack paths of the different specimens observed in the fatigue tests. In specimens C1 the crack propagated in the foam just below the interface as it approached the tri-material junction. There are two specimens (C1_f2 and C1_f3) where the crack did not deflect at the tri-material junction. Figure 8.5 shows the crack paths captured at the tri-material junction from specimens C1. In all cases the crack kinked back towards to the face sheet at the tri-material junction resulting in the crack

propagating at the face sheet/peel stopper interface in specimens C1_f2 and C1_f3. In specimens C2 the crack firstly propagated at the face sheet/core interface and then grew in the foam just below the interface. Figure 8.6 (a) shows the crack path at the tri-material junction observed from specimen C2_f2. In specimens C3 the crack propagated with different paths as it approached the tri-material junction. The crack propagated along the face sheet /core interface in specimens C3_f1 and C3_f2. In specimen C3_f3 the crack firstly propagated along the interface and then grew in the foam. Figure 8.6 (b) and (c) show the crack paths at the tri-material junction obtained from specimens C3_f1 (i.e. crack tip in the face sheet) and C3_f3 (i.e. crack tip in the foam core) respectively, i.e. the crack deflected regardless of where the crack tip was located. Additionally, in all cases there was no debonding at the face sheet/peel stopper interface, unlike the static loading described in the previous chapter.

Table 8.2 Crack paths observed from different specimens

Specimen	Peel Stopper configuration	Crack paths before the tri-material junction	Crack paths at the tri-material junction
C1_f1	C1	Foam	Deflected
C1_f2		Foam	Not deflected
C1_f3		Foam	Not deflected
C2_f1	C2	Interface, foam	Deflected
C2_f2		Interface, foam	Deflected
C2_f3		Interface, foam	Deflected
C3_f1	C3	Interface	Deflected
C3_f2		Interface	Deflected
C3_f3		Interface, foam	Deflected

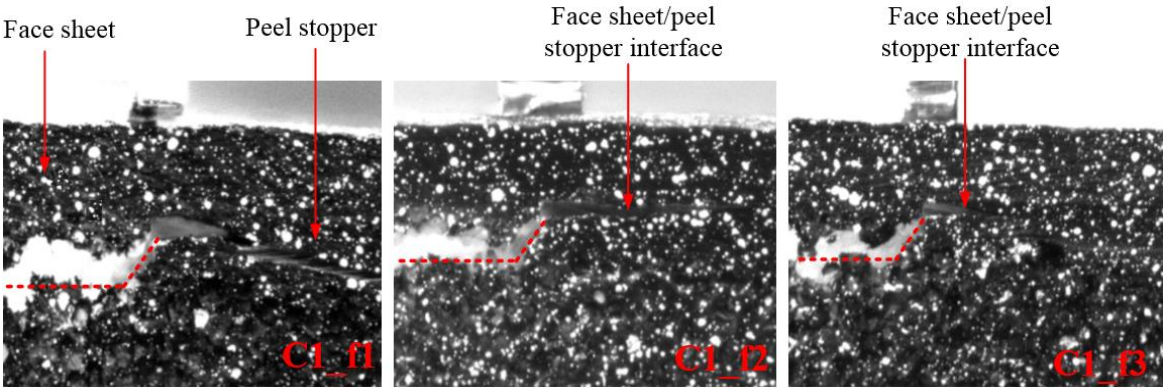

Figure 8.5: Crack paths at the tri-material junction observed from specimens C1

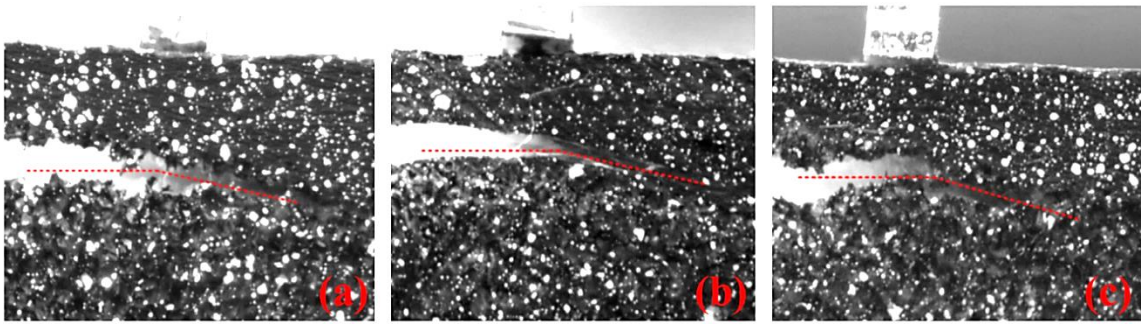

Figure 8.6: Crack paths at the tri-material junction observed from (a) specimen C2_f2, (b) specimen C3_f1, (c) specimen C3_f3

8.6 TSA results

TSA results are presented in the form of the non-dimensional stress metric, $\Delta T/T$, as described in section 5.4.3. An example showing the difference in the $\Delta T/T$ data before and after applying the MC is shown in Figure 8.7 as the crack propagated in the foam and reached the tri-material junction. After applying MC, a localised increase in $\Delta T/T$ at the tri-material junction, i.e. in the face sheet and at the crack tip, can clearly be observed in Figure 8.7 (b).

Figure 8.8 shows the $\Delta T/T$ values obtained in the vicinity of the tri-material junction from specimens C1. In Figure 8.8 Images 1, Images 2 and Images 3 were obtained when crack approached, reached and passed the tri-material junction respectively. As the crack approached the tri-material junction (see Image 1), the through-thickness stress gradient

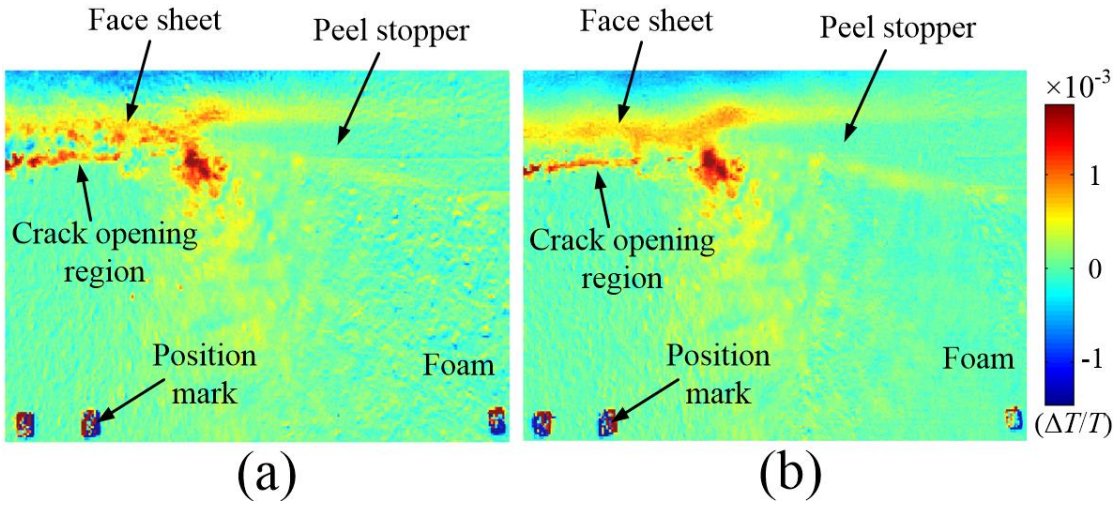

Figure 8.7: Comparison of the TSA results before (a) and after (b) MC

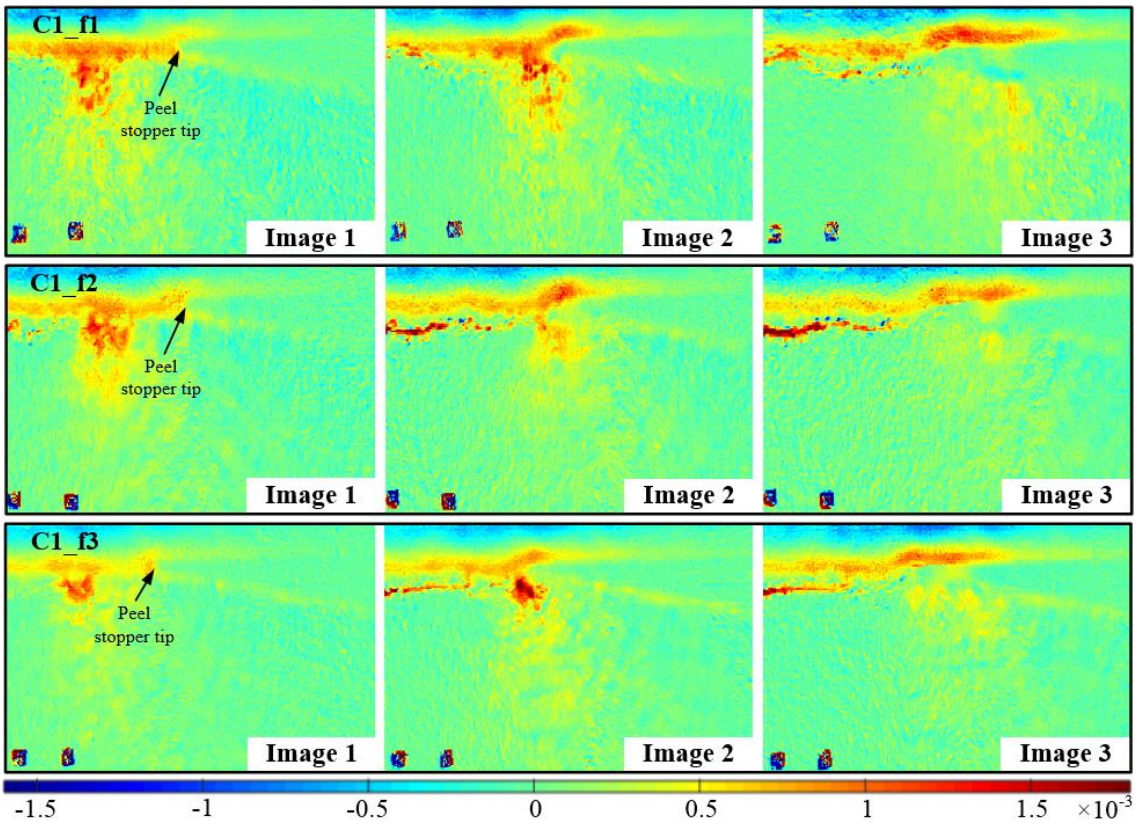

Figure 8.8: $\Delta T/T$ obtained from the neighbourhood of the tri-material junction from specimens C1

changes from compression to tension, as does the stress concentration in the foam just below the interface at the crack tip. When the crack reached the tri-material junction (Image 2), large $\Delta T/T$ values were obtained from the face sheet on the right hand side ahead of the peel stopper. The $\Delta T/T$ values in the face sheet ahead of the peel stopper tip are of comparable magnitude to those in the foam below the peel stopper tip (i.e. the crack tip). As the thermoelastic constant of the foam is about 20 times higher than that of the E-glass/epoxy composites (see section 5.3), this indicates that the stress produced in the face sheet ahead of the peel stopper tip is much higher than that at the crack tip. After the crack passed the tri-material junction, two crack paths were observed in specimens C1 as described in section 8.5. Although the crack was deflected in specimen C1_f1, an increase in $\Delta T/T$ in the face sheet close to the face sheet/peel stopper interface is seen in Image 3. This may be due to weak bonding between the face sheet and the peel stopper. In specimens C1_f2 and C1_f3, the crack was not deflected; hence large $\Delta T/T$ values are generated in the face sheets.

Figure 8.9 shows the $\Delta T/T$ data obtained from specimens C2. Here in all specimens the crack propagated in the foam just below the interface and was deflected at the tri-material junction. The $\Delta T/T$ values obtained as the crack approached the tri-material junction (see

Image 1) show similar results to specimens C1. When the crack reached the tri-material junction (see Image 2), the $\Delta T/T$ value in the face sheet ahead of the peel stopper tip was much smaller than observed in C1. Moreover, an increase in $\Delta T/T$ occurs at the peel stopper/core interface compared to that observed for C1. After the crack passed the tri-material junction, large $\Delta T/T$ values were produced around the peel stopper/core interface. The $\Delta T/T$ values in the face sheet ahead of the peel stopper tip were much smaller than those observed in C1.

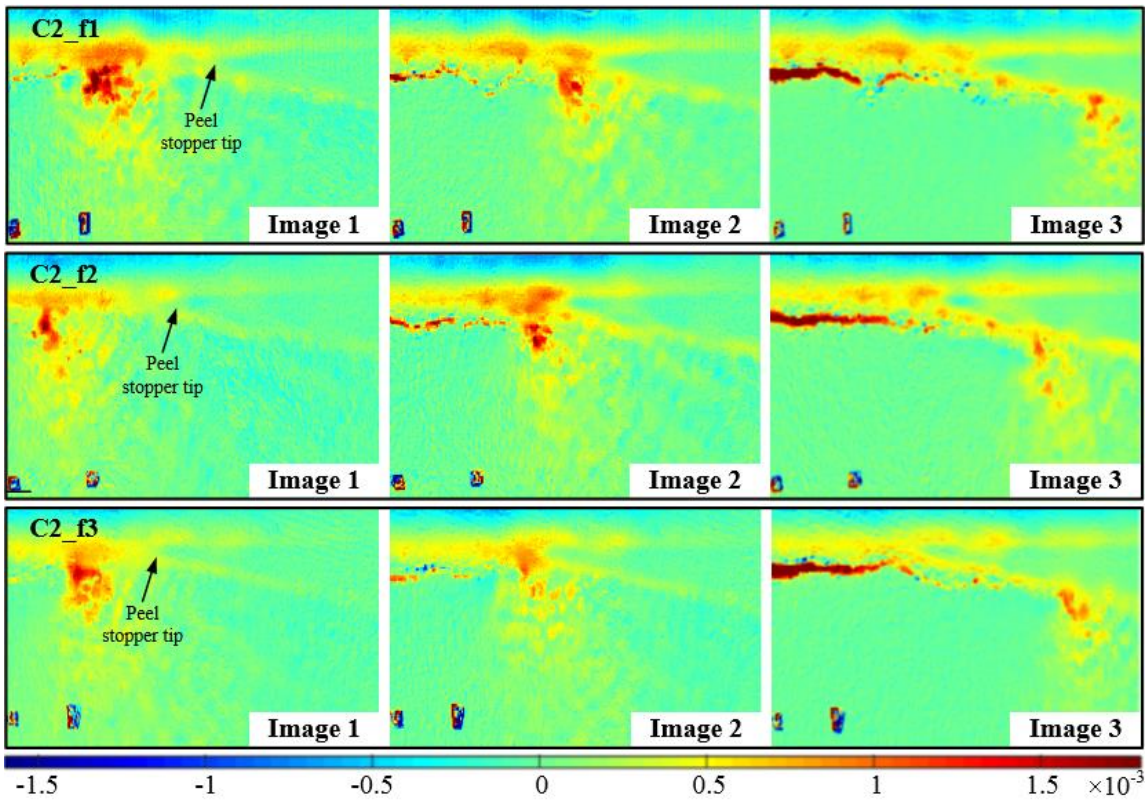

Figure 8.9: $\Delta T/T$ obtained from the neighbourhood of the tri-material junction from specimens C2

The $\Delta T/T$ values obtained from specimens C3 are shown in Figure 8.10. When the crack approached the tri-material junction (see Image 1), the $\Delta T/T$ values were similar to those obtained from specimens C1 and C2. When the crack reached the tri-material junction (see Image 2), the $\Delta T/T$ fields obtained from different crack tip locations (i.e. in the face sheet/core interface or in the foam core) were comparable to those observed from C2, i.e. large $\Delta T/T$ values were only produced on the left hand side of the peel stopper tip accompanied by an increase in $\Delta T/T$ at the peel stopper/core interface. After the crack was deflected, an increase in the $\Delta T/T$ values was observed in a small area ahead of the peel stopper tip; this was not the case for C1 and C3.

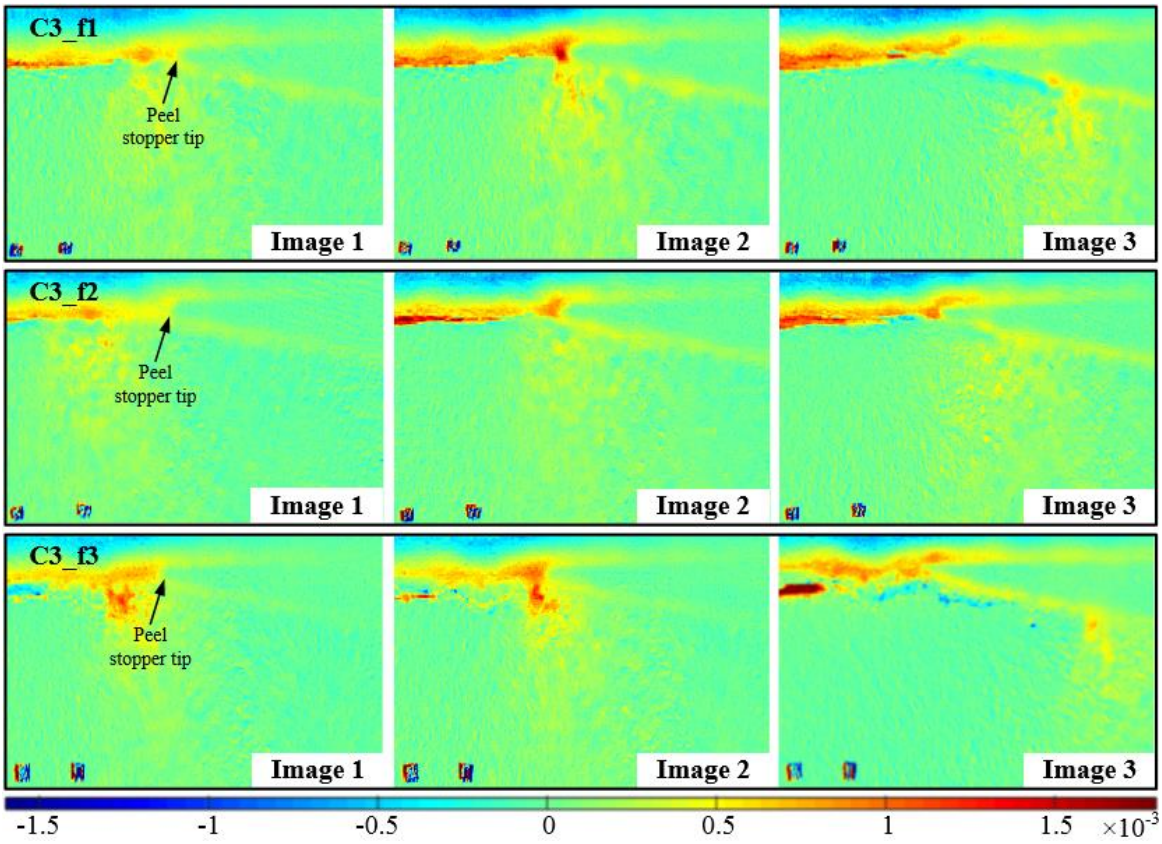

Figure 8.10: $\Delta T/T$ obtained from the neighbourhood of the tri-material junction from specimens C3

The local effects introduced by different peel stopper configurations have been identified using the TSA data collected from the neighbourhood of the tri-material junctions. It was shown that the local effects are strongly dependent on the peel stopper configurations, especially when the crack reached and passed the tri-material junction. Based on the TSA results, the effectiveness of the peel stopper configurations were evaluated and are described in the next section.

8.7 Discussion

To quantify results, the $\Delta T/T$ values in the face sheet along the y direction taken 8 pixels ahead of the peel stopper tip (see the black line in the images in Figure 8.11) were normalised with respect to the average $\Delta T/T$ value in the face sheet behind the peel stopper tip (see the black rectangular area in Figure 8.11). In Figure 8.12 the normalised $\Delta T/T$ values are plotted against the through thickness distance in the face sheet. The plots represent the through-thickness stress gradient in the face sheet (ahead of the peel stopper

tip) and change from compression to tension. It is shown that the normalised values obtained from specimens C1 are much larger than those obtained from specimens C2 and C3 at the interface with the peel stopper. This direct comparison demonstrated that there is a significant difference in the stresses generated in the face sheet ahead of the peel stopper in specimen C1.

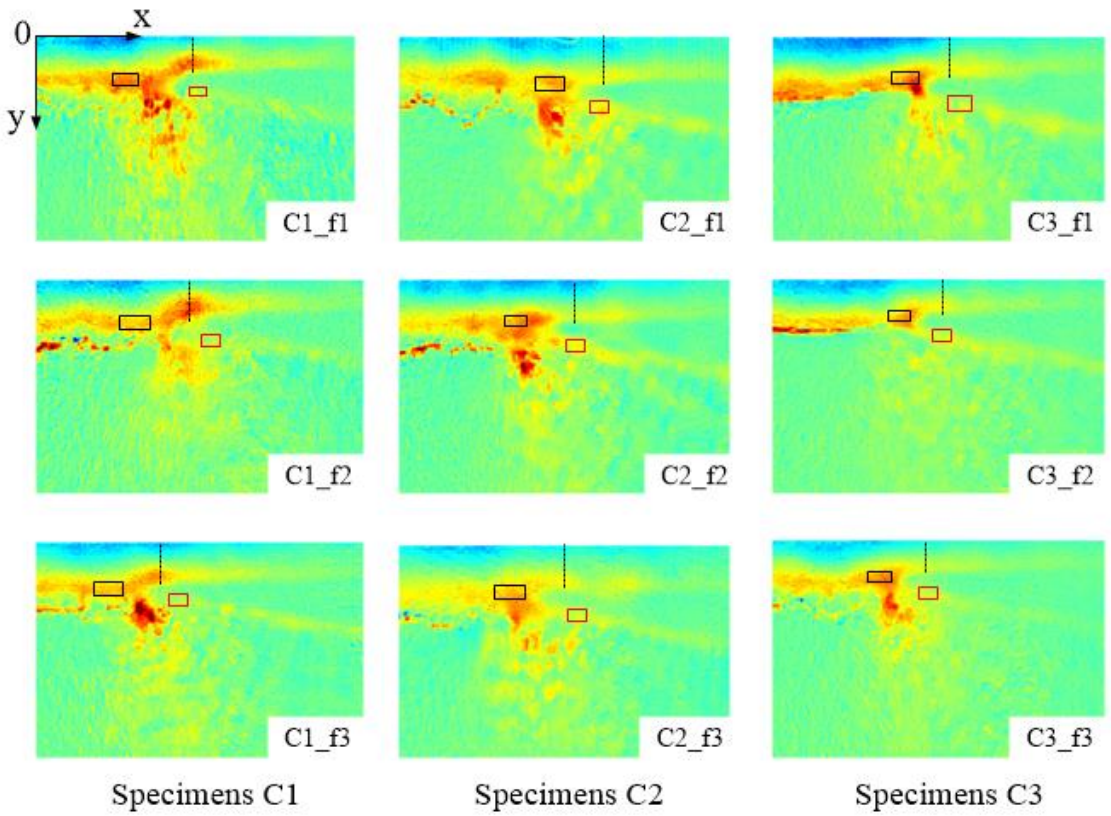

Figure 8.11: Images 2 of different specimens

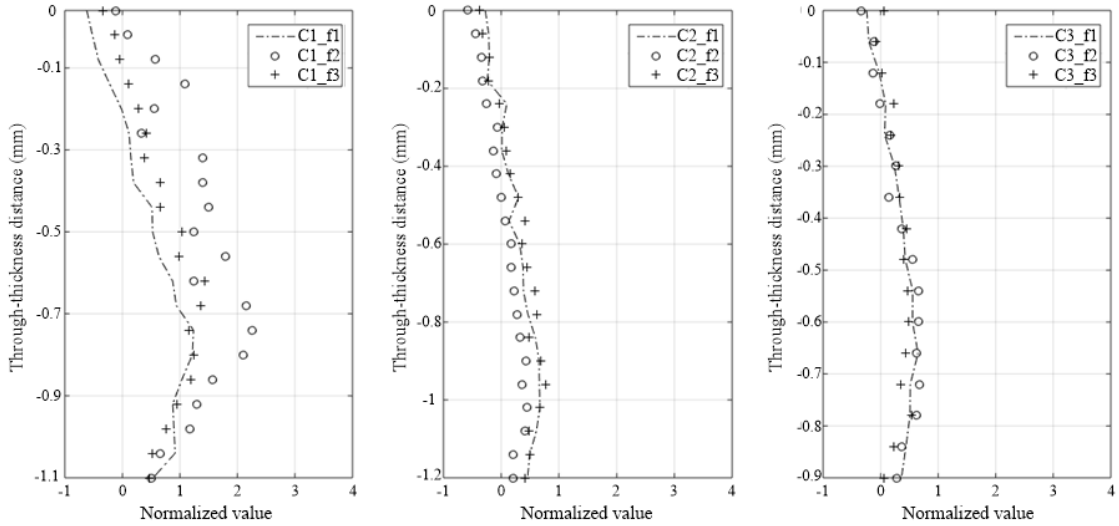

Figure 8.12: Line plots of the normalized $\Delta T/T$ values along y-direction taken 8 pixels ahead of the peel stopper tip

Furthermore, an increase in $\Delta T/T$ at the peel stopper/core interface is observed in C2 and C3 when the crack approaches the tri-material junction. To quantify the increases in the $\Delta T/T$ value, an average $\Delta T/T$ value in the area close to the peel stopper/core interface (see the red rectangular area in Figure 8.11) were calculated from Images 1 and Images 2. The differences between the average $\Delta T/T$ values obtained from Images 1 and Images 2 are plotted in Figure 8.13. It is shown that the $\Delta T/T$ values increase significantly in specimens C2 and C3.

The above results clearly demonstrate the differences in the stress fields for each peel stopper configuration. The TSA results for C1 indicate that large longitudinal stresses (σ_x) exist in the face sheet ahead of the peel stopper tip. It is important to note that as discussed in Chapter 5 the stresses in the face sheet are predominantly in plane, conversely in the foam the thermoelastic response is dominated by the transverse normal stresses. So the σ_x values in the core area below the face sheet/peel stopper interface in C1 are much smaller compared to those in the face sheet. In C2 and C3, this is not the case as an increase in $\Delta T/T$ is identified at the peel stopper/core interface, indicating that σ_x has influence in both the face sheet and the peel stopper. If the bending moment that produces σ_x only acts on the face sheet, it induces large peeling stresses between the face sheet and the peel stopper. Furthermore, compressive transverse normal stresses are induced across the face sheet/peel stopper interface ahead of the crack tip as shown in Figure 8.14 (a). This explains the crack path in specimens C1 where the crack kinked back towards to the face sheet at the tri-material junction. On the other hand, if the bending moment acts on both the face sheet and the peel stopper as in C2 and C3, peeling stresses are induced at the peel stopper/core interface as illustrated in Figure 8.14 (b). Hence, facilitating the crack deflection at the tri-material junction. The TSA has enabled identification of the mechanism controlling crack propagation in the vicinity of the peel stoppers. Moreover, this clearly explains why C2 and C3 deflects the crack much more efficiently than C1.

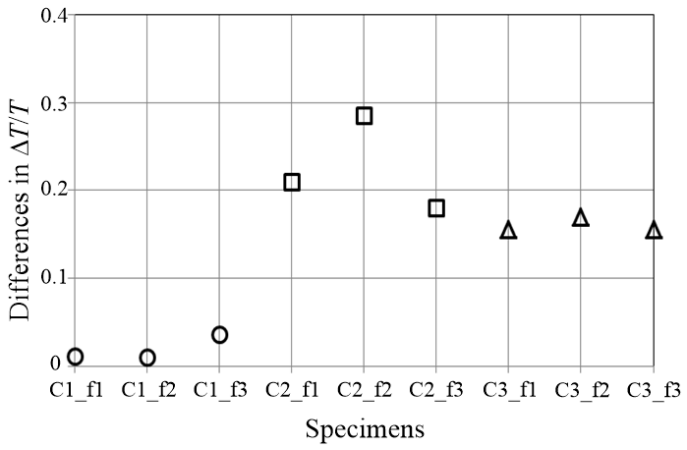

Figure 8.13: Differences in $\Delta T/T$ values between Images 1 and Images 2 calculated form an average value taken in the area close to the peel stopper/core interface

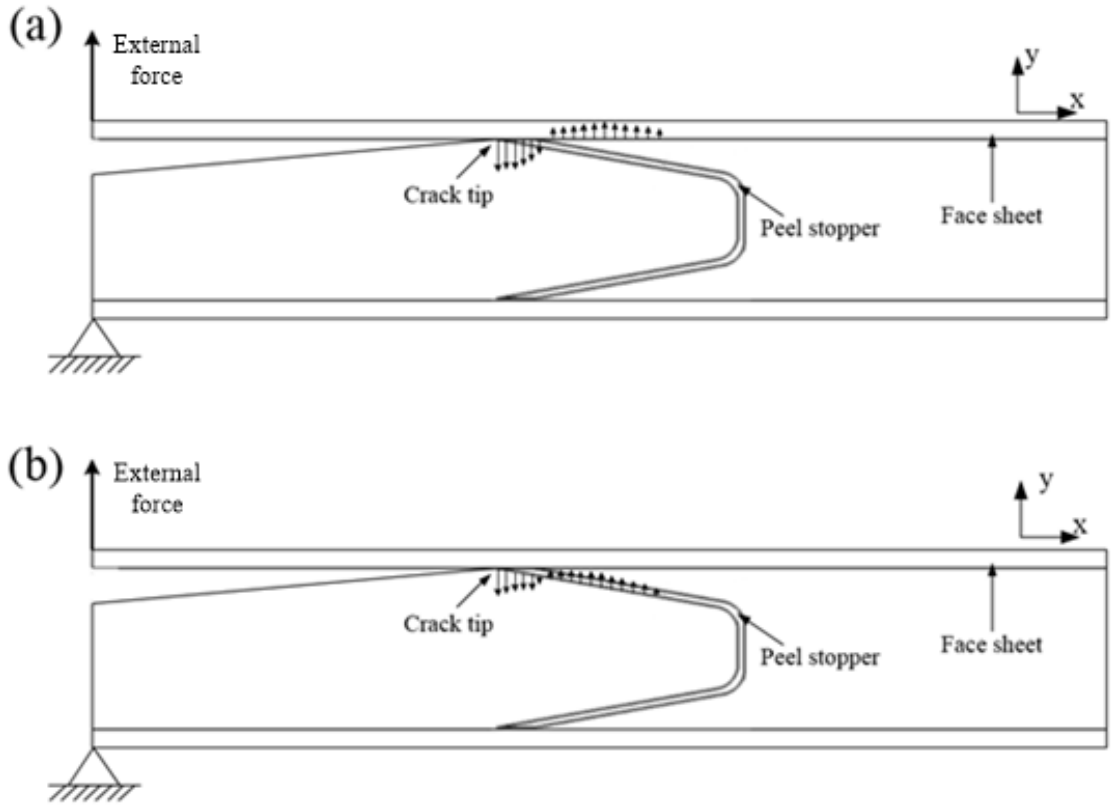

Figure 8.14: Force diagram of the debonded sandwich beam specimen associated with (a) crack path at the face sheet/peel stopper interface and (b) crack path at the PU/foam interface

The specific peel stopper configuration also influences the stress state after the crack deflection has occurred. In specimens C1 large $\Delta T/T$ values can be observed near the face sheet/peel stopper interface as shown by Images 3 of Figure 8.8. In C3 an increase of the $\Delta T/T$ values can be also observed around the face sheet/peel stopper interface (see Images 3 of Figure 8.10), but is most noticeable in the area close to the peel stopper tip. Compared to specimens C1 and C3, the increase in $\Delta T/T$ values at the face sheet/peel stopper interface is much smaller for the specimens C2 (see Images 3 of Figure 8.9). The reason for the relatively large $\Delta T/T$ values observed ahead of the peel stopper tip for the C3 specimens is not entirely clear, but it may be caused by defects introduced during the manufacturing, for example that the inter-fibre layer may not be bonded perfectly to the peel stopper tip and the face sheet at the tri-material junction, and also voids and a resin rich area may be introduced at the tri-material junction as sketched in Figure 8.15. This may be caused by two different mechanisms: 1) the applied vacuum in combination with the atmospheric pressure, which together drives the infusion process, may not be sufficient to assure that air bubbles are not entrapped and that full wetting of the glass fabric is achieved at the tri-material junction; 2) the geometry of the peel stopper tip is imperfect (i.e. not a perfect wedge). This large $\Delta T/T$ values ahead of the peel stopper tip

observed in C1 and C3 specimens indicate a weak bonding at the face sheet/peel stopper interface which can result in the debond damage. Thus, the TSA results provide a clear indication of the reasons why significant debond damage was observed for specimens C1 and C3 during the static tests.

The performance of the three different peel stopper configurations with respect to their ability to deflect propagating interface cracks and the risk of post crack deflection debond damage are shown in Table 8.3. Configurations C2 and C3 are both capable of deflecting the crack at the tri-material junction effectively, whereas configuration C1 is not. The assembly and infusion of sandwich panels with a configuration C3 peel stopper was much more complex than the production sandwich panels with a C2 peel stopper due to the addition of an extra layer of glass fabric during the manufacturing. Moreover, it was difficult to control the manufacturing quality at the tri-material junction for the C3 specimens, and there are strong indications from the TSA data that voids and debond defects were present already before the testing started. It was further observed in the static test that the C3 specimens were prone to display significant debond damage post crack deflection, whereas this did not occur for the C2 specimens. Thus, it is concluded that the C2 peel stopper configuration is superior to the two other tested configurations with respect to its ability to deflect and arrest propagating interface cracks.

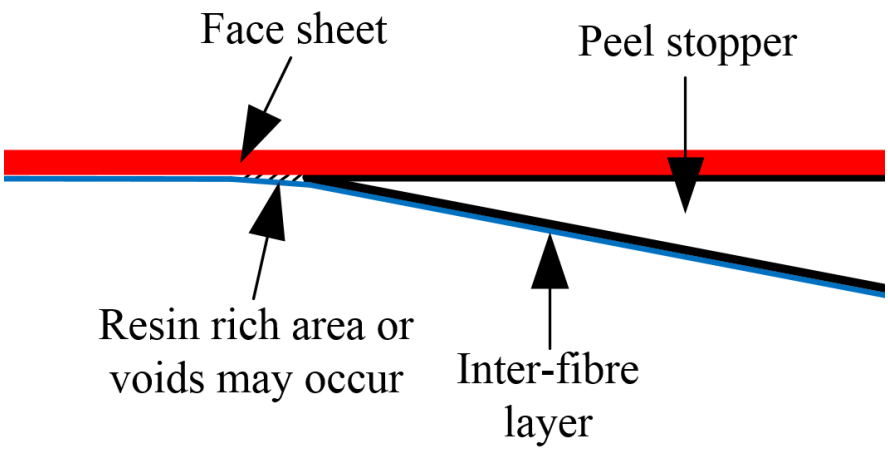

Figure 8.15: Sketch of the tri-material junction for specimens C3

Table 8.3: Comparison of different peel stopper configurations

Peel stopper configurations	C1	C2	C3
Assembly of the sandwich structure	Simple	Simple	Complex
Ability to deflect the interfacial crack	Bad	Good	Good
Post crack deflection behaviour - risk of debond damage	High	Low	High

8.8 Summary

The fatigue crack paths for different peel stopper configurations were examined under mode I dominated loading. It was shown that the peel stopper configurations C2 and C3 were more effective in deflecting propagating interface cracks than configuration C1.

The local effects induced near the peel stopper tip for the different peel stopper configurations were quantified using TSA. It was shown that the local effects induced near the peel stopper tip were significantly influenced by the type of peel stopper used. When the interface crack reached the tri-material junction for the C1 specimens, large stresses were identified ahead of the peel stopper tip in the face sheet. However, an increase in the stresses at the peel stopper/core interface was observed for configurations C2 and C3. It has been further demonstrated that the large stresses ahead of the peel stopper tip for C1 indicate the presence of significant interfacial peeling stresses which result in crack propagation along the face sheet/peel stopper interface. For C2 and C3 it was demonstrated that interfacial peeling stresses are primarily induced along the peel stopper/core interface, thus promoting crack deflection. For specimens C1 and C3, an increase in face sheet stresses was induced ahead of the peel stopper tip when the crack had passed the tri-material junction. This indicates a weak bonding at the face sheet/peel stopper interface where debonding initiated.

It has been shown that both peel stopper configurations C2 and C3 are capable of deflecting a propagating interface crack at the tri-material junction. As the manufacturing quality of configuration C3 is difficult to control, and as C3 also was shown not to be able to effectively arrest the crack after crack deflection, it is concluded that configuration C2 is the only one (of the investigated peel stoppers) capable of both crack deflection and crack arrest.

Chapter 9

Conclusions and future work

9.1 Introduction

The overarching aim of this research was to establish experimental methods based on IR imaging techniques to characterise the interfacial fracture behaviour in foam cored sandwich composites. The motivation for the work has arisen from the current lack of reliable methods to study the fracture mechanisms and determine the crack tip parameters at bi/tri-material interfaces, which are essential to establish a damage tolerance philosophy for debonded sandwich structures.

The work in this thesis can be divided into 3 main parts:

1. The development of TSA to establish the stress state at the interfacial crack tip in sandwich structures, Chapters 4 and 5.
2. The development of an experimental method to characterise the interfacial fracture toughness of foam cored sandwich structures, Chapter 6.
3. The assessment and improvement of the efficiency of specially embedded devices that enable crack deflections and arrest (so called peel stoppers) using the TSA methodology developed in part 1, Chapters 7 and 8.

The relationships between the 3 main parts and the challenges that need to be overcome to characterise a damage tolerance philosophy as described in Chapter 1 are presented in Figure 9.1. The aim was to contribute to the first 3 challenges shown in the flowchart, and the main outcomes of each part of the work are summarised in the following sections. Also references are made to the journal papers and conference presentations/papers by the

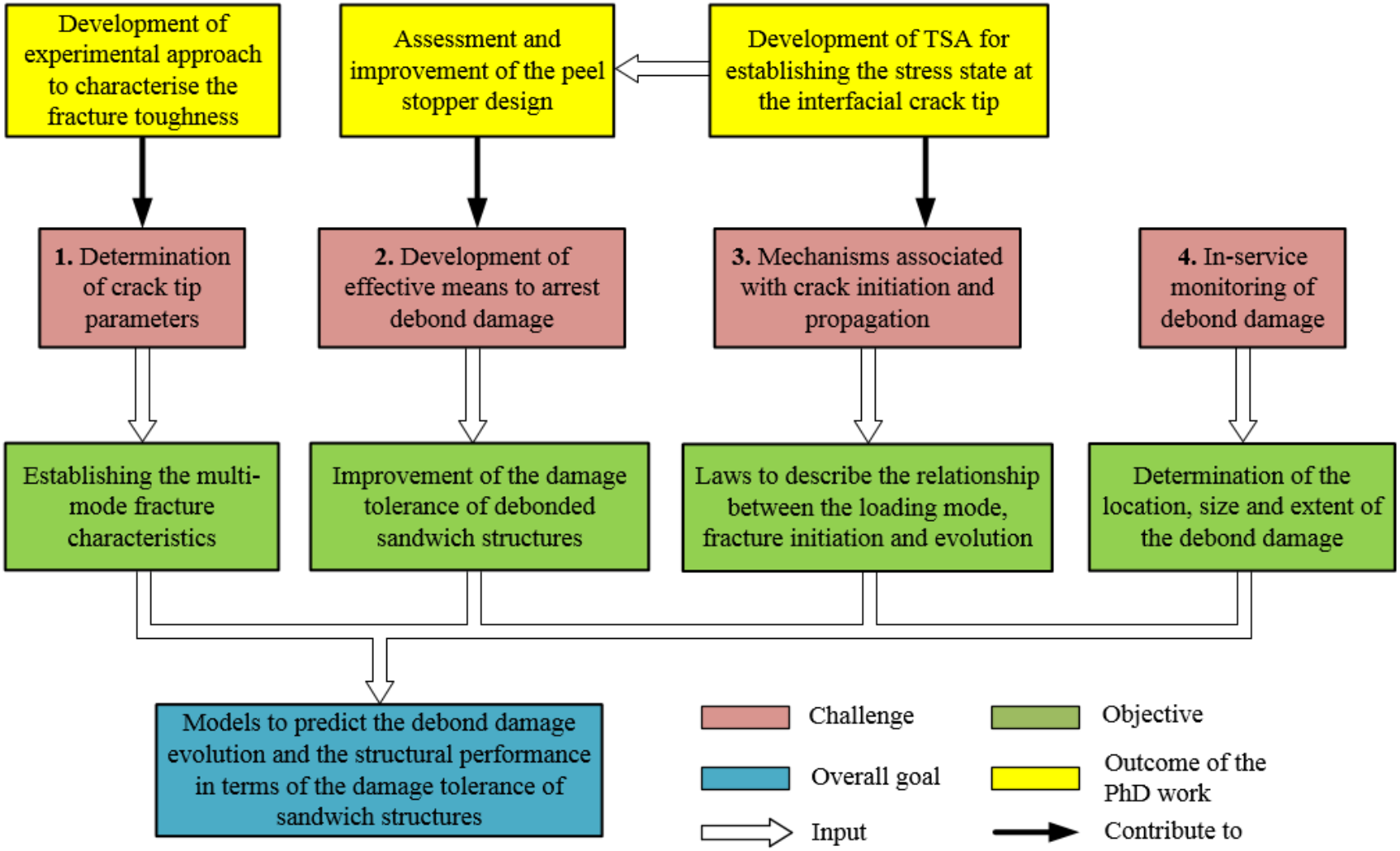

Figure 9.1: Contributions of the work covered in this thesis to establish and improve a damage tolerance philosophy for debonded sandwich structures

author where the work has been published. A complete list of the papers is given in appendix A. In summary the work described in the thesis has made an important contribution to the understanding of the mechanics of interfacial fracture in foam cored composite sandwich structures. This has been achieved by creating and validating novel testing methodologies based on imaging.

9.1.1 Development of TSA to establish the stress state around interfacial cracks in sandwich structures

A new method for motion compensation (MC) has been developed for TSA and applied to establish the full-field stress state at interfacial crack tips in sandwich structures. The outcome can be summarised as:

1. A high spatial resolution MC method based on DIC technique has been developed for TSA. The method enables high spatial resolution images for DIC to be obtained by a white light camera, and therefore increases the accuracy of MC, especially when the displacement field contains steep gradients and discontinuities.

2. It has been shown that by using the correct combination of surface paints, a speckle pattern can be applied to the specimen surface to provide contrast in the white light spectrum for the DIC, but which at the same time provides a uniform emissivity in the IR spectrum so that there is no effect on the TSA. Thus, it is possible for the MC to be conducted simultaneously by capturing the IR and white light images from the same specimen preparation.

3. The feasibility of the MC method to correct the discontinuous and complex motion at a debonded face sheet/core interface has been demonstrated. It has been shown that the effect of motion on the TSA can be effectively eliminated using the MC method, and enables the full-field stress state at an interfacial crack tip to be assessed reliably on both macro and meso scales. This enables the accurate characterisation of interfacial cracks in sandwich structures.

The outcome of the work has been published in references [A1, A4] given in appendix A.

9.1.2 Development of experimental method to characterise interfacial fracture toughness

An experimental method based on high speed IR thermography was proposed for obtaining the fracture toughness of foam cored sandwich composites. The method relates

the interfacial fracture toughness with the temperature change developed at the crack front. The outcome can be summarised as:

1. An experimental approach based on high speed IR thermography has been developed to capture the temperature evolution at the crack front during fracture. It has been demonstrated that IR thermography with 15 kHz frame rate can be used to conduct a quantitative measurement of the crack front temperature associated with the crack growth.

2. A constant of proportionality ψ was derived which links the temperature change per unit area at the crack front to the fracture toughness provided by a validated FE model. It has been shown that ψ values obtained from specimens displaying the same crack path were identical, even though the specimen dimensions and loading mode-mixities were different. Thus, for a particular interface, when ψ is obtained from a known loading condition, the interfacial fracture toughness from any loading configuration can be determined from a direct temperature measurement.

The outcome of the work has been published in references [A2, A5, A7] given in appendix A.

9.1.3 Assessment and improvement of peel stopper devices

The crack paths of different peel stopper devices were investigated under mode I dominated loading conditions. The initial investigations were based on a previously proposed peel stopper configuration [18]. To enable effective crack deflection away from the face sheet, different modifications of the initial peel stopper at the tri-material junction have been proposed. The efficiency of the different peel stopper configurations has been evaluated using TSA. The main findings can be summarised as:

1. The original peel stopper geometry was modified to a ‘U’ shape to reduce the volume and mass, and glass fibre layers were introduced into the PU material to increase the fracture toughness of the peel stopper.

2. Using the new peel stopper geometry, three different configurations of the peel stopper (C1, C2 and C3) were proposed. C1 has the same configuration at the tri-material junction as that of the original peel stopper (the peel stopper are directly bonded to the foam core). For C2 reinforcement fibres inside the peel stopper protrudes from the peel stopper tip and are attached to the face sheet by bonding through the infusion process. For C3 an inter-fibre layer glass fabric is placed

along the peel stopper/core interface and the part of the fibre-layer extending from the peel stopper tip is bonded to the face sheet in the infusion process.

3. The local effects induced near the peel stopper tip for the different peel stopper configurations were quantified using TSA. It was shown that the local effects induced near the peel stopper tip were significantly influenced by the type of peel stopper used.

4. When the crack reached the tri-material junction for the C1 specimens, large stresses were identified ahead of the peel stopper tip in the face sheet. It has been further demonstrated that the large stresses ahead of the peel stopper tip for C1 indicate the presence of significant interfacial peeling stresses which result in crack propagation along the face sheet/peel stopper interface.

5. For configurations C2 and C3, an increase in the stresses at the peel stopper/core interface was observed when the interfacial crack reached the tri-material junction. It was demonstrated that interfacial peeling stresses are primarily induced along the peel stopper/core interface, thus promoting crack deflection.

6. For specimens C1 and C3 an increase in face sheet stresses was induced ahead of the peel stopper tip when the crack had passed the tri-material junction. This indicates a weak bonding at the face sheet/peel stopper where debonding initiated.

7. It has been shown that both peel stopper configurations C2 and C3 are capable of deflecting a propagating crack at the tri-material junction. As the manufacturing quality of configuration C3 is difficult to control, and as C3 also was shown not to be able to effectively arrest the crack after crack deflection, it is concluded that configuration C2 is the only one (of the investigated peel stoppers) capable of both crack deflection and crack arrest.

The outcome of the work has been published in references [A3, A6, A8] given in appendix A.

9.2 Future work

The new MC method developed for TSA has enabled full-field stress states at interfacial crack tips in sandwich structures to be obtained. Using the TSA methodology developed herein, an area of future work which is of particular interest is the derivation of the stress intensity factors for interfacial cracks in sandwich structures. In [136] complete near-tip stress equations have been developed in closed form for isotropic bimaterial interfaces.

Therefore, the development of suitable methods to derive the stress intensity factor from TSA data is a possibility for future work. It is conceived as feasible to achieve this for isotropic material interfaces. However, for orthotropic biomaterial interfaces, like the foam cored sandwich composites, a closed form solution for the near tip stress field is not available in the literature. A general crack tip stress field for interfacial cracks in anisotropic materials has been developed [137], but the near tip stress field equations were not derived for orthotropic bimaterial interfaces. It may be possible to extend the theory to cover orthotropic biomaterial interfaces but this is clearly not a straightforward matter and therefore has not been tackled in the present work.

In Chapter 6, an experimental method has been proposed for obtaining the fracture toughness of an interfacial crack in foam cored sandwich composites. The method was examined using sandwich specimens with E-glass/epoxy face sheets and cross-linked PVC H100 foam loaded in the MMB rig. It was shown that, for a particular interface, when a constant of proportionality ψ was obtained from a known mode-mixity, ψ can be used to derive the fracture toughness for any mode-mixities and specimen dimensions by a direct temperature measurement. Future work should be conducted to fully validate this proposition. An investigation of ψ for different test methods and constituent materials is required. However, the work described in this thesis has provided an important first step to show that there is a simple linear relationship between the temperature change per unit area at the crack front and the fracture toughness for 'brittle' materials.

Finally, an area which should be studied in future work is the investigation of the efficiency of different peel stopper configurations under mode II dominated loading. The TSA methodology and the test method developed in this thesis can be applied to characterise the local effects induced by different peel stopper configurations and to understand the mechanisms that control crack propagation in the vicinity of the peel stoppers.

Appendix A

Journal publications

[A1]. W.Wang, R.K. Fruehmann, J.M. Dulieu-Barton, "A high spatial resolution motion compensation method for thermoelastic stress analysis", submitted, 2015.

[A2]. W.Wang, J.M. Dulieu-Barton, O.T. Thomsen, "A methodology for characterising the interfacial fracture toughness of sandwich structures", accepted with minor corrections, 2015.

[A3]. W. Wang, G. Martakos, J.M. Dulieu-Barton, J.H. Andersen, O.T. Thomsen, "Crack propagation mechanisms of bi-material interface crack approaching a tri-material junction", in preparation.

Conference publications

[A4]. W. Wang, J.M. Dulieu-Barton, R.K. Fruehmann, "Thermoelastic stress analysis of an interface crack in composite sandwich structures", Conference proceeding of 10th international conference on sandwich structures, Nantes, France, 2012.

[A5]. W. Wang, J.M. Dulieu-Barton, O.T. Thomsen, "Characterization of interfacial fracture toughness of sandwich structures using high speed infrared thermography", 21st DYMAT Technique meeting - high speed imaging for dynamic testing of materials and structures, London, UK, 2013.

[A6]. W. Wang, O.T. Thomsen, J.M. Dulieu-Barton, "Full-field analysis of stress distribution at crack arresting devices in sandwich structures", Society for experimental mechanics conference, Greenville, SC, USA, 2014.

[A7]. W. Wang, J.M. Dulieu-Barton, O.T. Thomsen, "Characterization of interfacial fracture toughness of sandwich structures", Society for experimental mechanics conference, Greenville, SC, USA, 2014.

[A8]. W. Wang, J.M. Dulieu-Barton, O.T. Thomsen, "Assessment of stress evolution at crack arresting devices in sandwich structures using thermoelastic stress analysis", 16th international conference on experimental mechanics, Cambridge, UK, 2014

References

[1]. D. Zenkert, *An Introduction To Sandwich Construction*. London: Chameleon Press, 1995.

[2]. D. Zenkert, *The Handbook of Sandwich Construction*. EMAS/Engineering Materials Advisory Services Ltd, 1997.

[3]. O.T. Thomsen, "Sandwich materials for wind turbine blades - present and future", *Journal of Sandwich Structures and Materials*, vol. 11, no. 1, pp. 7-26, 2009.

[4]. D. Zenkert, "Damage tolerance of naval sandwich panels", in *Major Accomplishments in Composite Materials and Sandwich Structure: An Anthology of ONR Sponsored Research* (I.M. Daniel., eds.), pp. 279-303, Springer, 2009.

[5]. A.S. Herrmann, P.C. Zahlen and I. Zuardy, "Sandwich structures technology in commercial aviation – present applications and future trends", in *Sandwich Structures7: Advancing with Sandwich Structures and Materials* (O.T. Thomsen, B.E., and L.A., eds.), (Dordrecht), pp. 13-26, Springer, 2005.

[6]. T.R. Emery, J.M. Dulieu-Barton, "Thermoelastic stress analysis of damage mechanisms in composite materials", *Composites: Part A*, vol. 41, pp. 1729-1742, 2010.

[7]. S. Dietrich, M. Koch, P. Elsner, K. Weidenmann, "Measurement of sub-surface core damage in sandwich structures using in-situ hertzian indentation during x-ray computed tomography", *Experimental Mechanics*, vol. 54, pp. 1385-1393, 2014.

[8]. M.A. Sutton, W. Zhao, S.R. McNeill, J.D. Helm, R.S. Piascik and W.T. Riddell, "Local crack closure measurements: development of a measurement system using computer vision and a far-field microscope", in *Advances in Fatigue Crack Measurement and Analysis* (R.C. McClung., eds.), pp. 145-156, ASTM STP 1343, West Conshohocken, PA, 1999.

[9]. M. Johannes, J.M. Dulieu-Barton, E. Bozhevolnaya, O.T. Thomsen, "Characterization of local effects at core junctions in sandwich structures using thermoelastic stress analysis", *Journal of Strain Analysis for Engineering Design*, vol. 43, no. 6, pp. 469-492.

[10]. V. Vadakke, L.A. Carlsson, “Experimental investigation of compression failure of sandwich specimens with face/core debond”, *Composites Part B: Engineering*, vol. 35, pp. 583-590, 2004.

[11]. S. El-Sayed, S. Sridharan, “Imperfection-sensitivity of integral and debonded sandwich beams under compression”, *Sandwich Structures & Materials*, vol. 4, no. 1, pp. 49-69, 2002.

[12]. D.W. Sleight, J.T. Wang, “Buckling analysis of debonded sandwich panel under compression”, *NASA Technical Memorandum 4701*.

[13]. H. Mahfuz, S. Islam, M. Saha, L.A. Carlsson and S. Jeelani, “Buckling of sandwich composites; effects of core-skin debonding and core density”, *Applied composite materials*, vol. 12, pp. 73-91, 2004.

[14]. T.L. Anderson, *Fracture Mechanics: Fundamentals and Applications*. CRC Press, 2005.

[15]. A. Shipsha, M. Burman and D. Zenkert, “Interfacial fatigue crack growth in foam core sandwich structures”, Fatigue & Fracture of Engineering Materials & Structures, vol. 22, no. 2, pp. 123-131, 2001.

[16]. H.C. Cao and A.G. Evans, “An experimental study of the fracture resistance of bimaterial interfaces”, *Mechanics of Materials*, vol. 7, pp. 295-304, 1989.

[17]. J. Grenestedt, “Development of a new peel-stopper for sandwich structures”, *Composites Science and Technology*, vol. 59, pp. 251-259, 2003.

[18]. J. Jakobsen, E. Bozhevolnaya and O.T. Thomsen, “New peel stopper concept for sandwich structures”, *Composites Science and Technology*, vol. 67, pp. 3378-3385, 2007.

[19]. Y. Hirose, M. Hojo, A. Fujiyoshi and G. Matsubara, “Suppression of interfacial crack for foam core sandwich panel with crack arrester”, *Advanced Composite Materials*, vol. 16, No. 1, pp. 11-30, 2007.

[20]. R.K. Fruehmann, W. Wang, J.M. Dulieu-Barton and S. Quinn, “The application of thermoelastic stress analysis to evaluate debond damage in composite sandwich structures”, *Applied Mechanics and Materials*, vol. 70, pp. 470-475, 2011.

[21]. T.M. Wulf, “Automated ultrasonic inspection of large-scale sandwich structures”, in *Sandwich Structures7: Advancing with Sandwich Structures and Materials* (O.T. Thomsen, B.E., and L.A., eds.), (Dordrecht), pp. 795-804, Springer, 2005.

[22]. E. Fadamand-Ashtiani, J. Cugnoni, J. Botsis, “Monitoring and characterization of the interfacial fracture in sandwich composites with embedded multiplexed optical sensors”, *Composites Structures*, vol. 96, pp.476-483, 2013.

[23]. J.M. Dulieu-Barton, “Introduction to thermoelastic stress analysis”, *Strain*, vol. 35, pp. 35-39, 1999.

[24]. R.K. Fruehmann, D. Crump and J.M. Dulieu-Barton, “Characterization of an infrared detector for high frame rate thermography”, Measurement Science and Technology, vol. 24, no. 10, 2013.

[25]. R.K. Fruehmann, J.M. Dulieu-Barton and W. Wang, “Debond damage assessment in foam/core composite sandwich structures”, *18th International conference on composite materials*, 2011.

[26]. E. Bozhevolnaya, J. Jakobsen and O.T. Thomsen, “Fatigue performance of sandwich beams with peel stoppers”, *Strain*, vol. 45, pp. 349-357, 2009.

[27]. F.T. Frederick and P.A. Bingham, *Fibreglass and Glass Technology*. New York: Springer Science and Business Media, 2010.

[28]. D.W. Chalmers, “The potential for the use of composite materials in marine structures”, *Journal of Marine Structures*, vol. 7, pp. 441-456, 1994.

[29]. P.S. Veers, “Trends in the design, manufacture and evaluation of wind turbine blades”, *Journal of Wind Energy*, vol. 6, pp. 245-259, 2003.

[30]. D. Hull and T.W. Clyne, *An Introduction to Composite Materials*. Cambridge: Cambridge University Press, 1996.

[31]. Y. Frostig and Y. Shenhad, “High-order bending of sandwich beams with a transversely flexible core and unsymmetrical laminated composite skins”, *Composites Engineering*, vol. 5, no. 4, pp. 405-414, 1995.

[32]. G.M. Viana and L.A. Carlsson, “Mechanical properties and fracture characterization of cross-linked PVC foams”, *Journal of Sandwich Structures & Materials*, vol. 4, no. 2, pp. 99-113, 2002.

[33]. A.H. Landrock, *Handbook of Plastic Foams: Types, Properties, Manufacture and Applications*. New Jersey: Noyes Publications, 1995.

[34]. C. Berggreen, K. Branner, J.F. Jensen and J.P. Schultz, “Application and analysis of sandwich elements in the primary structure of large wind turbine blades”, *Journal of Sandwich Structures and Materials*, vol. 9, no. 6, pp. 525-552, 2007.

[35]. P.G. Bergan, L.Buene, A.T. Echtermeyer and B. Haymann, “Assessment of FRP sandwich structures for marine applications”, *Marine Structures*, vol. 7, no. 2-5, pp. 457-473, 1994.

[36]. K.F. Kicki and B.T. Astrom, “Manufacturing and applications of structural sandwich components”, *Composites Part A*, vol. 28, no. 2, pp. 97-111, 1997.

[37]. M.M. Schwarz, *Composite materials handbook*. McGraw-Hill Inc, 1984.

[38]. P. Brondsted, H. Liholt and A. Lystrup, “Composite materials for wind turbine blades”, *Annual review of materials research*, vol. 35, pp. 505-538, 2005.

[39]. B.F. Sorensen, E. Jorgensen, C.P. Debel, F.M. Jensen, H.M. Jensen, T.K. Jacobsen and K.M. Halling, “Improved design of large wind turbine blades of fibre composites (phase 1) – summary report”, tech.rep., Riso-R-1390(EN), 2004.

[40]. C. Berggreen, *Damage Tolerance of Debonded Sandwich Structures*. PhD thesis, Technical University of Denmark, 2004.

[41]. L.A. Carlsson and G.A. Kardomateas, *Structural and Failure Mechanics of Sandwich Composites*. Springer Science Business Media, 2011.

[42]. C. Lundsgaard-Larsen, C. Berggreen and L.A. Carlsson, “Tailoring sandwich face/core interface for improved damage tolerance-part ii: Experiments”, *Applied Composites Materials*, Vol. 17, no. 6, pp. 621-637, 2010.

[43]. A.A. Griffith, “The phenomena of rupture and flow in solids”, *Philosophical Transactions*, vol. A, pp.163-198, 1920.

[44]. T.L. Anderson, *Fracture Mechanics: Fundamentals and Applications*. Broken Sound Pkwy NW: Taylor & Francis Group, 2005.

[45]. G.R. Irwin, “Onset of fast crack propagation in high strength steel and aluminium alloys”, *Sagamore Research Conference Proceed*

ings, vol. 2, pp. 289-305, 1956.

[46]. J.W. Hutchinson and Z. Suo, “Mixed mode cracking in layered materials”, *Advances in Applied Mechanics*, vol. 29, pp. 63-191, 1992.

[47]. Z. Suo, “Singularities interacting with interface and cracks”, *International Journal of Solids and Structures*, vol. 25, pp. 1133-1142, 1989.

[48]. M. Williams, “The stresses around a fault or crack in dissimilar media”, *Bulletin of the Seismological Society of America*, vol. 49, no.2, pp. 199-204, 1959.

[49]. P.G. Charalambides and W. Zhang, “An energy method for calculating the stress intensities in orthotropic bimaterial fracture”, *International Journal of Fracture*, vol. 76, pp. 97-120, 1996.

[50]. J.L. Beuth, “Separation of crack extension modes in orthotropic delamination models”, *International Journal of Fracture*, vol. 77, pp. 305-321, 1996.

[51]. H.M. Jensen, J.W. Jutchinson, K.S. Kim, “Decohesion of a cut prestressed film on a substrate”, *International Journal of Solid Structure*, vol. 26, pp. 1099-1114, 1990.

[52]. K.M. Liechti and Y.S. Chai, “Asymmetric shielding in interfacial fracture under inplane shear”, *Journal of Applied Mechanics*, 1990.

[53]. L.A. Carlsson, L.S. Sendlein and S.L. Merry, “Characterization of face/ core shear fracture of composite sandwich beams”, Journal of Composite Materials, vol. 25, pp. 101-116, 1991.

[54]. F. Aviles and L.A. Carlsson, “Analysis of the sandwich DCB specimens for debond characterization”, Engineering Fracture Mechanics, vol. 75, no. 2, pp. 153-168, 2008.

[55]. J. Ratcliffe and W.J. Cantwell, “Center notch flexure sandwich geometry for characterizing skin-core adhesion in thin-skinned sandwich structures”, *Journal of Reinforced Plastics and Composites*, vol. 20, no.11, pp. 945-975, 2001.

[56]. W.J. Cantwell and P. Davies, “A test technique for assessing core-skin adhesion in composite sandwich structures”, Journal of Materials Science Letters, vol. 13, no. 3, pp. 203-205, 1994.

[57]. X. Li and L.A. Carlsson, “The tilted sandwich debond (TSD) specimen for face/core interface fracture characterization”, *Journal of Sandwich Structures & Materials*, vol. 1, no. 1, pp. 60-75, 1999.

[58]. X. Li and L.A. Carlsson, “Fracture mechanics analysis of tilted sandwich debond (TSD) specimen” *Journal of Composite materials*, vol. 35, no. 23, pp. 2145-2167, 2001.

[59]. K.N. Shivakumar and S.A. Smith, “In situ fracture toughness testing of core materials in sandwich panels”, *Journal of Composite Materials*, vol. 38, no. 8, pp.655-668, 2004.

[60]. C. Berggreen and L.A. Carlsson, “A modified TSD specimen for fracture toughness characterization – fracture mechanics analysis and design”, *Journal of Composite Materials*, vol. 44, no. 15, pp. 1893-1911, 2010.

[61]. A. Quispitupa, C. Berggreen and L.A. Carlsson, “Design analysis of the mixed mode bending sandwich specimen”, *Journal of Sandwich Structures & Materials*, vol. 12, pp. 253-272, 2010.

[62]. A. Quispitupa, C. Berggreen and L.A. Carlsson, “On the analysis of a mixed mode bending sandwich specimen for debond fracture characterization”, *Journal of Sandwich Structures & Materials*, vol. 76, pp. 594-613, 2009.

[63]. A. Quispitupa, C. Berggreen and L.A. Carlsson, “Face/core interface fracture characterization of mixed mode bending sandwich specimens”, *Fatigue & Fracture of Engineering Materials & Structures*, vol. 34, pp. 839-853, 2011.

[64]. R.C. Østergaard and B.F. Sorensen, “Interface crack in sandwich specimen”, *International Journal of Fracture*, vol. 143, pp. 301-316, 2007.

[65]. R.C. Østergaard, B.F. Sorensen and P. Brondsted, “Measurement of interface fracture toughness of sandwich structures under mixed mode loadings”, *Journal of Sandwich Structures & Materials*, vol. 9, pp. 445-465, 2007.

[66]. B. Lascoup, Z. Anoura, K. Khellil and M. Benzeggagh, "Stitching effect on static and dynamic behaviour of sandwich structures", *in Sandwich Structures7: Advancing with Sandwich Structures and Materials* (O. T. Thomsen, B. E., and L. A., eds.), (Dordrecht), pp. 681-690, Springer, 2005.

[67]. P. Potluri, E. Kusak and T. Y. Reddy, "Novel stitch-bonded sandwich composite structures", *Composite Structures*, vol. 59, pp. 251-259, 2003.

[68]. J. Grenestedt, "Development of a new peel-stopper for sandwich structures", Composites Science and Technology, vol. 61, p. 1555-1559, 2001.

[69]. C. Wonderly and J. Grenestedt, "Dynamic performance of a peel stopper for composite sandwich ship structures", Journal of Composite materials, vol. 38, no. 10, pp. 805-831, 2004.

[70]. Y. Hiorse, G. Matsubara, M. Hojo, H. Mastsuda and F. Inamura, "Evaluation of modified crack arrester by fracture toughness tests under mode I type and mode II type loading for foam core sandwich panel", *in Proc, US-Japan conference on composite materials*, Tokyo, Japan, 2008.

[71]. M. Rinker, P. C. Zahlen, M. John, R. Schäuble, "Investigation of sandwich crack stop elements under fatigue loading", *Journal of Sandwich Structures and Materials*, vol. 14, pp. 55-73, 2012.

[72]. J. Jakobsen, J. H. Andreasen and O. Thomsen, "Crack deflection by core junctions in sandwich structures", *Engineering Fracture Mechanics*, vol. 76, p. 2135-2147, 2009.

[73]. J. Jakobsen, O. Thomsen and J. H. Andreasen, "Crack deflection analyses of different peel stopper designs for sandwich structures", *Composites Science and Technology*, vol. 69, pp. 870-875, 2009.

[74]. E. Bozhevolnaya, J. Jakobsen and O. Thomsen, "Fatigue performance of sandwich beams with peel stoppers", *Strain*, vol. 45, pp. 349-357, 2009.

[75]. J.M. Monteiro, M. Vaz, F.Q. Melo and J.F.S Gomes, "Use of interferometric techniques for measuring the displacement field the plane of a part-through crack existing in a plate", *International Journal of Pressure Vessels and Piping*, vol. 78, pp. 253-259, 2001.

[76]. J.S. Epstein, H.Y. Jung and W.G. Reuter, "Stress intensity factor extraction using moiré interferometry based on a two-parameter displacement eigenfunction: validity criteria and comparison with ASTM e-399 & plane strain test methods", *Optics and Lasers in Engineering*, vol. 13, pp. 167-180, 1990.

[77]. S. Roux, J. Réthoré and F. Hild, "Digital image correlation and fracture: an advanced technique for estimating stress intensity factors of 2D and 3D cracks", *Journal of physics D: Applied physics*, vol. 42, no. 21, 2009.

[78]. V. Richter-Trummer, P.M.G.P. Moreira, S.D. Pastrama, M.A.P, Vaz and P.M.S.T. de Castro, "Methodology for in situ stress intensity factor determination on cracked structures by digital image correlation", *International Journal of Structural Integrity*, vol. 1, no, 4, pp. 344-357, 2010.

[79]. R.A. Tomlinson, A.D. Nurse and E.A. Patterson, "On determining stress intensity factors for mixed mode cracks from thermoelastic data", *Fatigue & Fracture of Engineering Materials & Structures*, vol. 20, no. 2, pp. 217-226, 1997.

[80]. F.A. Diaz, E.A. Patterson , R.A. Tomlinson and J.R. Yates, "Measuring stress intensity factors during fatigue crack growth using thermoelasticity", *Fatigue & Fracture of Engineering Materials & Structures*, vol. 27, pp. 571-583, 2004.

[81]. D. Nowell, R.J.H. Paynter and P.F.P. de Matos, "Optical methods for measurement of fatigue crack closure: moiré interferometry and digital image correlation", *Fatigue & Fracture of Engineering Materials & Structures*, vol. 33, pp. 778-790, 2010.

[82]. S. Daly, A. Miller, G. Ravichandran and K. Bhattacharya, "An experimental investigation of crack initiation in thin sheets of nitinol", *Acta Materialia*, vol. 55, pp. 6322-6330, 2007.

[83]. S.W. Robertson, A. Mehta, A.R. Pelton and R.O. Ritchie, "Evolution of crack-tip transformation zones in superelastic nitinol subjected to in situ fatigue: A fracture mechanics and synchrotron x-ray microdiffraction analysis", *Acta Materialia*, vol. 55, pp. 6198-6207, 2007.

[84]. R.A. Tomlinson and E.A. Patterson, "Examination of crack tip plasticity using thermoelastic stress analysis", *Thermomechanics and Infra-red Imaging*, Vol. 7, pp. 123-129, 2011.

[85]. R.A. Tomlinson and L. Marsavina, "Thermoelastic investigations for fatigue life assessment", *Experimental Mechanics*, vol. 44, no. 5, pp. 487-494, 2004.

[86]. P. Jacquot, "Speckle interferometry: A review of the principal methods in use for experimental mechanics applications", *Strain*, vol. 44, pp. 57-69, 2008.

[87]. F.A.L. Porta, J.M. Huntley, T.E. Chung and R.G. Faulkner, "High magnification moiré interferometer for crack tip analysis of steels", Experimental Mechanics, vol. 40, pp. 90-95, 2000.

[88]. J.M. Huntley and L.R. Benckert, "Measurement of dynamic crack tip displacement field by speckle photography and interferometry", Optics and Lasers in Engineering, vol. 19, pp. 299-312, 1993.

[89]. F.A.L. Porta, *High magnification moiré interferometric measurement of crack tip deformation fields in stainless steels*. PhD thesis, Loughborough University, 1999.

[90]. J. Soons, P. Lava, D. Debruyne and J. Dirckx, "Full-field optical deformation measurement in biomechanics: digital speckle pattern interferometry and 3D digital image correlation applied to bird beaks", *Journal of the Mechanical Behaviour of Biomedical Materials*, vol. 14, pp. 186-191, 2012.

[91]. P. Bing, Q. Kemao, X. Huimin and A. Anand, "Two-dimensional digital image correlation for in-plane displacement and strain measurement: a review", Measurement Science and Technology, vol. 20, no. 6, 2009.

[92]. D. Nowell, M.E. Kartal and P.F.P. de Matos, "Digital image correlation measurement of near-tip fatigue crack displacement fields: constant amplitude loading and load history effects", *Fatigue & Fracture of Engineering Materials & Structures*, vol. 36, pp. 3-13, 2012.

[93]. K.C. Jajam and H.V. Tippur, "Quasi-static and dynamic fracture behaviour of particulate polymer composites: a study of nano- vs. micro-size filler and loading-rate effects", *Composites: Part B*, vol. 43, pp. 3467-3481, 2012.

[94]. L. Dongyeon, T. Hareesh, K. Madhu and B. Phillip, "Experimental study of dynamic crack growth in unidirectional graphite/epopxy composites using digital image correlation method and high-speed photography", Journal of composite materials, vol. 43, no. 19, pp. 2081-2108, 2009.

[95]. P. Fabrice, G. Ben and R.W. Michael, "Full-field assessment of the damage process of laminated composite open-hole tensile specimens. Part I: Methodology", *Composites: Part A*, vol. 38, no. 11, pp. 2321-2332, 2007.

[96]. M.P. Rostand, B. Claudiu and G. Michel, "Experimental and numerical fracture analysis of a pre-cracked aluminium specimen using the grid method", *Fracture and Fatigue*, vol. 7, pp. 79-84, 2014.

[97]. A. Stephane, F. Emmanuel, V. Alain, H. Patrice and S. Yves, "A full-field optical method for the experimental analysis of reinforced concrete beams repaired with composites", *Composites Part A*, vol. 35, pp. 873-884, 2004.

[98]. A.Y. Fedorova, M.V. Bannikov and O.A. Plekhov, "Infrared thermography study of the fatigue crack propagation", *Fracture and Structural Integrity*, vol. 21, pp. 46-53, 2012.

[99]. K. Krishnaprasad and R.V. Prakash, "Fatigue crack growth behaviour in dissimilar metal weldment of stainless steel and carbon steel", *World Academy of Science, Engineering and Technology*, vol. 32, pp. 873-879, 2009.

[100]. J.M. Dulieu-Barton, C. Berggreen and C. Mettemberg, "Assessment of foam fracture in sandwich beams using thermoelastic stress analysis", *17th International Conference on Composite Materials*, 2009.

[101]. E.L. Dereniak and G.D. Boreman, *Infrared Detectors and Systems*. John Wiley & Sons, Inc, 1996.

[102]. M.A. Bramson, Infrared Radiation: *A handbook for applications*. Plenum Press, 1968.

[103]. A. Rogalski, "Infrared detectors: status and trends", *Progress in Quantum Electronics*, vol. 27, pp. 59-210, 2003.

[104]. J.A. Jamieson, R.H. McFee, G.N. Plass and R.G. Richards, *Infrared physics and engineering*. McGraw-Hill, 1963.

[105]. W. Thompson, "Dynamical theory of heat with numerical results deduced from Mr Joule's equivalent of a thermal unit and M Regnault's observation on steam", *Transactions of the Royal Society of Edinburgh*, vol. 20, pp. 261-283, 1853.

[106]. J.M. Dulieu-Barton and P. Stanley, "Development and applications of thermoelastic stress analysis", *Journal of Strain Analysis for Engineering Design*, vol. 33, no. 2, pp. 93-104, 1998.

[107]. P. Stanley and W.K. Chan, "The application of thermoelastic stress analysis technique to composite materials", *Strain analysis for engineering design*, vol. 23, pp. 137-143, 1998.

[108]. M.H. Belgen, "Structural stress measurement with an infrared radiometer", *ISA transactions*, vol. 6, pp. 49-53, 1967.

[109]. N. Harwood, W.M. Cummings, *Thermoelastic stress analysis*, Adam Hilger IOP Publishing, Bristol, 1991.

[110]. T.R. Emery, *Identification of damage in composite materials using thermoelastic stress analysis*. PhD thesis, University of Southampton, 2007.

[111]. J.M. Dulieu-Smith, S. Quinn, R.A. Shenoi, P.J.C.L Read and S.S.J. Moy, "Thermoelastic stress analysis of a GRP tee joint", *Applied composite materials*, vol. 4, pp. 283-303, 1997.

[112]. J.M. Dulieu-Barton, J.S. Earl and R.A. Shenoi, "Determination of the stress distribution in foam-cored sandwich construction composite tee joints", *Journal of Strain Analysis*, vol. 36, no. 6, pp. 545-560, 2001.

[113]. R.K. Fruehmann, *stress and damage assessment in woven composite materials by means of thermoelastic stress analysis*. PhD thesis, University of Southampton, 2009.

[114]. T. Sakagami, N. Yamaguchi, S. Kubo and T. Nishimura, "A new full-field motion compensation technique for infrared stress measurement using digital image correlation", *The Journal of Strain Analysis for Engineering for Engineering Design*, vol. 43, no. 6, pp. 539-549, 2008.

[115]. M. Silva and G. Ravichandran, "Combined thermoelastic stress analysis and digital image correlation with a single infrared camera", *The Journal of Strain Analysis for Engineering for Engineering Design*, vol. 46, no. 8, pp. 783-793, 2011.

[116]. L.B. Meng, G.C. Jin, and X. F. Yao, "Errors caused by misalignment of the optical camera axis and the object surface in the DSCM", *Journal of Tsinghua University*, 2006.

[117]. M.A. Sutton, J.J. Orteu, H. Schreier, *Image correlation for shape, motion and deformation measurements*. Springer, 2009.

[118]. LaVision GmbH, Göttingen, "Product-Manual for DaVis 8.1 (Strainmaster)", 2012.

[119]. A.F. Robinson, J.M. Dulieu-Barton, S. Quinn and R.L. Burguete, "Paint coating characterization for thermoelastic stress analysis of metallic material", *Measurement Science and Technology*, vol. 21, no. 8, 2010.

[120]. ANSYS 12.1 manual, ANSYS Inc Canonsburg, 2009.

[121]. G. Crammond, S.W. Boyd and J.M. Dulieu-Barton, "Speckle pattern quality assessment for digital image correlation", *Optical Lasers Engineering*, vol. 51, no. 12, pp. 1368-1378, 2013.

[122]. S. Zhang, J.M. Dulieu-Barton, R.K. Fruehmann and O.T. Thomsen, "A methodology for obtaining material properties of polymeric foam at elevated temperatures", *Experimental mechanics*, vol. 52, no. 1, pp. 3-15, 2012.

[123]. S. Taher, O.T. Thomsen, J.M. Dulieu-Barton and S. Zhang, "Determination of mechanical properties of PVC foam using a modified arcan fixure", *Composites Part A: Applied Science and Manufacturing*, vol. 43, no. 10, pp. 1698-1708, 2012.

[124]. H. Jin, W.Y. Lu, S. Scheffel, T.D. Hinnerichs and M.K. Neilsen, "Full field characterization of mechanical behaviour of polyurethane foams", *International Journal of Solids and Structures*, vol. 44, no. 21, pp. 6930-6944, 2007.

[125]. DIAB-Inc., "Matweb.com – online material datasheet", 2013.

[126]. J.A. Loya, E.I. Villa, J. Fernandez-Saez, "Crack-front propagation during three-point-bending tests of polymethyl-methacrylate beams", *Polymer Testing*, vol. 29, pp. 113-118, 2010.

[127]. B. Farahmand, *Fracture mechanics of metals, composites, welds, and bolted joints: application of LEFM, EPFM, and FMDM theory*, Kluwer Academic, US, 2011.

[128]. G. I. Taylor, H. Quinney, "The latent energy remaining in a metal after cold working", *Proceedings of the Royal Society A*, 1934.

[129]. A. Engelter, F.H. Muller, Kolloid Z 157 (89) 1958.

[130]. E.E. Saenz, L.A. Carlsson, A. Karlsson, "Characterization of fracture toughness (Gc) of PVC and PES foams", *Journal of Materials Science*, vol. 46, no. 9, pp. 3207-3215, 2011.

[131]. S.K. Maiti, M.F. Ashby, L.J. Gibson, "Fracture toughness of brittle cellular solids", *Scripta Metallurigca*, vol. 18, no. 3, pp. 213-217, 1984.

[132]. F. J. Kelly, "An equation for the local thermal emissivity at the vertex of a diffuse conical or v-groove cavity", *Applied Optics*, vol. 5, no. 6, pp. 925-927, 1966.

[133]. M. Manca, A. Quispitupa, C, Berggreen, L.A. Carlsson, "Face/core debond fatigue crack growth characterization using the sandwich mixed mode bending specimen", *Composites Part A*, vol. 43, no. 11, pp. 2120-2127, 2012.

[134]. http://www.instron.us/wa/acc_catalog/prod_list.aspx?cid=1165&cname=2580%20Series%20 load%20Cells, accessed in 2014.

[135]. PERMAlock 40496 polyurethane adhesive data sheet provided by the manufacturer.

[136]. M. Ravichandran and K. Ramesh, "Evaluation of stress field parameters for an interface crack in a bimaterial by digital photoelasticity", *Journal of Strain Analysis*, vol. 40, no. 4, pp. 327-343, 2004.

[137]. X. Deng, "General crack-tip fields for stationary and steadily growing interface cracks in anisotropic bi-materials", *Transactions of the ASME, Journal of Applied Mechanics*, vol. 60, pp. 183-189, 1993.